Aus dem Institut für Robotik und Kognitive Systeme

Direktor:
Prof. Dr.-Ing. Achim Schweikard

Model-based improvements for focal transcranial stimulation

Inauguraldissertation
zur
Erlangung der Doktorwürde
der Universität zu Lübeck
- Aus der Sektion Informatik/Technik -

Vorgelegt von Fernando Javier Gasca Buitrón
geboren in Mexiko-Stadt, Mexiko

Lübeck, im Februar 2013

Fernando Gasca
Ph.D. Student

Institut für Robotik und Kognitive Systeme
Universität zu Lübeck
Ratzeburger Allee 160
23562 Lübeck

1. Berichterstatter:	Prof. Dr.-Ing. Achim Schweikard
2. Berichterstatter:	Prof. Dr. rer. nat. Ulrich G. Hofmann
Tag der mündlichen Prüfung:	19. April 2013
Zum Druck genehmigt:	22. April 2013

For my parents

A mis padres

Contents

Zusammenfassung

Ein wichtiger Aspekt der transkraniellen Stimulation ist es zu erfassen in welchem Ausmaß bestimmte Hirnstrukturen von ihr beeinflusst werden. Bereits seit Beginn der Entwicklung dieser Technik war das Erreichen einer besseren Fokussierung, d.h. die räumliche Auflösung der Stimulation, eine wichtige Herausforderung. Diese Arbeit stellt die Entwicklung von Modellen und Methoden zur Verbesserung der Fokussierung für die zwei am weitesten verbreiteten Stimulationstechniken vor: transkranielle Magnetstimulation (TMS) und transkranielle Gleichstrom-Stimulation (tDCS, aus dem Englischen). Für das Simulieren der Stimulation wurden MRT-basierte, anatomisch korrekte, tierische und menschliche Modelle entwickelt.

Zur Fokussierung von TMS wurde eine leitfähige Platte an der Anregungsspule verwendet. Diese Platte hat ein Fenster, das nur einen Teil des magnetischen Feldes passieren lässt. Somit wird das induzierte elektrische Feld im Gehirn zu einem besser lokalisierten Bereich. Durch Simulationen mit der Finite-Elemente-Methode (FEM) konnte die leitfähige Platte in verschiedenen Szenarien charakterisiert werden. Für diese Szenarien wurde verifiziert, dass sie die Fokussierung verbessert. Die Validierung der Simulationen erfolgte aus experimentellen Messungen mit den beiden häufigsten Spulengeometrien.

Für die Fokussierung bei tDCS wurden drei Ansätze mit mehreren Elektroden entwickelt. Die Ansätze lösen ein inverses Problem, um einen bestimmten Betrag und eine Orientierung des elektrischen Feldes an einer Zielstelle zu erzeugen. Hierfür wurden Optimierungsverfahren mit Nebenbedingungen (unter Berücksichtigung der Patientensicherheit) verwendet. Basierend auf dem gewünschten Stimulationsergebnis berechnen diese Methoden die anzulegenden Elektrodenströme. Der erste Ansatz verwendet die vordefinierte internationale EEG 10/10 Elektrodenkonfiguration. Der zweite Ansatz vermeidet die vordefinierten Elektrodenpositionen. Er basiert auf einer Elektrodenmatrix, die beliebig auf der gewünschten Zielstelle positioniert ist, wobei auch hier die Elektrodenströme optimiert werden. Der dritte Ansatz erlaubt es, die Zahl der aktiven Elektroden zu wählen. Er ermöglicht daher die Verringerung der Hardwareanforderungen und die Herstellung optimierter Mehrelektroden-tDCS Systeme. Folglich ist dieses Verfahren kompatibel mit jedem Gleichstrom-Stimulator. Die Ergebnisse zeigen eine erhebliche Verbesserung der Fokussierung gegenüber den herkömmlichen Setups.

Phantomexperimente zeigen eine Übereinstimmung mit den Simulationen und bestätigen das Potenzial der untersuchten Ansätze für fokussierte Stimulation. Darüber hinaus wurden die Modelle für die Vorausplanung von zwei experimentellen Tierstudien verwendet. In beiden Fällen waren sie entscheidend dafür, die Rolle der Stimulation zu verstehen. Die Modelle und Methoden dieser Arbeit tragen zum besseren Verständnis der transkraniellen Stimulation bei. Sie fördern die systematische Anwendung der Techniken und die Verbesserung ihrer Funktionen.

Abstract

A major issue since the uprising of transcranial stimulation is understanding what extent of the brain is affected by it. Consequently, achieving greater focality (i.e. the spatial resolution of stimulation), has been a challenge ever since. This work presents the development of models and methods for the better understanding as well as for the focality improvement in the two most widely used transcranial stimulation techniques: transcranial magnetic stimulation (TMS) and transcranial direct current stimulation (tDCS). We developed MRI-based anatomically accurate animal and human models for the simulation of stimulation.

For focality in TMS, the concept of a conductive shield plate attached to the stimulating coil was used. The conductive shield has a window which allows only a portion of the magnetic field to pass through. It therefore restricts the induced electric field in the brain to a more localized region. Simulations using the finite element method allowed to characterize the conductive shield in different scenarios. We found that the conductive shield improves coil focality and validated our simulations by obtaining experimental measurements in the two most common coil geometries.

For focality in tDCS, three approaches using multiple electrodes were developed. The approaches solve an inverse problem in order to obtain a specific magnitude and orientation of the electric field at a brain target. Using constrained optimization techniques and taking patient safety into account, our methods obtain the adequate electrode currents to stimulate according to the desired outcome. The first approach employs the predefined international EEG 10/10 electrode configuration, where all possible electrodes can be used. The second approach avoids the fixed electrode positions altogether. It consists of an electrode patch array placed arbitrarily at the desired target, where electrode currents are also optimized. The third approach allows to choose the number of active electrodes in the solution, therefore reducing hardware requirements and making optimized multi-electrode tDCS compatible with any stimulator device. Results show substantial focality improvement over the conventional setups.

Phantom experiments show accordance to the simulations and confirm the potential of the approaches for focal stimulation. Furthermore, we performed the forward planning of two animal studies, in each case pivotal for understanding the role of

stimulation. The models and methods presented in this work contribute to the better understanding of transcranial stimulation and promote its systematic use while enhancing its capabilities.

Chapter 1

Introduction

This chapter covers the motivations for the improvement of non-invasive transcranial stimulation. Firstly, we provide the purpose of this work, explaining the relevance of developing methods to improve the focality in transcranial stimulation. Subsequently, we describe the major clinical applications for which transcranial stimulation has been applied. We explain the potential of transcranial stimulation for understanding the way the human brain works from a cognitive and behavioral perspective. Finally, we present the structure of this work.

1.1 Purpose of this work

Transcranial magnetic stimulation (TMS) and transcranial direct current stimulation (tDCS) are two techniques to modulate neural function non-invasively. They have emerged in the last twenty years, showing great potential to treat neurological conditions and to study the basics of cognitive and behavioral neuroscience [1],[2],[3]. For both techniques, spatial focality, i.e. the extent of brain tissue being affected during stimulation, is of crucial importance because it allows to improve the interpretation of the elicited functional effects, confining them to a clearly defined brain region [4]. Moreover, focal stimulation spares other anatomical structures contributing to less side effects during therapy.

Existing coils for delivering TMS have not evolved substantially since its conception in the 1980s. They still face a focality limitation that hinders the applicability of TMS in the human, as well as in small animal models, which have proven to be a valuable tool for evaluating potential treatments [5],[6],[7]. To enhance the

applicability of TMS, we present the use of a conductive shield plate attached to the stimulating coil; the shield plate has a window through which a smaller portion of the magnetic field generated by the coil can go through, thereby improving its focality. This can be ultimately adapted to any coil and has potential for animal experiments, where the dimensions of the brain are reduced and therefore a higher spatial resolution is required for stimulating specific cortical structures.

The conventional paradigm for applying tDCS consists in using two rectangular pad electrode sponges soaked in saline solution and placed on the scalp. This method is known to produce highly diffuse distributions of the induced electric field in the brain [8],[9]. Additionally, since the conventional paradigm involves two electrodes on the scalp, the results of stimulation are influenced by unwanted reverse effects caused by the reference electrode. The further development of tDCS therefore demands the creation of more focal techniques to deliver stimulation.

Given that cell somata polarization is maximum with either complete radial or tangential stimulation [10], controlling the direction of stimulating currents is also a useful feature. While in TMS one can change the direction of the induced currents simply by rotating the coil with respect to the position of the head [11], no method for controlling the direction of the induced currents has been used so far in tDCS pilot studies. The work of Dmochowski *et al.* [12] has laid out the foundations for performing optimized multi-electrode tDCS. In this work, we elaborate on this idea and bridge the missing gap to make multi-electrode tDCS applicable in a realistic environment. To achieve this, we devised methods for the sparse representation of the optimized solutions, also allowing to control the orientation of the induced currents. Our methods improved focality substantially in relation to the conventional rectangular pads used until now.

The direction of the induced currents during TMS is known to be predominantly tangential to the surface of the cortex. Although the common belief is that tDCS induced currents are radial under the electrodes, we quantitatively show that the induced currents exhibit both radial and tangential components due to the complex folding of the cortex. This finding changes our understanding of the nature of stimulation, shifting from somatic-driven mechanism to a neuronal-afferents-driven one.

The central motivation for this work lies in gaining control over the way transcranial stimulation is delivered by improving focality and understanding the induced electric fields in the brain in order to use the techniques in a rational manner. These

reasons have a direct impact on three important aspects: (1) the applicability of the techniques, (2) the interpretation of the physiological effects of stimulation and (3) the better understanding of their underlying biophysical mechanisms.

1.2 Clinical and scientific motivation

1.2.1 Major depression

Major Depression Disorder (MDD) is a psychiatric condition characterized by prolonged episodes of fatigue, low mood, together with lack of interest and pleasure [13]. It heavily affects the patients, having implications on their interpersonal relations and professional life. MDD will apparently be the second highest cause of disease burden worldwide in 2020 [14]. The estimated cost of depression has been $83.1 billion in the U.S., mostly attributed to time off work [15]. MDD is normally treated with antidepressant medication, psychotherapy and in extreme cases inducing seizures with electroconvulsive therapy. However, treatment efficacy varies and presents transient side-effects [13]. Therefore, new approaches for treating MDD are of great interest to the scientific community.

In 2008, the NeuroStar TMS Theraphy System (Neuronetics, Inc, Malvern PA, USA) obtained the Food and Drug Administration (FDA) approval for the treatment of adult patients with MDD [16]. The patients have to qualify for treatment, having failed to improve their condition previously using antidepressant medication, surpassing the minimal effective dose and duration in the current depressive episode [16],[17]. Once the patient classifies, TMS treatment is applied prefrontally on a daily basis in ca. 30 minute sessions for several weeks.

Nowadays, the evidence for TMS as an effective treatment for MDD has grown substantially [16],[18],[19]. However, there are still a variety of open questions regarding TMS coil location, extent of brain structures that should be stimulated, intensity and frequency of stimulation, as well as dosing.

tDCS trials have been applied to subjects with MDD in the past 10 years and a body of evidence suggests its effectiveness as a treatment [20],[21]. In [22], the authors stimulated severe MDD patients and showed a significant improvement in mood. Other studies have obtained similar results and observed that such effects tend to be more robust in severe patients [23]. However, since clinical development has

taken place primarily in the academia, studies have not been standardized, showing different experimental parameters (stimulation time, intensity, number of sessions) and have therefore undermined validity. For this reason, tDCS has not yet received the legal clearance for its widespread application; a similar situation TMS had ten years back [21].

1.2.2 Stroke

Stroke is one of the leading causes for acquired severe long-term disability in western industrialized countries [24],[25]. It involves the rapid loss of brain function caused by a failure in blood flow at a particular brain region. When the blood supply in the brain stops for more than a few seconds, brain cells die, and as the number of affected brain cells increases, there are a number of motor and cognitive impairments that arise as a result [26]. 55 to 75% of stroke patients have some deficit in their upper limb [27], 20% present aphasia or language impairments [28] and 30% are affected by neglect [29] i.e. the inability of the person to perceive stimuli from the contralateral (or sometimes ipsilateral) side of the lesion.

The conventional approach to rehabilitation in stroke patients is to follow motor, occupational and language-speech therapies [26]. However, in recent years, transcranial stimulation has shown to be greatly beneficial in stroke recovery. Using tDCS, studies have shown that in relatively short periods of time (5 days, 20 minutes daily sessions) stroke patients with aphasia can significantly improve their naming accuracy [30],[31], an effect persisting from one to three weeks after stimulation. In terms of motor function, tDCS and high frequency TMS applied to the affected hemisphere have provided evidence of their potential for recovery treatment [32],[33]. Simultaneous tDCS on both hemispheres, facilitating the affected one and inhibiting the overactivity of the healthy one, in combination with occupational therapy, showed therapeutic gains [34]. Similar positive results have been obtained with both tDCS and TMS for patients with neglect [25].

An important observation to make is that although the authors of the aforementioned studies obtained promising results, there is a lack of understanding of the underlying mechanisms of transcranial stimulation's effect in stroke patients. Furthermore, there is no prior analysis of the stimulation profiles. Only in [31], the authors used functional imaging to spot the desired stimulation sites for tDCS, however recognizing the lack of focality in stimulation.

1.2.3 Other potential clinical conditions

Besides the two most investigated neurological disorders addressed above, transcranial stimulation has been tested for treating variety of other neurological conditions. On the one hand, TMS has been successfully used acutely to treat chronic pain [35], Parkinson's disease [36] and epilepsy [37]. On the other hand, tDCS has also been used to treat Parkinson's [38], pain [39], Alzheimer's [40], craving [41] among other studies [2]. In spite of the current evidence, more robust studies are required to prove the efficacy of these potential treatments.

1.2.4 Understanding how the brain works: cognitive and behavioral neuroscience

Another area of application for transcranial stimulation is the study of brain function by inflicting the so-called "virtual lesions". The concept of a virtual lesion stems from the idea that TMS introduces random noise to the circuits which carry out a particular behavioral process, (e.g. learning, memory, emotions) or a cognitive task (e.g. identifying a geometrical, linguistic or logic pattern) [3]. This means that using repetitive TMS (rTMS), sending trains of pulses in frequencies normally up to $\sim$ 20 Hz, one can alter the neural activation of an anatomical structure associated to a certain function. In this way, TMS can inhibit (with low frequencies, 1 Hz or less) or facilitate (higher frequencies normally up to 20 Hz) neural function [42].

In the case of tDCS, disruption of brain function is associated to polarity of stimulation. Under the electrode where current enters the brain a facilitation is expected, whereas under the electrode where the current exits the brain, an inhibition takes place. A variety of tDCS studies have been performed on healthy subjects and have revealed insights about decision-making [43], attention [44] and language [45], among other studies [2]. tDCS during slow-wave sleep improved declarative memory [46],[47],[48]. Overall, these studies have observed the short-term performance effects. Therefore, there is the need to study the effects' duration in order to systematically design the way to deliver stimulation.

1.3 Structure of this work

This work is structured as follows:

Chapter I (Introduction) provides the purpose of this work and describes the clinical and scientific motivations for the improvement of transcranial stimulation techniques.

Chapter II (Basics) first introduces the physics of transcranial stimulation for both relevant techniques (TMS and tDCS) and then goes on providing an overview of the finite element method, which is used for the simulations presented in this work. We elaborate on common methods for determining electric fields and their main attributes.

Chapter III (Non-invasive transcranial stimulation) provides an overview of both transcranial stimulation techniques used in this work, covering their basic principles of operation and the current knowledge about the mechanisms of action at a neuronal level. We motivate the relevance of focality in transcranial stimulation and describe the state-of-the-art methods for its enhancement.

Chapter IV (Electric field in conductive medium) presents the experimental setup *in vitro* for validating our simulations and establish that superposition of electric sources in a conductive medium holds. The obtained measurements are shown and their implications for the subsequent formulations of this work are discussed.

Chapter V (Forward models) describes the following methods involving the forward models used in this work: (a) experimental setup for the electric field measurements using the conductive shield plate mounted on the TMS coil, (b) workflow for generating anatomically accurate models, (c) considerations for analyzing the direction of the induced electric field, (d) concepts needed to analyze anisotropic conductivity in the brain and (e) requirements and model parameters for the forward planning of two animal studies (TMS and tDCS).

Chapter VI (Inverse problem) presents the linear model of electric conduction in the brain used for formulating the inverse planning under the optimized multi-electrode tDCS paradigm. We present the different optimization schemes to achieve a predefined magnitude and orientation of the electric field at a given target. The experimental setup to validate our inverse planning is described.

Chapter VII (Results) presents the findings stemming from the models and experimental setups presented in chapters V and VI, namely: simplified rat model, measurements of TMS coil with conductive shield, evaluation of multi-electrode optimized tDCS schemes, measurements of inverse planning scenarios *in vitro* for tDCS, analysis of the induced electric field direction in tDCS, multi-targeting capabilities

of multi-electrode tDCS, anisotropic conductivity analysis in tDCS, and forward planning of TMS and tDCS animal experiments.

Chapter VIII (Discussion) performs an analysis of the findings presented in the previous chapter and their implication in the current understanding of transcranial stimulation. We discuss the advantages and limitations of the presented methods.

Chapter IX (Conclusion) is a summary of the achievements presented in this work with their contribution to the field of non-invasive transcranial stimulation. We elaborate on two interesting possibilities for future work: promising brain stimulation techniques and automation of realistic model generation.

Chapter 2

Basics

In this chapter we present the physical foundations of electromagnetic induction which are necessary for solving the forward problem of determining the induced electric field in tissue, whether stemming from a stimulating coil (in TMS) or from stimulating electrodes (in tDCS). We provide a general overview of the finite element method (FEM) and elaborate on other common state-of-the-art methods for calculating electric fields.

2.1 Introduction

The solution to the forward problem involves obtaining a result given a predefined set of parameters intended to produce a desired output. For example, in the context of radiotherapy treatment planning with a robotic arm, it means that the clinician shall choose a set of radiation beams, their intensity, angle of delivery and collimator parameters in order to hit a particular target and to spare other healthy structures. Subsequently, the dose from the beams is calculated and possibly the parameters are readjusted to achieve (or come close to) the desired result. In general, forward problem-solving has the disadvantage that for some desired results it will require several iterations to approach the desired solution. However, dealing with simple cases, usually when the problem does not present stringent constraints, forward planning can be fast and relatively intuitive for the operator.

In this work the finite element method is used to solve the physics behind transcranial stimulation. In the case of TMS, we solve Faraday's law of induction to translate the magnetic fields into electric fields. After, we can solve the Laplace equation within

the conductive medium to obtain the induced electric field. Similarly, in the case of tDCS, one can directly solve the Laplace equation given that the current source is in contact with the conductive medium.

In general, setting up an FEM problem involves three steps:

1. Define geometries in which the physical phenomena will take place.

2. Define material properties in what we call *subdomains* (parts that compose our geometry which can show different physical characteristics). In particular, when simulating transcranial stimulation, the subdomains are the different tissue layers, i.e. skin, bone, cerebro-spinal fluid, gray matter and white matter. The stimulating element also constitutes a subdomain (e.g. coil or electrodes). In the case of TMS, one must include an additional "air" subdomain encompassing all other geometries, to allow magnetic induction.

3. Define the appropriate inner (within the geometry) and outer boundary conditions.

Once the problem has been set, solving the model comes down to a linear system of equations. For doing this, there are number of direct or iterative solvers, which will be discussed in more detail later in this chapter.

In TMS, the forward problem consists in defining the stimulation parameters, namely coil current, polarity, waveform and frequency, along with its position and orientation. In tDCS, one needs to define the electrode's position, polarity and current density. For both stimulation cases, one must define the conductivity of the different tissue layers and the nature of the conductive medium, whether it is homogeneous or heterogeneous, isotropic or anisotropic and if displacement currents occur.

In the context of transcranial stimulation, the solution to the forward problem can provide insight into the extent in which the given stimulation parameters are able to reach the desired cortical targets in terms of induced field distribution and magnitude. The forward solution can help adjust parameters when they require minor changes. If this is not the case and the treatment has to change substantially, it is adequate to think about approaching the inverse problem, which will be covered in the next chapter.

2.2 Quasistatic condition

An important consideration when modeling fields in tissue is that, since TMS pulses are up to 10 kHz and tDCS is mostly applied in frequencies close to DC, we can assume a quasistatic condition. This is based on the three reasonable assumptions discussed below.

The first quasistatic assumption is that the induced electric field follows the same time course in the entire brain. This can be verified by obtaining the wavelength of the electromagnetic energy during TMS λ_{TMS}. For typical dielectric properties in human head λ_{TMS} is at least two orders of magnitude higher than the human head's dimensions [49], [50]. Therefore, we can expect no significant phase variations with the induced electric field at any location in the brain.

The second assumption is that the tissue can be modeled as purely resistive, i.e. the capacitance of cell membranes is sufficiently small to be neglected. Particularly, the time for charges to accumulate at the boundaries where conductivity changes can be negligible [49],[51]. To verify this, we know that the charge density decays inside the human head with a time constant ϵ/σ [50], i.e. the capacitive component of the conductivity, with ϵ being the permittivity and σ the conductivity in tissue. If we consider the ratio between this time constant and the duration of a TMS pulse (ca. 100 μs), we can measure the validity of this assumption. The ratio is in the range of 10^{-2} to 10^{-3}, which indicates that the charge accumulation at conductivity boundaries can be considered to occur without delay.

The third assumption involves the induced currents in the brain, which also generate a magnetic field that can oppose that of the TMS coil. The effect of these eddy currents is also negligible, given that they are much smaller than those in the TMS coil [51],[50]. Therefore, we can neglect the inductive effects of tissue and consider only the magnetic field generated by the coil.

2.3 Physics

The Biot-Savart law can describe the time-varying magnetic flux density $\vec{B}$ in a TMS coil generated by a time-varying electric current I [52],[50]:

$$\vec{B}(\vec{r},t) = \frac{\mu_0}{4\pi} I(t) \oint_C \frac{\vec{dl} \times (\vec{r} - \vec{r}\,')}{|\vec{r} - \vec{r}\,'|^3}, \tag{2.1}$$

where $\vec{r}$ and $\vec{r}\,'$ determine the displacement vector and the location where the integration is taking place along the coil, C is the path of current flow, $\vec{dl}$ is a vector whose magnitude is the length of the differential element along the coil in the direction of conventional current. μ_0 represents the magnetic permeability of free space.

Under the aforementioned quasistatic condition we can describe the induced electric fields using Faraday's law of induction, which states the core physical principle of TMS: a circulating electric field $\vec{E}$ is caused by a changing magnetic flux density $\vec{B}$, expressed in differential form by Maxwell [53], [54] and satisfying:

$$\vec{\nabla} \times \vec{E} = -\frac{\partial \vec{B}}{\partial t}. \tag{2.2}$$

Where the $\vec{\nabla}$ operator stands for the gradient $\frac{\partial}{\partial x}\hat{i} + \frac{\partial}{\partial y}\hat{j} + \frac{\partial}{\partial z}\hat{k}$, with unit vectors $\hat{i}, \hat{j}, \hat{k}$ for each of the three dimensions. The Ampère equation relates the magnetic flux density $\vec{B}$ with the current density $\vec{J}$ in the coil (considering displacement currents in tissue negligible)

$$\vec{\nabla} \times \frac{\vec{B}}{\mu} = -\sigma \vec{E} = -\vec{J}, \tag{2.3}$$

σ stands for the electric conductivity tensor for the different tissue layers in the head and μ is the permeability of tissue, considered very close to that of air and homogeneous in the entire head. The magnetic flux density $\vec{B}$ can be defined by a circulation of the magnetic vector potential $\vec{A}$ [55]:

$$\vec{B} = \vec{\nabla} \times \vec{A}. \tag{2.4}$$

If we substitute this into Equation 2.2 we rewrite Faraday's law as [56]:

$$\vec{\nabla} \times \vec{E} = -\frac{\partial}{\partial t}(\vec{\nabla} \times \vec{A}), \tag{2.5}$$

$$\vec{\nabla} \times (\vec{E} + \frac{\partial \vec{A}}{\partial t}) = 0. \tag{2.6}$$

Given that brain tissue is heterogeneous, the induced electric field results from two components: (1) the magnetic vector potential $\vec{A}$ (whose source is the TMS coil) generates the primary induced electric field $\vec{E}_p$ and (2) the electric scalar potential

V accounts for the accumulated charges at the boundaries where the conductivity changes and constitutes the secondary induced electric field $\vec{E}_s$ [54], [57]

$$\vec{E} = -\frac{\partial \vec{A}}{\partial t} - \vec{\nabla} V, \tag{2.7}$$

$$\vec{E}_p = -\frac{\partial \vec{A}}{\partial t},\ \vec{E}_s = -\vec{\nabla} V. \tag{2.8}$$

Ohm's law describes the constitutive relation between current density $\vec{J}$ and electric field $\vec{E}$. The equation of continuity implies that the divergence of the current density is zero, i.e. the amount of current that enters the brain is the same amount that exits the brain.

$$\vec{J} = \sigma \vec{E}, \tag{2.9}$$

$$\vec{\nabla} \cdot \vec{J} = 0, \vec{\nabla} \cdot (\sigma \vec{E}) = 0. \tag{2.10}$$

$$\vec{\nabla}(-\sigma \frac{\partial \vec{A}}{\partial t} - \sigma \vec{\nabla} V) = 0,\ \vec{\nabla} \cdot \sigma(\vec{E}_p + \vec{E}_s) = 0. \tag{2.11}$$

In the case of tDCS, since there is no contribution from the coil, the Laplace equation (Equation 2.11) only has the contribution of the electric scalar potential, therefore:

$$\vec{\nabla} \cdot (-\sigma \vec{\nabla} V) = \vec{\nabla}^2 V = 0. \tag{2.12}$$

Where the $\vec{\nabla}^2$ is the Laplacian $\frac{\partial^2}{\partial x^2}\hat{i} + \frac{\partial^2}{\partial y^2}\hat{j} + \frac{\partial^2}{\partial z^2}\hat{k}$. The air/tissue boundaries satisfy the Neumann boundary condition:

$$\vec{n} \times \vec{A} = 0, \tag{2.13}$$

$$\vec{n} \cdot \vec{J} = 0, \tag{2.14}$$

i.e. the normal component of the magnetic field potential, and respectively, the current density at the surface is zero. Where $\vec{n}$ is the unit vector normal to the interface. At the interface between two different conductivity media, the boundary condition follows the continuity of the magnetic field $\vec{H}$ and induced current [57]:

$$\vec{n} \times (\vec{H}_1 - \vec{H}_2) = 0, \tag{2.15}$$

$$\vec{n} \cdot (\vec{J}_1 - \vec{J}_2) = 0. \tag{2.16}$$

In tDCS, we define the stimulating current as an inward current flow at the electrode,

with J_n specifying the magnitude

$$\vec{n} \cdot (\vec{J_1} - \vec{J_2}) = J_n. \tag{2.17}$$

For the reference electrode, the electric potential at the corresponding boundary is set to zero

$$V = 0. \tag{2.18}$$

2.4 Finite element method (FEM)

The motivation for the FEM arose from the fact that there are no closed-form solutions when dealing with physical phenomena affecting more complex geometries than well-known structures (e.g. ellipsoids, spheres, cylinders and cubes). The FEM's core idea is to divide the problem into small parts and use numerical methods to come to a solution by approximating the partial differential equations (PDEs) with algebraic equations. If the PDEs are linear, then a linear system of equations can be constructed and the desired output field function can be obtained using the so-called *solvers*. This applies to steady state problems like the ones presented in this work.

To discretize the geometries, we must choose a basis function to describe the finite dimensional subspace. These functions are typically piecewise linear or polynomial. Fig. 2.1 shows the representation of an FEM problem in one dimension. The 1D geometry is discretized as well as the continuous field function $F(x)$, which is approximated at each of the elements using piecewise linear functions.

Once the geometry has been discretized, the PDEs can be solved as a function of the geometrical locations or nodes. Subsequently, a process called FE-assembly constructs a global matrix conformed by local element matrices, in order to have a global equation system where all unknown variables on the nodes can be solved. Each node is shared by a variable amount of elements. Each element linked to a node contributes to the unknown field function value. The system of equations $Ax = b$ consists of the resulting matrix from the assembly A, called the *stiffness matrix* (the name inherited from structural mechanics), x which represents the unknowns, and the *load vector* b, which contains information defined a priori, such as boundary conditions.

The unknowns of a discretized finite element model are called degrees of freedom

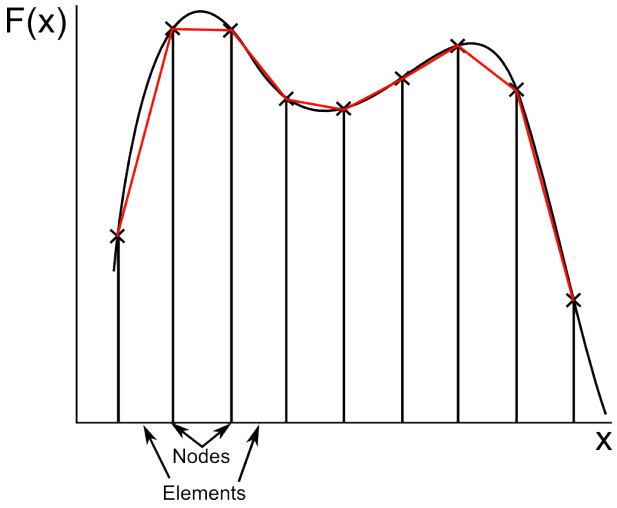

Figure 2.1: FEM problem in one dimension showing the nodes, elements and the field function approximated by piecewise linear segments (shown in red).

(DOFs). Each element in the discretized geometry has several DOFs which depend on the topology and structure of the mesh. The DOFs allow to describe the complexity of a model. Fig. 2.2 shows a flow diagram that summarizes the process of solving model using the FEM.

By discretizing problems FEM can deal with geometries of high complexity, which has consolidated it as the method-of-choice to predict a variety of physical phenomena. Originally in the 1950's FEM dealt with structural analysis of stress/strain in the aeronautical industry, but it quickly spread to other areas such as electromagnetism and fluid dynamics.

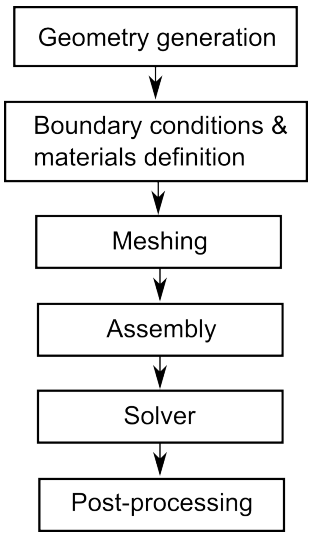

Figure 2.2: Flow diagram for solving a model with FEM.

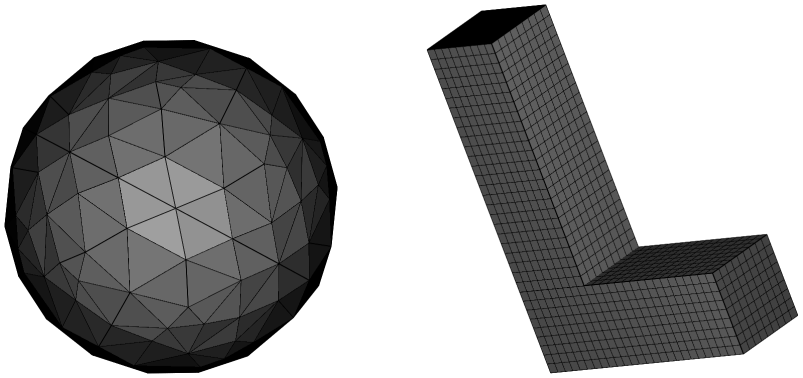

(a) (b)

Figure 2.3: Types of meshing for FEM geometries. (a) Tetrahedral unstructured mesh and (b) quadrilateral structured mapped mesh.

2.4.1 Mesh

The discretization is done by generating a sequence of nodes which describe the geometry in question. These nodes are connected to each other forming a finite number of elements. There are several ways to generate meshes. Quadrilateral elements can be used, however, the process to generate those meshes can be time consuming. Another kind of mesh makes use of triangulation in order to generate triangles (2D) or tetrahedra (3D) as elements. When generating a mesh, the location, order of the elements and their connectivity needs to be specified. This information is subsequently used when creating the algebraic representation of the problem. On the one hand, meshes can be *structured*, when they are mapped (using interpolation) and all elements maintain the same topology. On the other hand, meshes can also be *unstructured*, which means the elements follow no specific topology and can be connected in different patterns. These are called free meshes and have become well-established, given that its generation is more flexible and it can be readily automated yielding good results. Fig. 2.3 shows examples for a tetrahedral free mesh and a mapped structured mesh.

A wide variety of meshing software has become available in the last decade, with features which can increase the accuracy of the FE calculations, like for example, assigning higher mesh densities at regions of interest. In general, the difference in the physical phenomena between a discretized model and the real system, that is, the discretization error, becomes smaller as the element size decreases [58].

2.4.2 Solvers

There are two main types of algorithms known as *solvers* :

- **Direct solvers**

  These are algorithms which employ Gaussian elimination using a finite sequence of operations with few tuning parameters. They are well-suited for solving 1D and 2D problems as well as simple 3D problems, where the geometries are not complex (roughly less than 100,000 DOFs). As the problem size increases their memory usage and computation times also show a fast increase, making them impractical. Some well-known direct solvers are: SPOOLES, UMFPACK, PARDISO and Cholesky among others [58].

- **Iterative solvers**

  These algorithms work with an initial guess for the unknowns and successively update their values in order to approximate the solution making it more accurate until a set of convergence criteria is met. Iterative solvers require preconditioners, which are algorithms to simplify the stiffness matrix A. Depending on the quality of the preconditioner, they can be time consuming. However, they are able to handle much bigger problems than the direct solvers (roughly above 100,000 DOFs depending on available memory). Some well-known preconditioners are: LU factorization, Geometric Multigrid and Algebraic multigrid. Each preconditioner has certain qualities that makes it more suitable for a given problem and has a direct effect on the amount of iterations the solver will require to reach convergence. Some common iterative solvers include: Conjugate gradients, GMRES, Geometric multigrid and BiCGStab [58].

2.5 Other methods for calculating electric fields

Besides the FEM, there are other available methods for solving the forward problem in bioelectromagnetics, in this case computing the induced electric fields in conductive media. A list of the most notable methods is presented, along with their main attributes.

- **Boundary element method (BEM)**

  A method commonly used for calculating induced electric fields [59] and in general physical phenomena is BEM, where only the boundaries need to be discretized and the PDE's are formulated as integral equations. BEM uses the boundary conditions to fit boundary values into the integral equations, rather than through the entire space. In the post-processing stage the integral equations are also used to calculate the solution of the interior points in the subdomains.

  While BEM formulations result in fully populated matrices, in FEM, the resulting matrices are normally simpler, often exhibiting sparseness. This fact makes BEM computations to grow quadratically as the problem size increases, in contrast to the linear growth observed in the FEM. For this reason, there is a compromise with model complexity, where FEM becomes the method of choice when handling large and complex models. This is the case for the models presented in this work, which are composed of hundreds of thousands till millions of tetrahedral elements. Another shortcoming of BEM is that it does not allow to model anisotropic materials, which can be an important feature, later addressed in this chapter.

- **Finite difference method (FDM)**

  FDM is as well a numerical approach based on iterative solvers coupled with relaxation techniques which has been used in the context of TMS [60], [61], and more recently [62], [63]. The procedure calculates the potential at each point as the average of the neighboring elements. This process is repeated until the solution reaches convergence. Given that this method is an approximation technique, it has been shown that it may oversimplify the computation when dealing with complex geometries [64]. However, an advantage is that it is relatively easy to implement.

- **Impedance method (IM)**

  Electric field calculations based on the IM are composed of a uniform cartesian grid comprised of cubical elements or voxels which can correspond directly to

a segmented image. For each voxel one can define a 3D resistance network of impedances for which the Kirchoff's voltage law can be applied around each loop in the network. A loop is composed of the four edges of the cube's face. When simulating TMS, the loop currents are governed by Faraday's law of induction. When simulating electric stimulation, one can directly assign the electrode applied currents according to Kirchoff's law. Once the loop equations have been generated, one can solve a linear system using a variety of available methods [65]. The major advantage of using IM is that the meshing of the geometries can be spared and one can work, for example, directly with the segmented structures from MRI. The major caveat is that the linear system of equations can often be ill-conditioned, which leads to long convergence times or no solution at all. In [66] the authors propose an independent impedance method, which formulates the loops in a way to produce healthy matrices for the solver, also reducing computation times.

- **Analytical solutions**

One can also come to analytical solutions by applying the formulations presented in past sections on simplified geometries and sources. In [67] and [68] the authors present analytical solutions for the induced electric field due to magnetic sources for unbounded, semi-infinite, cylindrical and spherical models. Such formulations are useful for obtaining rough estimates of how the electric field distribution actually looks like in reality. However, when dealing with realistic and in general more complex model geometries, it is necessary to employ the methods described in the past sections, for which no closed-form solution for Maxwell's equations exist and therefore must rely on numerical techniques.

Chapter 3

Non-invasive transcranial stimulation

This chapter addresses the fundamental principles of non-invasive transcranial stimulation. There are two main sections covering the techniques analyzed in this work, i.e. transcranial magnetic stimulation (TMS) and transcranial direct current stimulation (tDCS). The mechanisms which allow each technique to modulate neural function are explained along with the required technical parameters which dictate the stimulators output and therefore an associated physiological response. Subsequently, the state-of-the-art methods for delivering stimulation and enhancing its focality are described.

3.1 Transcranial stimulation

The first reported experiments using electric stimulation of the brain go back to the ancient Greeks and Romans [69]. In the last two centuries, many other researchers have explored the use of electric currents in the brain to treat mental disorders reporting varying results [70],[21]. Nowadays, brain stimulation is applied in different modalities, all having a similar objective: to modulate neuronal function in a way to alter its current state and therefore yield improvements in a given medical condition, or simply to understand how the brain actually works, when inhibiting or facilitating certain brain function. An important characteristic about transcranial stimulation is its magnitude, which can either be supra-threshold, i.e. directly activating (depolarizing) neurons, or sub-threshold, i.e. when it modulates neural

function through other mechanism not directly involving activation.

In this work, we focus on improving the present methods to deliver transcranial stimulation of the brain, in the quest of achieving better and more specific results. In the past two decades, several types of transcranial stimulation modalities have emerged. We list the different modalities, briefly explaining their main characteristics:

- **Transcranial magnetic stimulation (TMS)**. Coil that drives a rapidly changing magnetic field inducing an electric field in the brain in supra-threshold levels.
- **Transcranial electrical stimulation (TES)**. Electrodes on the scalp which induce currents in supra-threshold levels.
- **Transcranial direct current stimulation (tDCS)**. Electrodes on the scalp which induce direct currents in sub-threshold levels.
- **Transcranial alternating current stimulation (tACS)**. Electrodes on the scalp which induce alternating currents in sub-threshold levels in a frequency-specific fashion.
- **Transcranial current stimulation (tCS)**. General concept that encompasses TES, tACS and tDCS.

In the following sections of this chapter we will cover in more detail the two transcranial stimulation techniques of most importance in this work: TMS and tDCS.

3.2 Transcranial magnetic stimulation (TMS)

3.2.1 Basic principles

In 1985, Barker *et al.* [71] were able to successfully stimulate the motor cortex non-invasivavely through the use of pulsed magnetic fields. A TMS device consists of a stimulating coil connected to a high-voltage (400 V - 3 kV) and high-current (4 kA - 20 kA) discharge electronic circuit [72]. In a traditional setup, the coil is placed above the head tangentially. The stimulation of the brain is achieved through the principle of electromagnetic induction, where a time-varying magnetic field produced by the stimulating coil enters the head with minimal attenuation to

induce an electric field in the brain. Contrary to its name, it is not the magnetic field but the induced electric field in brain tissue which rapidly hyperpolarizes or depolarizes neural tissue [73] depending on axon orientation, as well as on the relative orientation of the coil to the gyri [74],[11].

TMS is applied in two modalities:

1. **Single pulse TMS (sTMS)**, which can depolarize neurons transiently and is used primarily to functionally map the regions of the motor cortex [75]. It is used to evaluate the integrity of nerve conduction along the path to the corresponding muscle representation. This can be achieved measuring the response of the muscle in the form of a motor evoked potential (MEP) which can be recorded using electromyography. One can then calculate the corticomotor latency between the stimulus and the response, as well as the size (amplitude or area) of the MEP [76]. sTMS is used as a diagnostic tool to measure activity and function in patients who suffer stroke, spinal cord injuries, Parkinson's disease, multiple sclerosis, among other neurological disorders [72].

2. **Repetitive TMS (rTMS)** consists of a train of pulses applied repetitively. They cause a maintained excitability change, in contrast to sTMS where the effect is transient. This excitability change, also called "conditioning effect" [76], can be either excitatory or inhibitory depending on the parameters of stimulation, namely, frequency, intensity, duration, pulse shape and train length. rTMS is used therapeutically for treating a variety of psychiatric and neurological disorders such as depression [77], Parkinson's disease [36], epilepsy [37]. rTMS has also been extensively used in research to study cognitive and behavioral neuroscience [3] as introduced in Chapter 1.

A particularly important property of TMS is the stimulus waveform, which can be monophasic or biphasic. A monophasic pulse shows current flow in only one direction, while in a biphasic pulse the current flows in both directions. The shape of the waveform is of a damped sinusoid which is influenced by the electronics of the stimulator, namely, the capacitance, inductance and resistance [78]. Differences while stimulating have been identified for the two waveforms. Monophasic pulses show a stronger orientation sensitivity of the coil than biphasic pulses. Moreover, biphasic pulses are known to improve the efficiency of stimulation, requiring lower stimulation thresholds relative to monophasic (ca. 30% difference in MEP amplitude) [79]. The more sophisticated stimulator design described in [80] allows to

deliver near-rectangular waveforms, controlling their pulse-width while reducing the required energy as well as coil heating.

The geometry of the stimulating coil plays a critical role in the outcome of TMS, since it determines the spatial specificity or focality of stimulation and the capacity of the energy that can be delivered. The two most common coil geometries are the round and the figure-of-eight coils. The round coil consists of several windings arranged in a circular fashion, whereas the figure-of-eight coil is basically two round coils placed next to each other. The current in the two round coils that conform the figure-of-eight, flows in opposite direction. This is in order to create a magnetic field hotspot exactly in the middle of the coil (see Fig. 3.1). Note that the induced currents flow in opposite direction to the current in the coil.

3.2.2 How TMS affects the brain

TMS is capable of modulating neural function by inducing a suprathreshold electric field in the brain by means of a time varying magnetic field. In principle, the induced electric field affects both intracellular and extracellular spaces, and those parts of the neuronal cell membranes in which charges accumulate are potential loci for hyperpolarization or depolarization [81]. In reality however, the exact cellular mechanisms of how TMS affects neurons and its ability to elicit a sustained excitability modulation (known as the conditioning effect of rTMS) are still an open question. This has been shown by considerable inter-subject and inter-session variation in the induced excitability of rTMS [82],[83]. The observed variation has several potential systematic sources: (1) those having an influence on the time of the stimulus pattern such as frequency and stimulation duration; and (2) those having an influence on the spatial distribution and orientation of the induced electric field in the brain, such as coil geometry, pulse shape and coil orientation to the head while stimulating [78]. The most commonly accepted mechanism for explaining the conditioning effect of TMS is synaptic plasticity, in the form of long term potentiation (LTP) or long term depression (LTD) [84].

TMS could be compared to transcranial electrical stimulation (TES), a technique which can also induce supra-threshold stimulation by placing electrodes on the scalp and applying high electrical currents that flow through the skin and subsequent layers before reaching the brain. In contrast to TES, TMS affects the brain with minimal sensation on the scalp and the induced electric field is not as influenced by the different tissue layers. That is partly because in TMS, the induced currents are

predominantly tangential to the surface of the brain. In TES the direction of the induced currents can have both tangential and normal components to the surface of the brain. The so-called "shunting" of the current between the two electrodes is as well present, in the skin and cerebrospinal fluid layers, due to their higher conductivity in relation to the brain and bone.

3.2.3 Focality in TMS

Focality of stimulation constrains the achievable spatial resolution of TMS. Focality in TMS can only be achieved in two dimensions. This means the induced electric field maximum will always be at the surface of the brain, at the boundaries where the conductivity changes. This issue has been studied in [67], where the authors mathematically prove that it is not possible to produce a local maximum of electric field strength inside the brain using any superposition of external current sources.

A common measure of the focality in TMS is the surface area bound by the half-maximum of the induced electric field [85]. Fig. 3.1 shows the induced electric field for the two most common used coil geometries, namely, round and figure-of-eight coils. These plots were obtained from simulations placing a conductive block parallel to the bottom of the coil. We can observe that the figure-of-eight coil offers better focality than the circular coil. This is because the maximum induced electric field on a circular coil is under the windings with minimal induced field in the center, whereas in a figure-of-eight coil the maximum is located in the center of the coil, where the windings come close together generating a hotspot. Another feature of the figure-of-eight coils is that they can reach higher induced electric fields (of course at the cost of using more energy). In [86], the authors evaluate the focality and efficiency of two commonly used commercial figure-of-eight coils. They concluded that both coils show similar characteristics, however, reporting that both focality and efficiency are highly dependent on the coil-to-cortex distance, as well as the cortex radius.

Even though figure-of-eight coils offer better focality, circular coils are still used widely. This is because clinicians do not have the means to place the coil reliably at a given position. Many TMS users still hold the coil manually or use instruments to keep it in place. However, it is very likely the patient will move (at least slightly) during the TMS session, which makes it hard to keep the figure-of-eight coil positioned at the target. For this reason clinicians rather use diffuse stimulation with the circular coil to make sure they hit the desired target [87].

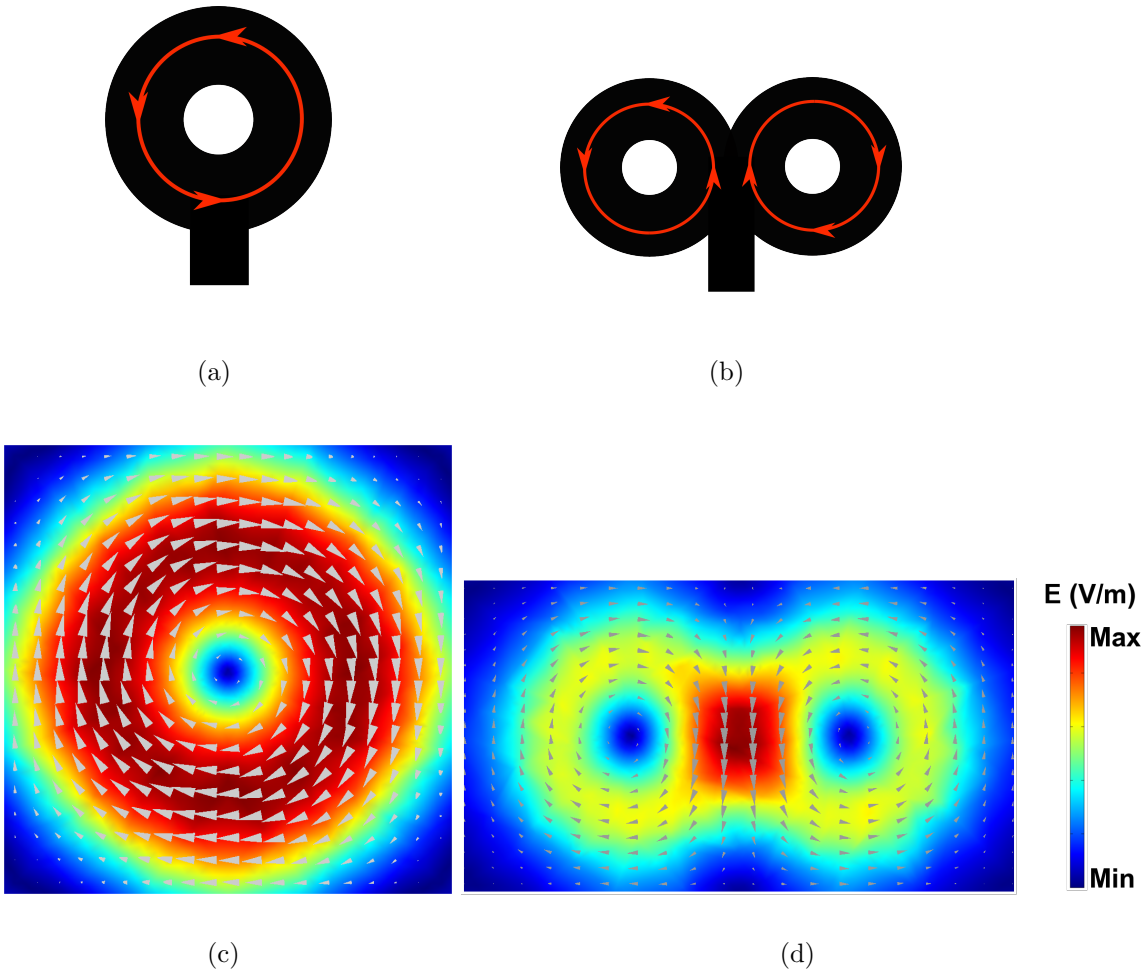

(a) (b)

(c) (d)

Figure 3.1: Induced electric field of the two most common TMS coil geometries. (a) Diagram of the round coil and (b) figure-of-eight coil. The red line with the arrows indicates the direction of the current in the coil. (c) Induced electric field E of round coil and (d) figure-of-eight. Red denotes higher field intensity, whereas blue, lower. Note that the induced currents are in opposite direction to the current in the coil. The gray cones illustrate the direction of the induced current. Plots were generated using the simulation software COMSOL Multiphysics (COMSOL AB, Sweden).

Our group has developed a neuro-navigated robotic TMS system [75],[88],[89], which has solved the coil positioning problem, using a robotic arm which not only precisely places the coil at the target, but compensates any patient movement with the aid of a tracking system, making sure the coil maintains the correct position as well as the appropriate orientation to the head surface (usually tangential). Using more sophisticated positioning systems like robotic TMS, focal stimulation can be exploited and more ambitious experiments can be carried out.

For TMS in the rat, focality plays an important role given the reduced dimensions of

the rat. TMS experiments are often performed on rats before humans. Motor evoked potentials (MEP) in the rat were investigated in [90]. Lateralization of forelimb MEP by TMS in the rat was recently analyzed [91]. Neurotransmitter modulation after repetitive TMS has been studied on rats [6], [5], as well as seizure inhibition effects [7]. In these experiments, researchers assume the stimulation of a particular target in the brain. However, due to the small dimensions of the rat brain, the stimulation affects undesired anatomical structures. This fact limits some of the experiments because their analysis cannot neglect the effect of other stimulated sites in the brain.

3.2.4 Focality improvement in TMS: state-of-the-art

- **Small coils**

  The most intuitive idea to improve focality is to reduce the dimensions of the stimulating coil and therefore make the magnetic field and (as a result) the induced electric field more confined. This idea is in principle possible, however there are two main physical limits which constrain the construction of small coils: (1) Having a small coil means that the length of the conductive wire will be reduced. This has an implication in the effective inductance of the coil, which will require more energy to produce an equivalent magnetic field compared to a coil with greater dimensions. Higher energy also translates into higher temperatures, which is destructive for the coil. (2) Given that higher currents are required to drive small coils, the Lorentz forces, product of the pulsing magnetic field (and also responsible for the mechanical distress producing the characteristic clicking sound in TMS) are destructive for the coil and its casing. For these two reasons, there has been limited improvement in the achievable focality. Nevertheless, these coils are available for research purposes, normally referred to as small animal coils. Simulations in [92] show that a 15 mm diameter figure-of-eight coil shows a 33% focality improvement over a 70 mm diameter figure-of-eight coil. The small coil, however, overheats and is only able to reach 45% of the maximum induced electric field of the larger coil.

- **Other coil geometries**

  Some researchers have proposed the use of alternative coil arrangements as a way to improve focality and penetration depth. In [93] the authors show dif-

(a) (b) (c)

Figure 3.2: Small coil compared to traditional coils. (a) Commercial small figure-of-eight-coil (dimensions: 10 cm x 5.5 cm) Medtronic MagPro MCB35 compared to (b) round coil Medtronic MagPro MCF75 (dimensions: 8.8 cm diameter) and (c) figure-of-eight Medtronic MagPro MCFB65 (dimensions: 17.4 cm x 9.4 cm). The three coils are from MagVenture A/S, DK (with friendly permission).

ferent configurations using several coils in a variety of orientations. The idea is basically to add the coils' magnetic fields in order to achieve a more suitable stimulation pattern. The result is, however, highly impractical. Increasing the coils in use increases the necessary driving power. Such arrangements are also much bigger than the conventional coils, which makes them heavy and cumbersome in a clinical environment. The authors of [94] proposed the H-coil, a combination of intricate wiring patterns, for which they claim to achieve stimulation at deeper brain regions. Further studies have measured the H-coil's induced electric field distribution and found that the figure-of-eight coil still performs better in terms of focality. The penetration depth is also not substantially better [95]. In [96], the authors integrated customized magnetic cores to the coil for guiding the magnetic flux. This can reduce the size of the coil and increase its inductance, but makes it heavy.

- **Shielding**

The use of a passive conductive shield in TMS was studied in [97], where it was used to suppress the surface electric field responsible for the unpleasant sensation in the scalp reported by some patients. The authors of [92] used a conductive shield plate on a figure-of-eight coil and significantly improved the localization of the electric field in their simulations. In [98], the concept of active shielding for TMS is proposed, where the authors take a figure-of-eight

coil and place another virtual figure-of-eight coil on top, which suppresses the unwanted components of the magnetic field in order to optimize focality and penetration. Unfortunately, the construction of such coil would have to deal with a higher energy demand as well as the Lorentz forces stemming from the two coils, which cause vibration and would be destructive for the coil and potentially harmful for the subject.

- **Linear superposition**

  Optimized TMS targeting was formulated in [99], applying the superposition of electric fields from multiple small coils. Unfortunately, using multiple adjacent coils simultaneously leads to the partial cancellation of their fields, which dramatically raises the energy requirement to drive such a system, making its realization impractical.

3.3 Transcranial direct current stimulation (tDCS)

3.3.1 Basic principles

Animal studies from the 1960s reported that weak electrical currents applied by intracerebral or epidural electrodes can increase or decrease neural excitability according to the current polarity. Depending on current intensity and duration of stimulation, these changes can be stable for hours after stimulation [100]. Since its successful application to the human cortex [101], transcranial direct current stimulation has received increasing attention from the neuroscience and clinical communities as a tool for modulating cortical excitability .

The conventional setup for delivering tDCS involves two sponge electrodes soaked in saline solution placed on the scalp. The *stimulating electrode* or *anode* is commonly placed above the motor cortex and the *return electrode* or *cathode* is usually placed on the contralateral orbit (see Fig. 3.3). When applying anodal stimulation in the motor cortex, TMS is routinely used to measure the excitability changes in the form of MEPs in the corresponding muscles.

A number of researchers have applied tDCS to study basics of cognitive and behavioral neuroscience [1],[48],[102],[47]. Its therapeutic potential in neurological

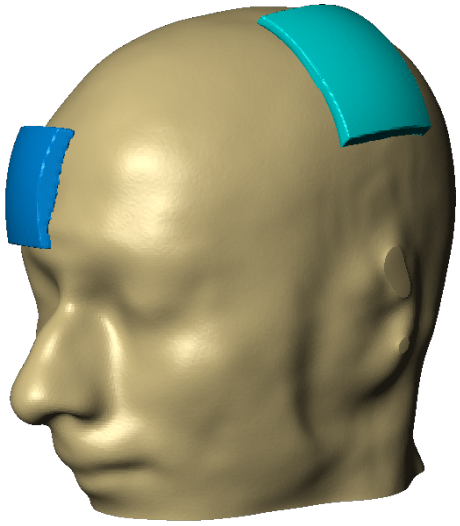

Figure 3.3: Conventional setup for tDCS with rectangular 35 cm^2 pads placed on the scalp. The anode is placed above the motor cortex region and the cathode is placed contralaterally above the eye orbit at the dorsolateral prefrontal cortex (DLPFC).

disorders has been explored: anodal stimulation has been suggested for treating the symptoms of major depression, Parkinson's disease and chronic pain. A survey of tDCS studies with stimulation parameters, namely, electrode placement, current strength, duration and outcome can be found on [2].

Although the tDCS research community has increasingly grown in the past years, the physiological mechanisms of how weak electrical fields affect brain activity are not entirely understood.

3.3.2 How tDCS affects the brain

In the past decade tCS has been applied most widely in the modality of tDCS. In contrast to other brain stimulation techniques, such as TMS, where a changing magnetic field induces an electric field to rapidly stimulate neural tissue, tDCS is considered a neuromodulatory method, where affected tissue is polarized and its excitability is modified [100]. In [103], the authors suggest this effect is due to a shift in resting membrane potential in cortical neurons. Applying extracellular uniform steady state direct current (DC) electric fields *in vitro* can modulate neuronal excitability in a time-dependent manner. This occurs as a result of the interaction between the different neuronal compartments leading to short and long-term changes in excitability and network function [104].

A fundamental difference between TMS and tDCS, is that the latter induces sub-

threshold stimulation, i.e. it does not depolarize neurons, in contrast to TMS, where the induced electric fields in the brain are suprathreshold and reach magnitudes in the order of 100 V/m [105],[11]. tDCS reaches magnitudes of ca. 1 V/m per 1 mA of applied current [8]. Yet interestingly, both techniques yield to similar effects outlasting the time of stimulation [106]. Additionally, in contrast to TMS, where induced currents are mostly tangential to the surface of the brain, one must note that in tDCS currents travel between both electrodes in the head, yielding both tangential and normal components of the induced electric field. tDCS can also reach deeper structures (with decreasing electric field strength) if the electrodes are apart. The maximum electric field strength however, is always at the surface structures. If the electrodes are close to each other, it will result in the shunting of the current through the scalp, decreasing the amount of current passing through the brain, which is undesired because it may also lead to increased sensation.

So far, tDCS experimental studies have been rationalized by the *somatic doctrine*, namely, the idea that radial inward or outward cortical currents under the anode or cathode induce pyramidal soma depolarization or hyperpolarization leading to increased or decreased excitability, respectively [101],[107]. However, it has been shown that tangential currents during tDCS are dominant even under the electrodes [9], [108]. This point, along with the finding that maximal polarization during uniform DC stimulation in vitro occurs at synaptic terminals, suggest that tDCS mechanisms of action are more intricate than the somatic doctrine [108].

There is increasing evidence supporting that weak electric fields can acutely modulate network activity [109], which can be manifested as small but coherent changes in firing rate and timing of neural populations. These effects can be magnified by dynamic network activity [110]. Experiments in vitro have also shown that mammalian pyramidal neuron somata polarize linearly in relation to small applied electric fields ($< |40|$ V/m) [104].

Pharmacological studies, where tDCS together with central nervous system drugs were applied have revealed insights into the cellular mechanisms of the induced neuroplasticity. In [111], the authors used Na^+-channel-blocking and a N-methyl-D-aspartate (NMDA) receptor antagonist. They monitored the motor excitability changes using TMS and found strong evidence suggesting the involvement of NMDA receptors in both types of DC stimulation induced plasticity, (i.e. *anodal* and *cathodal*), pointing out that polarity driven changes in membrane potentials play a crucial role in tDCS lasting effects. Modification of intracellular calcium levels has also been reported [112], [111], which is a shared effect with the well-studied plasticity phe-

nomena of long term potentiation (LTP) and long term depression (LTD).

3.3.3 Focality in tDCS

The modulation of brain function by tDCS results from a variety of factors: applied current, waveform, duration of stimulation, polarity, electrodes' size and positioning. Up to date, tDCS is delivered using two 35 cm^2 rectangular pads placed on the scalp. This montage is known to produce a highly diffuse distribution of the induced electric field in the brain. This has been shown in finite element (FE) studies addressing the induced effects of tDCS in spherical models [113], [114], and more recently in realistic models depicting the complex folding geometry of the brain [9],[8].

Achieving better focality, i.e. reducing the size of the stimulation locus, allows to improve the interpretation of the functional effects, because these are then restricted to a more clearly defined cortical area. Improved focality can also avoid unwanted reversed effects under the reference electrode, something of particular importance clinically, where often a shift in excitability in one direction is required [4]. Another important implication of focality is that in general, it may avoid side-effects caused by stimulating a variety of neighboring brain structures to the desired target.

The original reason for using the rectangular pads was to minimize sensation in the skin by minimizing current density. However, it has been shown that the use of large electrodes soaked in saline solution or using conductive gel does not guarantee reduced sensation [115]. A pruritic sensation is commonly reported after a threshold around 1 mA of applied current (charge density $\sim$ 340 C/m^2 [116]). This is due to the fact that the current in the electrode-skin interface is not uniformly distributed, and shows maxima at the periphery of the electrodes, the so-called edge-effect [115].

Achieving focality in deeper brain structures, like in TMS, has been shown to be not possible [67]. Whether the sources are magnetic or electric, no superposition of external currents can induce a local maximum inside the brain. The electric field maximum, like in TMS, will always be at the surface of the brain.

3.3.4 Focality improvement in tDCS: state of the art

- **Extracephalic reference**

The conventional tDCS montage involves two electrodes placed on the scalp. Under both electrodes the induced electric field will show its maximum, which means that there are two hotspots in the brain. This is undesired in the case the clinician or neuroscientist aims at stimulating a single cortical region. For achieving this, the use of an extracephalic reference has been proposed [4]. The concept has been applied in a rat model of tDCS [117]. Nevertheless, the scenario of having only one cortical region may not always be the best choice. For example, in treatment for stroke it may be desirable to have two symmetric contralateral hotspots at the motor cortex.

- **Increase reference electrode size**

Increasing the size of the reference electrode aims at eliminating its functional efficacy by reducing the current density flowing directly underneath [4]. Like the extracephalic reference, focality is improved by removing the second hotspot under the reference. Simulations illustrating this configuration were performed in [118].

- **Reduce electrode size**

A third alternative is to reduce the size of the stimulating electrode while maintaining the current density constant [4]. This may yield discomfort in the form of a pruritic sensation or pain due to the temperature changes and activation of nerve fibers at the interface electrode-skin. New efforts in electrode design have shown that minimizing the size of the electrodes to a circular contact surface with ca. 12 mm diameter, and ensuring the right interface with the skin with conductive gel, one can safely stimulate for periods of ca. 20 minutes without skin irritation (see Fig. 3.4) [119].

- **4-by-1 electrode configuration**

The authors of [8] proposed the use of a ring configuration, the so-called 4-by-1 montage, consisting of one anode in the center and four cathodes placed around it. This configuration employs the small HD-tDCS electrodes described in [119]. Given the four return electrodes, the idea is to elicit one hotspot within

Figure 3.4: Ring electrode (12 mm diameter) for high-definition tDCS with casing and conductive gel for proper interface with the skin (with friendly permission from author [119]).

the ring. This has been shown in FEM simulations, where it has proven to improve focality against the conventional montage.

- **Optimized multi-electrode tDCS**

  The aforementioned methods are based on intuition about the behavior of the current density. Optimized multi-electrode tDCS belongs to a second generation of focality enhancement methods, where the brain is modeled as a resistive conductive medium and the superposition principle is used to model the applied currents from multiple electrodes placed in the scalp according e.g. to the international EEG 10/10 configuration. With this model one can solve the inverse problem of finding the appropriate electrode currents which elicit a predefined intensity of the electric field at a given location in the brain. Furthermore, one can specify the direction of the electric field at the target beforehand, which is an advantage given the a priori knowledge of the orientation of the pyramidal cells at the gyri in the brain. The authors of [12] established the foundations for this technique and showed substantial improvements against the conventional montage. The techniques later portrayed in this dissertation make use of these foundations.

Chapter 4

Electric field in conductive medium *in vitro*

For supporting the subsequent formulations in this work, it is important to establish: (1) the validity of our FEM simulations of the induced electric field and (2) the superposition of current sources in a conductive medium. In this chapter, we present the *in vitro* experiments to support these two points. We describe the experimental setup, display the results of the measurements and discuss their implications.

4.1 Superposition of electric fields

In order to corroborate that our simulations realistically represent the physics of conduction and set the basis for the multi-electrode stimulation approach later introduced in this work, we measured the superposition of multiple current sources. The superposition principle, commonly found in physics and characteristic of linear systems, is defined as:

$$F\big(\sum_{k=1}^{K} x_k\big) = \sum_{k=1}^{K} F(x_k), \tag{4.1}$$

implying that the response of a system F to a number of stimuli $(x_1, x_2, \ldots, x_K)$ is equal to the sum of the responses of the system to each of the sources individually. To validate this principle comparing it to our simulations, we set to measure the induced electric field in a conductive medium.

4.1.1 Experimental protocol

In order to apply an electric field to a conductive medium and be able to measure its spatial distribution with a needle electrode, our experiments must be in a medium in which we can control the electrical conductivity. Therefore, we chose saline solution as the medium, with a conductivity $\sigma = 9$ mS/m, given that one can control the conductivity by simply adding $NaCl$ to the solution and measure it with a pH-conductivity-measuring device, in our case the PCE-PHD (PCE Instruments UK Ltd. UK).

To achieve repeatable and reliable measurements we used a 5-axis stereotactic robot developed at our institute, i.e. the Spherical Assistant for Stereotactical Surgery, (SASSU) introduced in [120] and [121]. By using the SASSU one can approach the problem systematically, controlling relevant parameters such as electrode trajectories and timing for the measurements. For programming the SASSU, we employed its available library in MATLAB (Mathworks, Natick, MA).

A tungsten needle electrode was used (Alpha Omega GmbH, DE) to acquire the measurements, immersed ∼1 mm in the saline solution. The active and ground electrodes were made of copper (2 mm diameter, 20 mm shaft length, completely immersed in saline solution) and were energized with a current I_e= 60 μA using an Isostim current controlled stimulator (World Precision Instruments Inc. Sarasota, FL, USA). The recordings of induced voltage were pre-processed using a custom circuit to adjust the output impedance and make sure that the signal was in the dynamic range of the g.USBamp (g.tec medical engineering GmbH, Schiedlberg, Austria), the amplifier we used to measure the voltage signals and interface them to a PC. This amplifier allows its manipulation through a MATLAB library. In this way, we could control the SASSU and the measurement system in a single MATLAB script.

We applied a periodic signal and measured its energy average in time, i.e. its power P_d, in its discrete form given by:

$$P_d = \frac{1}{N_p} \sum_{n=1}^{N_p} |x[n]|^2 \tag{4.2}$$

where N_p is the number of samples for the processing window, $x[n]$ is the discrete voltage signal sampled at f_c =256 Hz. We then applied $\sqrt{P_d}$ in order to obtain the root-mean-square value of the signal. The use of a periodic signal allows to detect

and discard any kind of drift or offset easily by applying a high-pass filter. For our experiments we used a stimulation signal with frequency f_s =10 Hz, a low frequency for which the quasistatic condition applies.

The setup for the experiment is depicted in Fig. 4.1, next to the real scenario. The conductive medium was held in a petri dish with 10 cm diameter and 2 cm depth. The SASSU robot is responsible for driving the tungsten needle electrode through the conductive medium in order to obtain the distribution of the electric potential V and from that, the induced electric field $\vec{E}$ as follows:

$$\vec{E} = -\vec{\nabla}V = -\frac{\partial V}{\partial x}\hat{i} - \frac{\partial V}{\partial y}\hat{j} - \frac{\partial V}{\partial z}\hat{k}. \tag{4.3}$$

In a first experiment, the task is to validate the forward problem of taking two separate sources and measure their electric potential distributions with one of them active at the time. Subsequently, we activate both sources and compare the validity of the superposition. We calculate the error between the corresponding simulation and the acquired data.

As a second experiment we validate the inverse problem, that is, to obtain the needed current values from the sources in order to generate a given field intensity and orientation at a target. The theory for this case as well as the experiments will be covered in the subsequent chapters of this work.

4.1.2 *In vitro* measurements

Electric potential distribution measurements are depicted for the superposition of two current sources, where each source was measured individually and then the two of them simultaneously. Separate measurements and simulations are shown for source 1 and 2 in Fig. 4.2. We include diagrams depicting the location of the active source and ground, also showing the measurement area in the petri dish, denoted by a dotted square (Fig. 4.2a,b).

The superposition of the two sources is depicted in Fig. 4.3, where in a similar fashion we show a diagram of the active electrodes and ground (Fig. 4.3a), and the simulation and experimental measurement of both sources active simultaneously (Fig. 4.3b,c).

To quantitatively evaluate the validity of our measurements against the theoretical

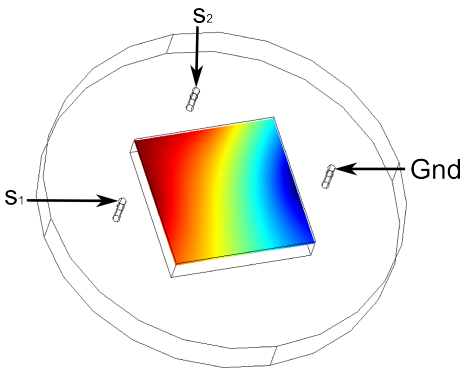

(a)

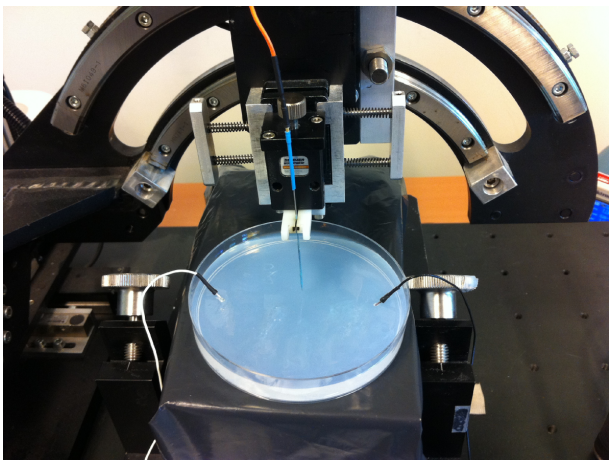

(b)

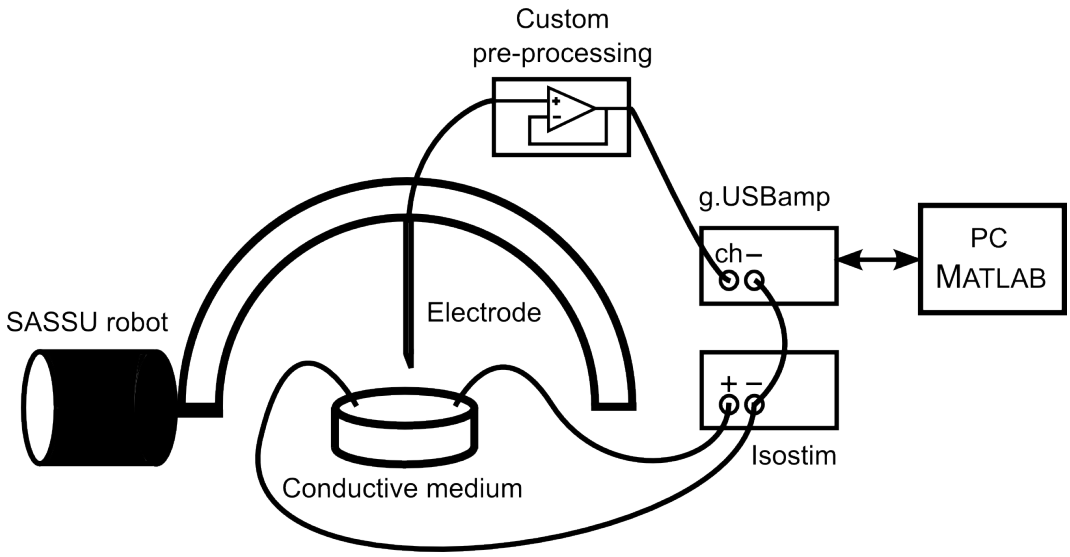

(c)

Figure 4.1: Experiment setup: superposition of fields in conductive medium in electrical stimulation. (a) Petri dish simulation for experiment showing the ground electrode and the two electrodes: source 1 (s_1) and source 2 (s_2), (b) real scenario in the laboratory and (c) diagram of the integrating blocks of the experiment. The SASSU robot drives the needle electrode in the conductive medium in synchrony with the acquisition of the g.USBamp (g.tec medical engineering GmbH, Schiedlberg, Austria). The current controlled stimulator Isostim (World Precision Instruments Inc. Sarasota, FL, USA) generates a periodic stimulating signal. The experiment is run by a single MATLAB script.

results, we show the plots of the normalized error for both of the sources in their individual measurements (Fig. 4.4a,b), as well as for their superposition (Fig. 4.4c). We note that the normalized error between simulation and measurement shows a maximum of 9.8% for source 1, 3.5% for source 2 and 7.6% for the superposition of sources. The measurements and simulations agree in their distribution and scale with minor differences attributed to environmental factors such as temperature and moisture, which can influence the conductivity of the *in vitro* medium, as well as to possible inhomogeneities in the saline solution.

In order to further validate the superposition principle in the medium, we compared the electric potential distributions resulting from the measurement of both sources being active simultaneously, i.e. $F(s_1 + s_2)$, with the arithmetic summation of the individual measurements, i.e. $F(s_1) + F(s_2)$. Ideally, both expressions should be equivalent. In Fig. 4.5 we show the normalized error between the two and observe that it shows a maximum error of 5.8%, with an average of 3.3%. This confirms that the superposition holds (with a marginal error). Another important aspect when performing experimental measurements is their repeatability. We measured this and exemplify two consecutive measurements, showing their normalized error. The repeatability error stays below 1% for the entire set of samples in the two measurements.

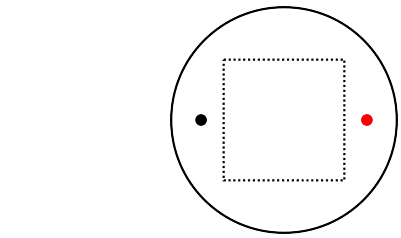

(a)

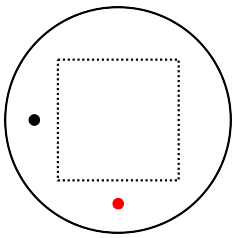

(b)

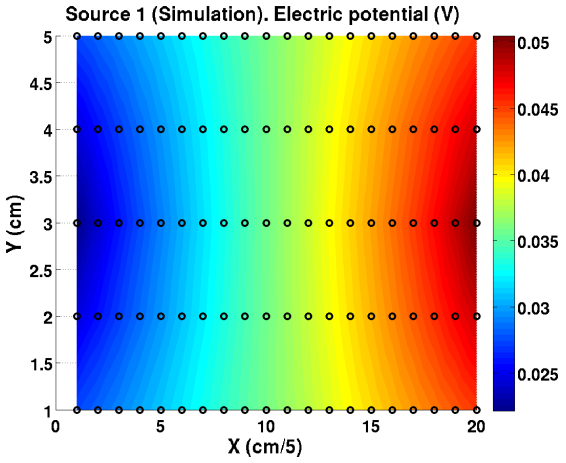

(c)

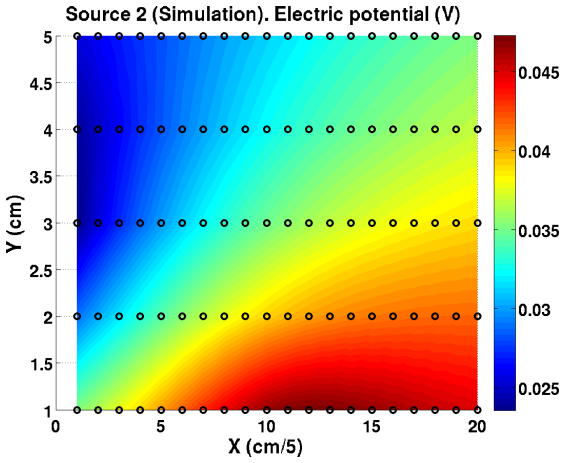

(d)

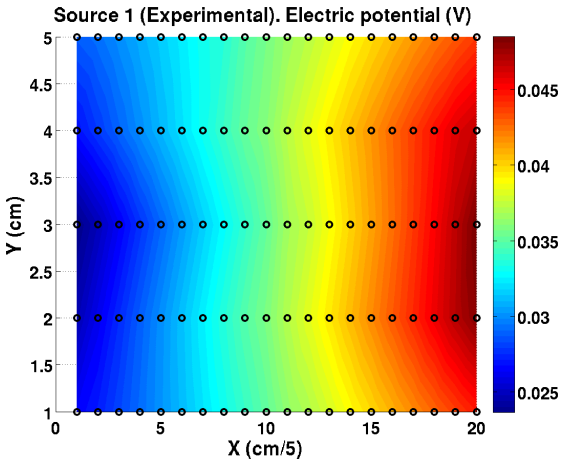

(e)

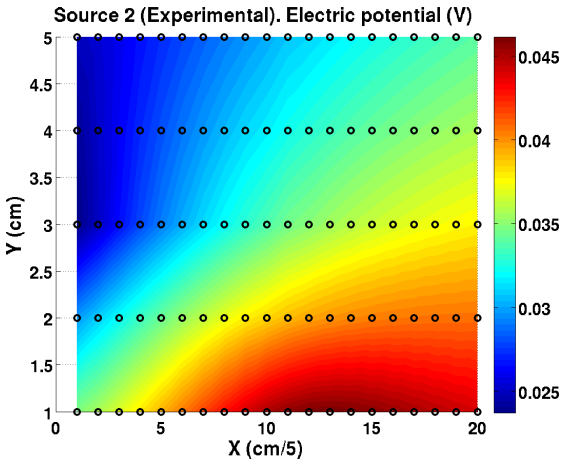

(f)

Figure 4.2: Experimental results: electric potential distribution in conductive medium, simulation vs. measurements for individual sources 1 and 2. (a), (b) Petri dish diagrams showing location and state of electrodes: active source (red circle) and ground (black circle). The dotted-line square is the measurements' area. (c), (d) Simulation and (e), (f) measurement of the distribution of the electric potential (black rings are measurement points).

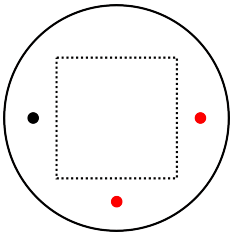

(a)

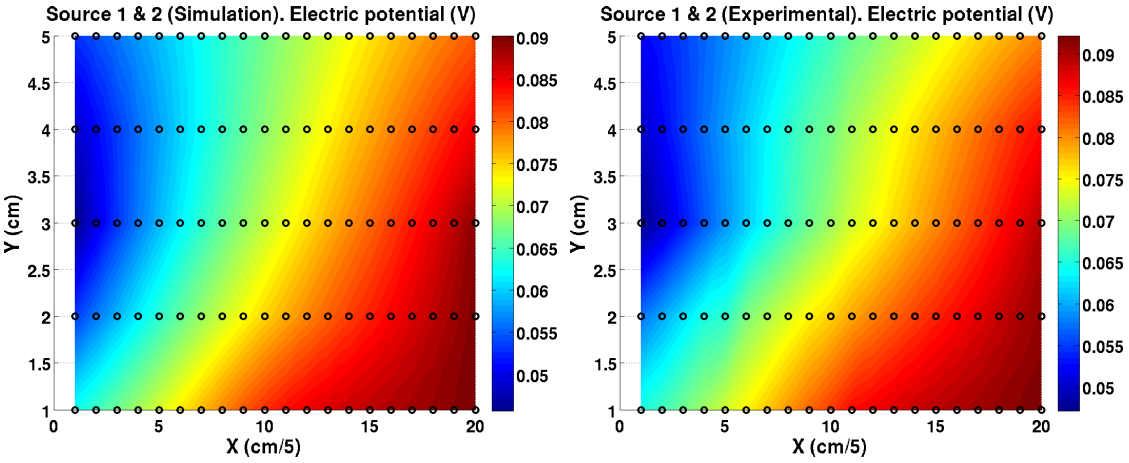

(b) (c)

Figure 4.3: Experimental results: electric potential distribution in conductive medium, simulation versus measurements for the superposition of sources 1 and 2. (a) Petri dish diagram showing location and state of electrodes in measurement: source 1 and 2 active (red circles) and ground (black circle). The dotted-line square is the measurements' area. (b) Simulation and (c) measurement of the distribution of the electric potential (black rings are measurement points).

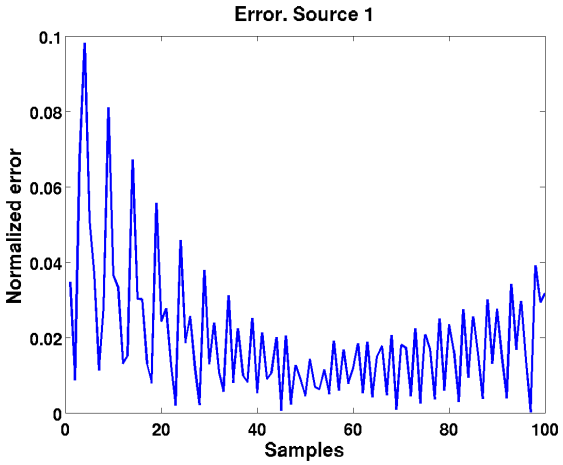

(a)

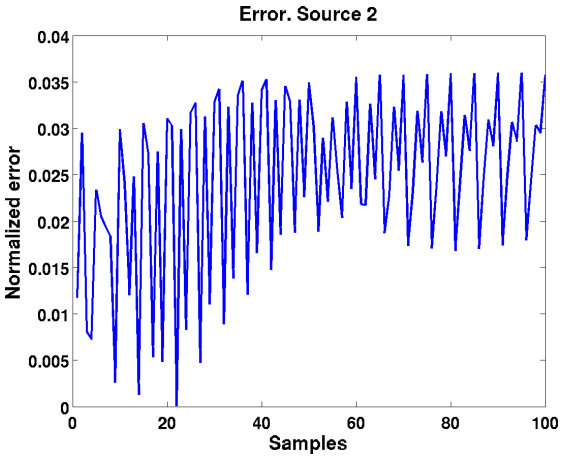

(b)

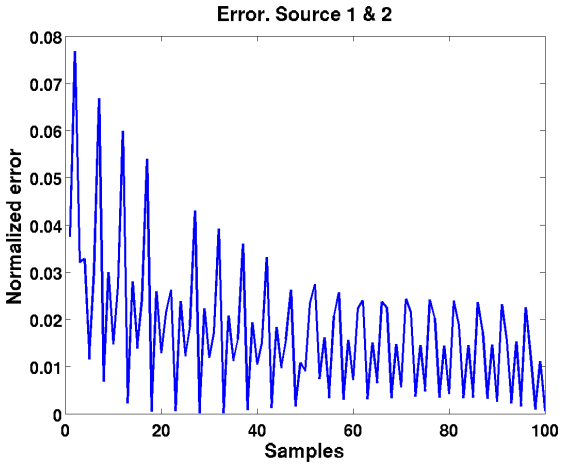

(c)

Figure 4.4: Experimental error: simulation versus measurement. Normalized error in relation to theoretical values (simulations) for (a) source 1, (b) source 2 and (c) superposition of sources 1 and 2.

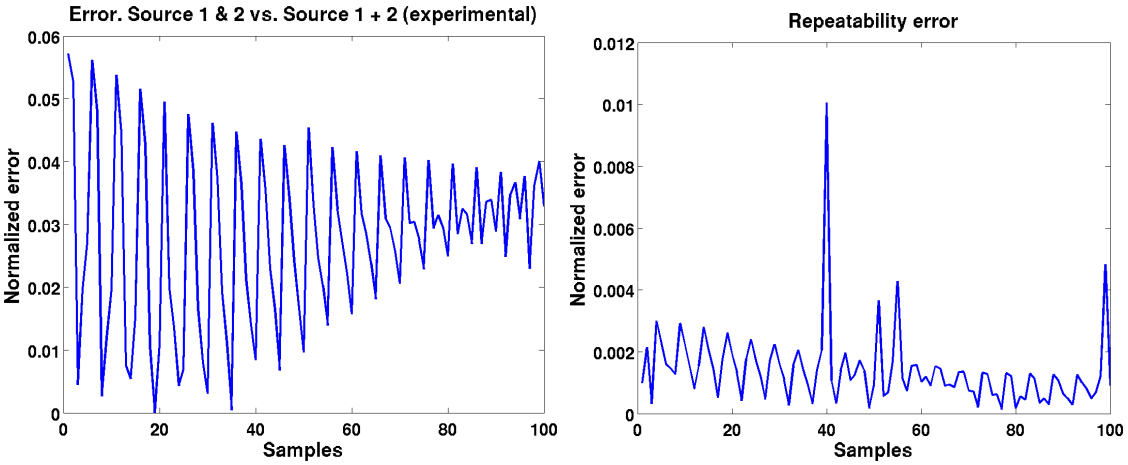

(a) (b)

Figure 4.5: Experimental evaluation: superposition and repeatability. (a) Normalized error comparing the superposition of the two sources when added individually or when measured at the same time (both sources active). (b) Normalized repeatability error exemplifying two consecutive measurements.

4.1.3 Implications

The experimental results for the forward problem were able to validate two important aspects for this work: (1) the finite element simulations we employ accurately describe the physics of the conduction phenomenon and (2) the linear superposition of sources is valid in an homogeneous conductive medium.

Our experiments were performed systematically with the use of the SASSU robot. This means we were able to reproduce the results under the same conditions, drive the needle electrode with the robot in a regular grid of measurement points, as shown by the repeatability error (Fig. 4.5).

The obtained *in vitro* results yield a simplified, yet reasonably realistic picture of the physics in a conductive medium. Although the measurements were acquired in a flat surface, the behavior we observed can be extrapolated to more complex geometries. The heterogeneity in different conductivity layers causes charge to accumulate at the interfaces; however, it does not influence the linearity required for superposing multiple sources. Linearity also holds for anisotropic conductivity, which can be integrated to our models as we discuss later in this work.

Chapter 5

Forward models[1]

In this chapter we present the animal and human forward models used in this work for simulating transcranial stimulation. The workflow for generating and solving the anatomically accurate models is explained in detail. Subsequently, an approach to analyze the direction of the induced electric field in the brain is introduced. The inclusion of anisotropic conductivity in a realistic model along with its implications are laid out. We present the technical details and context of two animal studies for which our models were used.

5.1 Anatomical models: background

Using realistic models plays an important role in the accuracy of the simulations portraying physical phenomena. Up until recent years in the FEM world, geometries were usually simplified to speed up computation times. However, in the advent of a new computation era, much more complex model geometries can be solved in reasonable time. No longer than a decade ago, homogeneous sphere head models started to be used, along with unbounded, semi-infinite, or cylindrical media [68].

Years later, researchers became aware that tissue heterogeneity, because of different tissue properties in the head, was of great importance to account for the accumulated charges at the boundaries between layers [57],[126]. Since then, head models using concentric spheres were used. Some groups still use them in their simulations [127],[128]. Such models, help gather insight into the induced currents in tissue.

[1]Parts of this chapter have been published in [122], [123], [124] and [125].

However, in the case of the human it has been shown that the complex folding of the cortex differs substantially from spherical approximations [11].

Model sophistication has advanced in the past few years and proved to increase the accuracy of the calculations [8],[9],[129],[130]. Anatomically realistic models have enabled a more thorough analysis of the electric field distribution in the brain, providing valuable information on the direction of the induced currents (which will be discussed later in this chapter) and the penetration and decay of the stimulation source.

5.2 TMS models

5.2.1 Conductive shield in TMS coil

The use of a passive conductive shield in TMS was studied in [97], where it was used to suppress the surface electric field which can cause discomfort during stimulation. Focalization in TMS has been addressed in literature mostly evaluating coil geometries and configurations [93], discussed in Chapter 3. The authors of [92] used a conductive shield plate on a figure-of-eight coil and improved the localization of the field in their simulations. We elaborated on this idea, which consists in using a conductive shield as a collimator placed between the TMS coil and the head to limit the amount of energy going through a window in the shield. We carried out simulations in different scenarios and report the first experimental results.

5.2.2 Simplified rat model

TMS experiments are often performed on rats before humans. Motor evoked potentials (MEP) in the rat were investigated by Luft *et al.* [90], lateralization of forelimb MEP by TMS in the rat was recently analyzed [91], neurotransmitter modulation after repetitive TMS has been studied on rats [6],[5], as well as seizure inhibition effects [7]. Some of these experiments assume the stimulation of a particular target in the brain. However, due to the small dimensions of the rat brain, the stimulation affects undesired anatomical structures as well. This fact limits some of the experiments because their analysis cannot neglect the effect of other stimulated sites in the brain.

There are limited studies addressing the TMS induced fields in small animals. In [131] a study on a realistic rat model showed the electric field distribution for two common coil geometries. The authors of [132] studied the electric field distribution in a realistic homogeneous mouse model, and analyzed its dependence on coil size, geometry and orientation.

As a first step investigating the use of the conductive shield plate, this section presents an analysis of the induced electric field in a four-layer simplified rat head model. The use of a conductive shield plate to improve field focalization (as introduced in [92]) is evaluated. The induced electric field was calculated through FEM simulations. We hypothesize that use of a shield plate can improve the state-of-the-art of TMS experiments in the rat by allowing the stimulation of specific structures.

Simulation

The induced electric field was calculated using the electromagnetics quasistatics variant of the AC/DC module from COMSOL Multiphysics 3.5a (COMSOL AB, Sweden). The software computes the solution for $\vec{A}$ and V through the FE method, assuming a sinusoidal current source with a frequency of 5 kHz and a voltage of 3 kV. The 3D geometries of the simulation are shown in Fig. 5.1a. The rat head consists of four concentric ellipsoids which account for the scalp, bone, CSF and brain. Each layer is 1 mm thick near the short axes and 2 mm near the long axes. The brain's long and short axes are 2.8 cm and 1.4 cm respectively, similar to the rat's real dimensions [133]. The coil has round shape with a 5 cm diameter and 4 turns. Its copper wire has a cross-sectional diameter of 3 mm. The surrounding air was modeled as a sphere of 15 cm diameter. The coil was placed perpendicularly 7 mm above the vertex of the outer ellipsoid as shown in Fig. 5.1b.

The conductive shield is simulated as a copper disk with 7 cm diameter and 3 mm thickness. The window in the disk is circular and was evaluated with five different diameters ranging from 10 mm to 30 mm. The shield plate was placed between the rat's head (2 mm above) and the coil. The window in the conductive shield plate was placed concentric to the vertex of the outer ellipsoid.

The geometries were meshed and solved iteratively. Tissue was considered isotropic and the conductivity values were referred to those of the human, as in [105]: $\sigma_{scalp} = 0.465$ S/m, $\sigma_{bone} = 0.01$ S/m, $\sigma_{CSF} = 1.654$ S/m, $\sigma_{brain} = 0.126$ S/m (white matter)

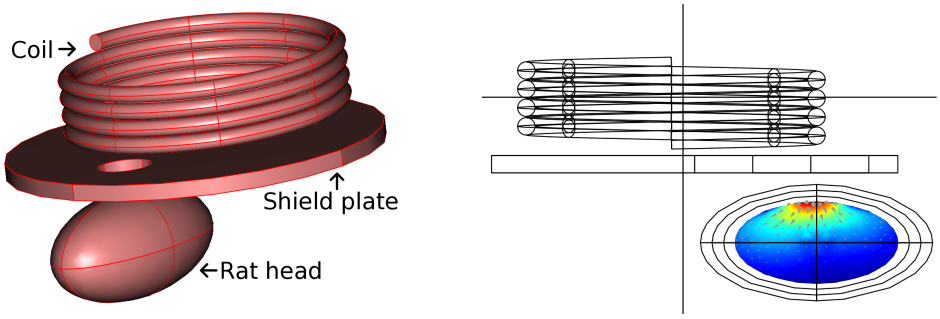

(a) (b)

Figure 5.1: Simulation geometries: TMS coil with conductive shield plate in simplified rat model. (a) Coil, shield plate and simplified rat head model and (b) lateral view of geometries depicting the 4 layers in the head model, i.e. skin, skull, CSF and brain.

and $\sigma_{air} = 0$ S/m.

To compare the results, a simulation of the coil without the shield plate was computed. The coil was placed exactly at the same location as in the simulations with the shield plate.

The focalization of stimulation can be measured with the half power region (HPR)[92], defined as

$$||\vec{E}|| \geq \frac{max||\vec{E}||}{\sqrt{2}}, \tag{5.1}$$

i.e. the field elements above 70.7% of the maximum induced electric field. To account for the HPR in 3D, the expression *HPR ratio* is used, namely, the ratio of 3D elements of the brain satisfying condition 5.1, to the total number of 3D elements of the brain.

5.2.3 Realistic rat model

For building the realistic 3D model, we obtained MRI data from a 450g living male Wistar rat (240 cross-sectional slices, 320 x 320 voxels with resolution of 0.3 x 0.3 x 0.2 mm, Philips Achieva 3 T, Neuroradiology UKSH Lübeck). Brain and head contour were subsequently segmented and exported as surface meshes to COMSOL Multiphysics (COMSOL AB, Sweden), where they were converted to solids. The model is composed of scalp, and brain tissue (Fig. 5.2). Since magnetic fields enter the head with minimal attenuation, the simulation using a homogeneous model of the

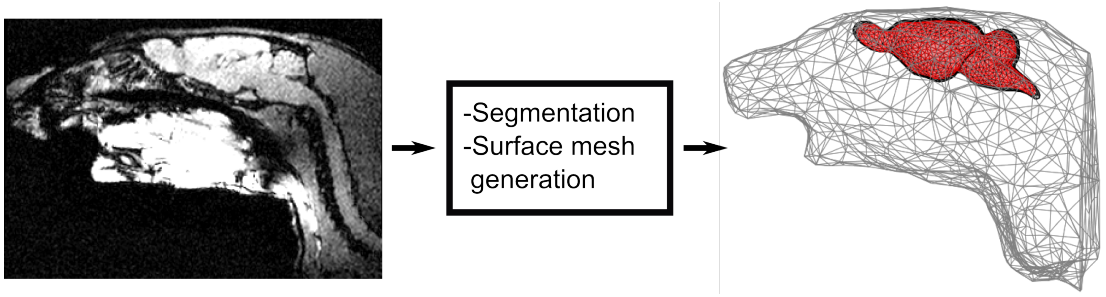

Figure 5.2: Realistic model of the rat head. Diagram illustrating the three steps for a simulation with an MRI-based realistic model of the rat: MRI data acquisition, segmentation and surface mesh generation and FEM simulation.

rat scalp and brain provides a reasonably realistic representation of the stimulation scenario, given that most of the charge accumulation during TMS occurs at the scalp-air interface, adequately considered in the model.

The rat scalp and brain were modeled as homogeneous, isotropic volume conductors and were assigned the conductivity of $\sigma_{brain} = 0.33$ S/m, corresponding to averaged gray matter conductivity values found in literature, and used in a similar FEM study [134].

The induced electric field in the brain calculated with COMSOL results from the sum of two components: the field induced by the coil itself, given by Faraday's law of induction, and the field given by the charge accumulation at the different conductivity interfaces (Section 2.3).

The boundary condition for all outer boundaries was defined as electrical (Equation 2.14) and magnetic insulation (Equation 2.13), i.e. zero normal current density at the surface. Continuity of the normal component of the current density was given to all inner boundaries (Equations 2.16 and 2.15). The coil was energized applying current J_n to the respective edge elements, taking into account the direction of the current flow.

5.2.4 TMS experiments: electric field measurements

To validate our simulations applying the conductive shield plate, we measured the induced electric field from two common TMS coils with and without using the conductive shield. For this, we devised an electric field sensor capable of measuring the electric field in two orthogonal axes x and y. The sensor consists of a 10 mm diameter PVC cylinder (non-conductive) with 150 mm length as shown in Fig. 5.3b

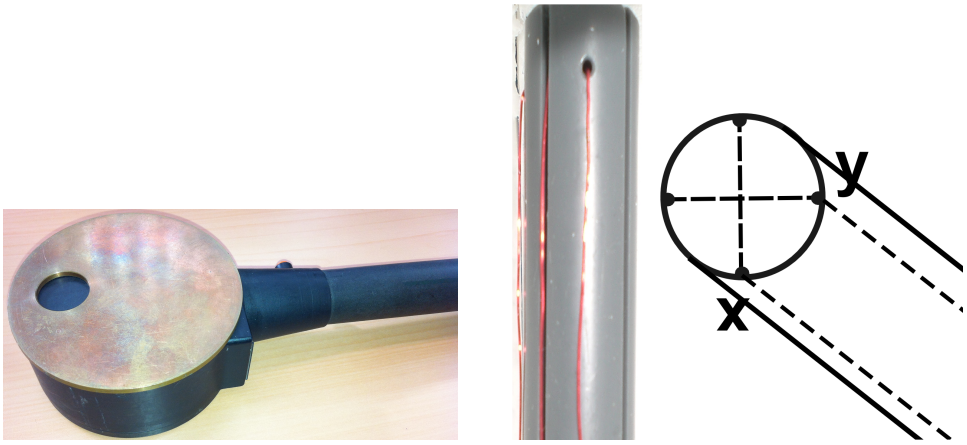

(a) (b)

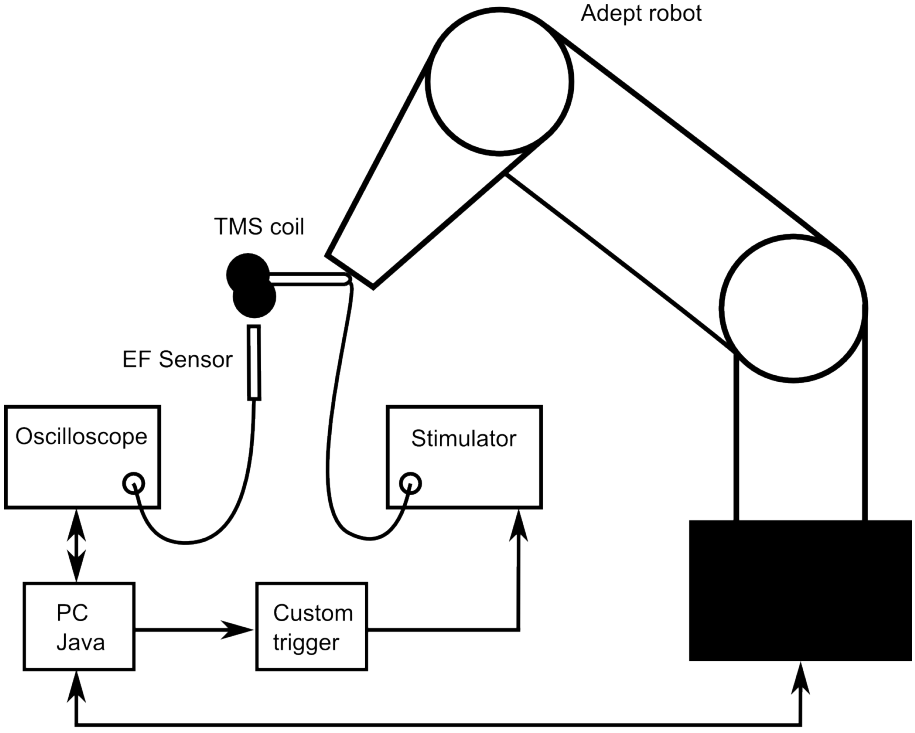

(c)

Figure 5.3: Experiment setup: measurement of the induced electric field by TMS coil with conductive shield. (a) Medtronic MagPro MCF75 circular coil with copper shield plate with 20 mm diameter circular window. (b) Electric field sensor consisting of a cylindric PVC tube with guides for two orthogonal wires at the top. (c) Diagram of the experimental setup showing the robot that drives the TMS coil in a grid measured by the electric field sensor connected to the oscilloscope. The PC triggers the stimulator to synchronize each measurement with the TMS pulse.

with two orifices at the top end. At these orifices one can insert a conductive wire in each of the two axes. We had the two wires go through the orifices and bent them so that they form a 90° angle going down the PVC cylinder.

It is important to note that we only measure the x and y components of the electric field, given that the induced field from the TMS coil in the z direction is negligible [51]. Each of the sensor axes' wires is connected directly to an Agilent oscilloscope DS06014A (Agilent Technologies Inc, USA) where we measured the peak induced voltage. We established a TCP/IP connection with the oscilloscope so that we could read the peak values from the induced voltages on a PC. In order to synchronize the TMS stimulator and the measurement of the oscilloscope, we used a custom-made circuit board to trigger the Medtronic MagPro Stimulator X100 (MagVenture A/S, DK).

In order to obtain a map of the induced electric field by the coils, we used an industrial robot to position the coil in a grid and synchronized the three interacting elements, namely, stimulator, oscilloscope and robot with custom software written in *Java*. The complete setup for the experiment is shown in Fig. 5.3.

We obtained measurements for the two most common coil geometries, namely, the circular coil Medtronic MagPro MCF75 and the figure-of-eight-coil Medtronic MagPro MCB35. Each measurement was achieved by driving the robot in a predefined grid of positions (with the coil in its end-effector) while the electric field sensor remained static and attached to the oscilloscope acquiring each grid point.

5.3 tDCS models

5.3.1 tDCS in the rat

Using the tDCS rat model defined in Section 5.2.3, we investigated the effect of implantation depth and focality for two electrode configurations modeled similarly to those used in [135]. We positioned the electrodes in reference to bregma, which was localized by visual inspection of the MRI data. The electrodes were modeled as stainless steel cylinders with 1.57 mm diameter and 2.4 mm shaft length. The electrode configurations were: (1) two-electrode configuration (Fig. 5.4 left), where the electrodes were aligned to bregma symmetrically in a coronal plane, 4 mm into each hemisphere (lateral: $\pm$ 4 mm), one electrode being the anode

and other the cathode, and (2) the three-electrode configuration (Fig. 5.4 right), where a third electrode was placed 2.5 mm anterior to bregma and used as anode (anteroposterior: + 2.5 mm). The other two are cathodal electrodes and their location was the same as in the two-electrode configuration.

In both configurations the electrodes were implanted in the skull. We investigated three scenarios for the electrodes' implantation depth: (a) at the surface of the skull (Fig. 5.4d), (b) halfway through the skull and (c) through the skull and in contact with the CSF. The current applied for the two-electrode configuration in scenario (a) was 15 μA, giving a maximum current density of s_{max}=0.241 A/m^2 in the brain. For purpose of comparison, the applied currents for the rest of the simulations were adjusted so that the maximum current density would equal s_{max} at the surface of the brain.

The geometries were meshed and solved iteratively using the conjugate gradients linear system solver (relative tolerance of 1x10^{-6}). The models were composed of above 1.5x10^5 tetrahedral elements and 2x10^5 degrees of freedom.

5.3.2 Realistic human model

Model generation

The realistic model of the human head was obtained from MRI data of a 26 year old male (180 cross-sectional slices, 240 x 240 voxels, each with size 1 mm x 1 mm x 1 mm, Philips Achieva 3T, Neuroradiology UKSH Lübeck). Brain, skull and scalp contours were extracted using the FSL software (Oxford, UK). Subsequently, tissue segmentation was done using Simpleware's ScanIP software (Simpleware Ltd, Exeter, UK) through the built-in region-growing algorithm and careful manual correction.

The electrodes of the international EEG 10/10 configuration were drawn in computer aided design (CAD) according to the positioning described in [136] (10% distance increments on the surface of the head from nasion to inion, as well as from the left to the right preauricular points), and imported to Simpleware's ScanCAD, where they were properly placed in the head model and converted to a segmentation mask (Fig. 5.5b). This same step was performed the other two electrode configurations used in this model: the conventional rectangular pads (Fig. 5.5a) and electrode patch arrays (Fig. 5.5c,d). The electrodes of the international EEG 10/10 configuration

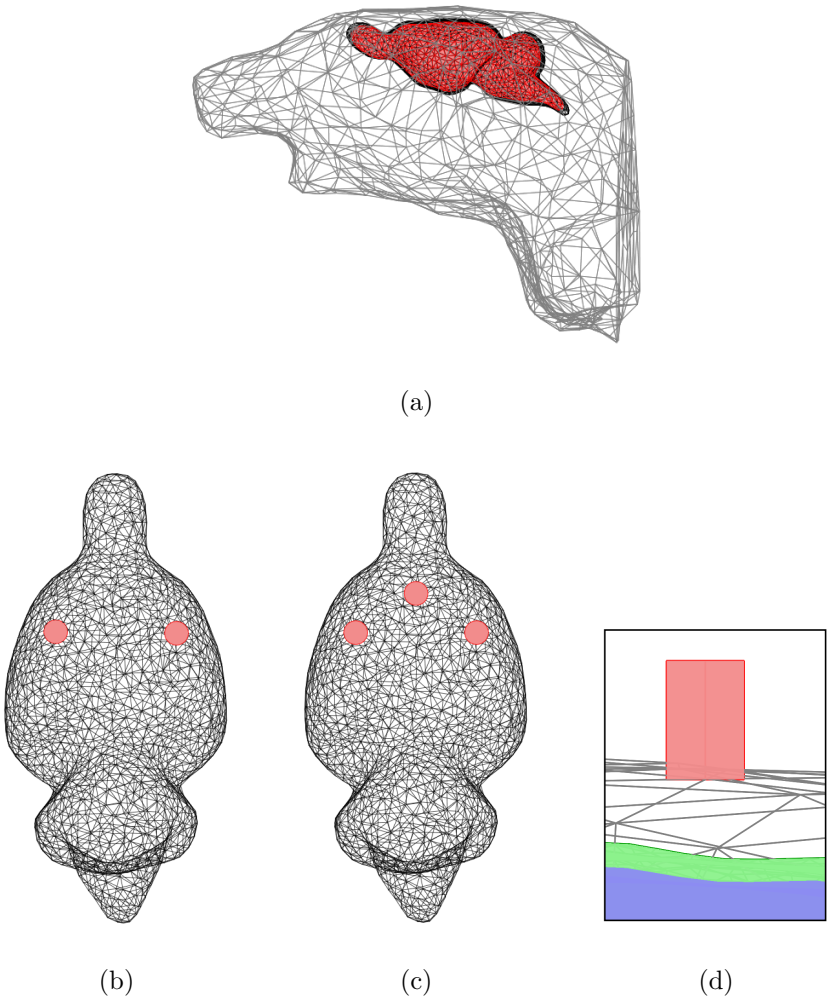

(a)

(b) (c) (d)

Figure 5.4: Realistic rat model for tDCS simulations. (a) Surface mesh of the rat head model with brain and CSF, (b) two-electrode configuration with both electrodes at the height of bregma, (c) three-electrode configuration with a third electrode 2.5 mm anterior to bregma (anode) and other two electrodes (cathodes) positioned as in (b). (d) Close-up at the electrode portraying the scenario "at the surface of the skull" with electrode (pink), CSF (green) and brain (blue).

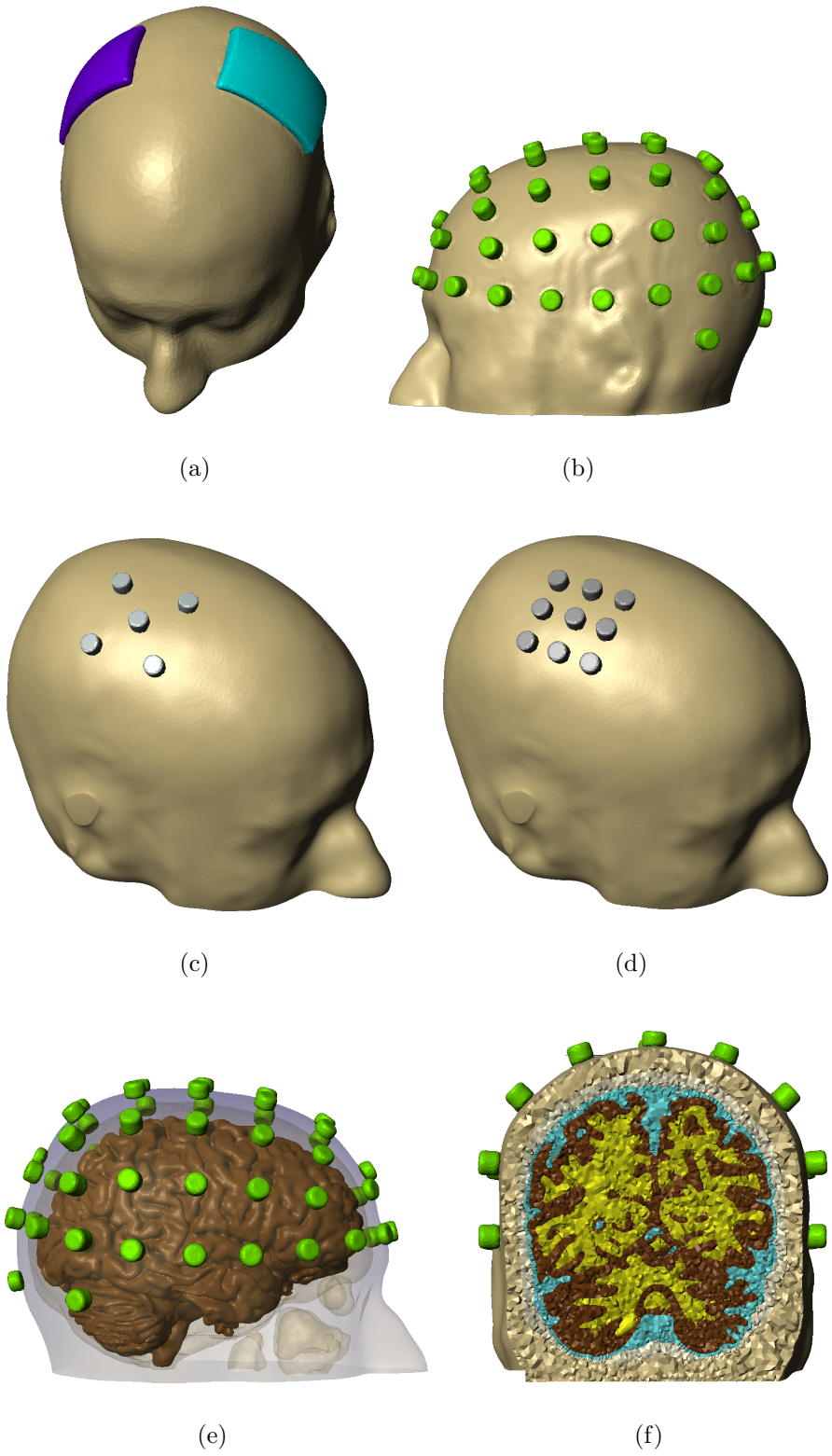

Figure 5.5: Realistic model of the human head for transcranial current stimulation. (a) Conventional 35 cm^2 pad montage, (b) multi-electrode configuration using EEG 10/10 standard, (c) 4-by-1 and (d) 3x3 patch arrays of electrodes. (e) Convoluted brain cortex in model and (f) different tissue types: white matter (yellow), gray matter (brown), CSF (blue), bone (white), scalp (light brown).

and patch array were modeled as cylinders with 10 mm diameter and 7 mm shaft length, whereas the rectangular pads' size was 7 cm x 5 cm. The last step of the process was to re-import the models to ScanIP, where a volume mesh considering all material types was generated, resulting in ca. $1{\times}10^6$ tetrahedral elements. The final models were composed of scalp, skull, cerebrospinal fluid (CSF), brain, eyes, airways and electrodes (Fig. 5.5e,f).

Simulations

The distribution of the induced electric field by the different tDCS configurations was calculated using the Conductive DC Media module from COMSOL Multiphysics 3.5a (COMSOL AB, Sweden). The media is considered isotropic and the electric conductivity is taken from averaged human values used in a similar FE study [114], i.e., $\sigma_{scalp} = 0.465$ S/m, $\sigma_{bone} = 0.01$ S/m, $\sigma_{CSF} = 1.65$ S/m, $\sigma_{brain} = 0.2$ S/m, $\sigma_{air} = 1 \times 10^{-16}$ S/m. The electrodes are given the conductivity of the scalp.

All outer boundaries fulfill the Neumann boundary condition, following electrical insulation, i.e. zero normal current density (Equation 2.14). Continuity of the normal component of the current density was assigned to all inner boundaries (Equation 2.16). The active electrodes were given an inward current flow boundary condition (normal current density J_n, Equation 2.17), whereas the reference electrode was given the ground condition (Equation 2.18).

5.3.3 Direction of induced electric field

tDCS is thought to induce long-term plasticity in humans [47],[137]. This plasticity is assumed to stem from synaptic changes mainly in the presynaptic terminal. However, clinical and cognitive tDCS studies have been rationalized based on the influence of direct current stimulation on somas [107]. If we ignore the complex folding of the human cortex, under the anode electrode current flows radially into the brain and exits through the cathode electrode radially as well, however, the convoluted surface of the brain changes the direction of the induced fields significantly, exhibiting both radial and tangential components as shown in computational models [9],[114].

Animal studies have shown that radial current flow can create polarity-specific effects modulating excitability: inward current causes somatic depolarization and increases

neural activity, whereas outward current causes somatic hyperpolarization and reduces neural activity [138],[139],[100]. This is because the dependence on pyramidal soma polarization, which is what we refer to as *somatic doctrine*. However, several studies have pointed out that the neuromodulation effects of tDCS may be more complex, e.g. tangential current flow to the cortical surface polarizes synaptic afferents rather than pyramidal somas in vitro [104], [140].

To gather further insight into the role of other non-somatic mechanisms in the neuromodulation effects of tDCS as well as the polarization in the cortical sheet, we studied the direction of the induced electric field in an anatomically accurate FEM model of the head developed following the steps described in Section 5.3.2. We analyzed two aspects:

1. **Normal versus tangential component**

   Previous studies have highlighted the fact that indeed, there is significant presence of both normal and tangential components in the induced electric field under the stimulating electrodes [9],[114]. However, to our knowledge, no study has quantitatively assessed which component is more prevalent under the electrodes and other regions in the brain, for example, between the electrodes along the cortex, where high magnitudes of the electric field are also observed [8]. This is of particular relevance because of the neuronal activation dependence with the electric field orientation mentioned above, challenging the somatic doctrine which assumes that cortical currents are predominantly radial under the electrodes. Furthermore, understanding the extent of each vectorial component of the field in affected regions during stimulation can help clarify the underlying mechanisms of tDCS at a cellular level [108].

   The magnitude of the electric field distribution was calculated for the conventional tDCS montage (one anode and one cathode 5x5 cm sponge electrode, Fig. 5.6a) and the 4-by-1 montage (center anode and four surrounding cathodes, 1 cm diameter, Fig. 5.6b) [8]. The relative magnitude of the two components of the EF (radial and tangential) are quantified on field distributions in regions of interest under the electrodes (Fig. 5.6c,d) and in the interelectrode space. The ratio of tangential to radial (T/R) field magnitudes is used to describe the relative magnitudes in each region, such that $T/R > 1$ corresponds to greater tangential fields on average and $T/R < 1$ corresponds to greater

radial fields on average.

2. **Directionality of normal component**

In the context of tDCS during sleep, findings have shown that a relatively short period of stimulation (25 minutes) specifically when humans experience slow-wave oscillations (0.5 - 1 Hz) can have long-lasting plastic effects manifested in memory consolidation improvement [46],[47]. We took the configuration used in those experiments, involving two stimulating electrodes/anodes placed symmetrically at F3 and F4 and two returns/cathodes placed on the mastoids, i.e, M1 and M2 (10/20 EEG international configuration) as depicted in Fig. 5.6e .

The electric field polarization at the cortical sheet was calculated obtaining the dot product of the electric field vector with the normals to the cortical surface, that is:

$$\vec{E} \cdot \vec{n} = E_x n_x + E_y n_y + E_z n_z, \tag{5.2}$$

defining the normals $\vec{n}$ pointing inwards. Therefore, having a positive value in the projection of the electric field onto the normal means that current is flowing in (neurons are depolarized), whereas a negative value indicates the current is flowing out of the cortical sheet (neurons are hyperpolarized) [141].

In order to quantitatively asses the polarization in different regions of the cortical surface, eleven locations of the 10/20 EEG configuration were analyzed (Fig. 5.6f), namely, Fz, F7, F8, Cz, C3, C4, Pz, P3, P4, T3, T4. For each location we defined a region of interest within a 30 mm diameter sphere encompassing the corresponding gyri and sulci in the cortical sheet. Subsequently, the expression $\sum_{i=1}^{N_e} \vec{E_i} \cdot \vec{n_i}$ was calculated, where N_e is the number of finite elements in the region, yielding a value reflecting the magnitude and type of polarization at each region of interest. The expression 5.2 for the cortical sheet was obtained using COMSOL Multiphysics 3.5a (COMSOL AB, Sweden) and exported to MATLAB (Mathworks, Natick, MA), where it was postprocessed.

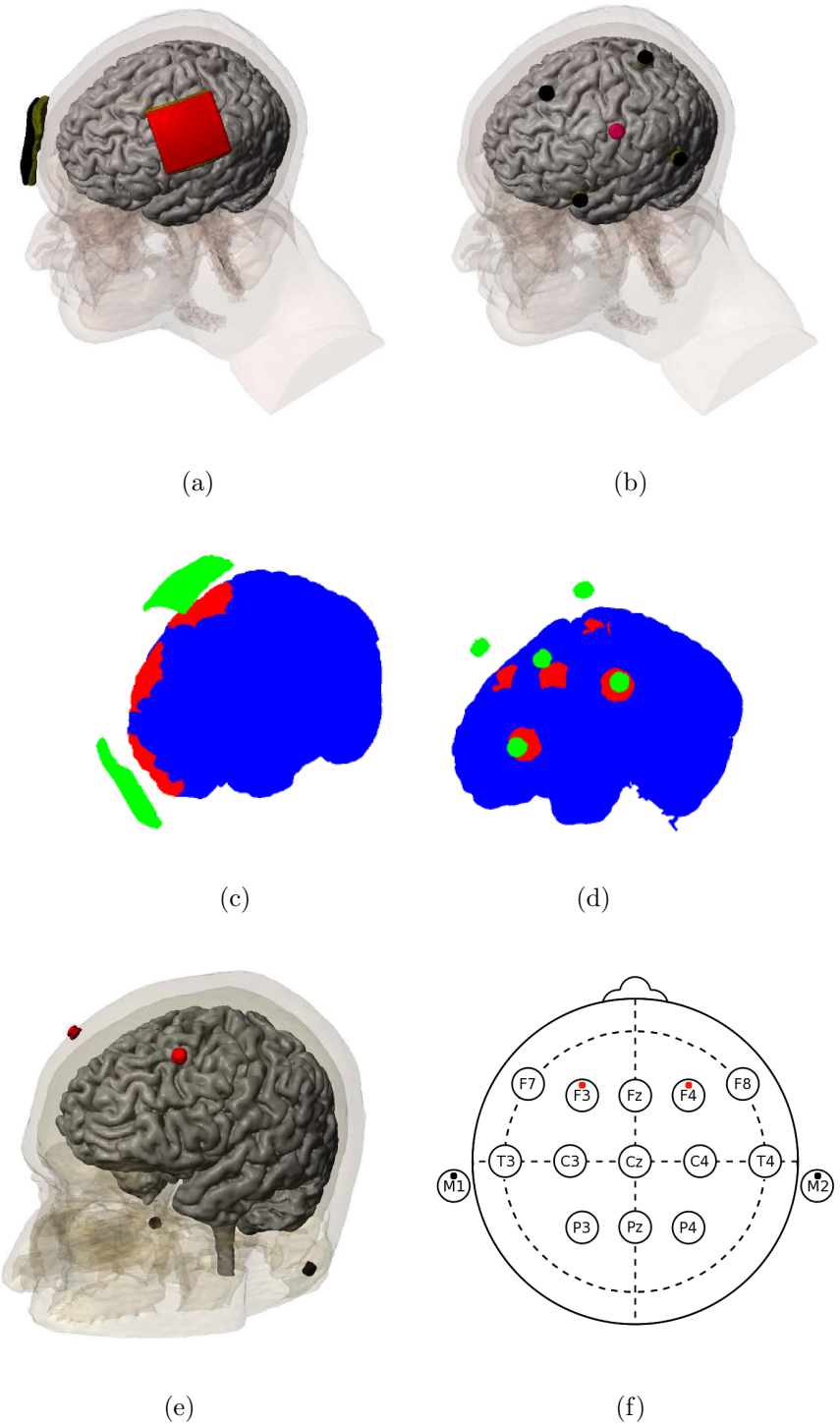

Figure 5.6: FEM human head models for analysis of the direction of the induced electric field. (a) Conventional tDCS pads, (b) 4-by-1 configuration, (c) regions of interest (red, 50 mm diameter) at the cortex in conventional tDCS: under electrodes and interelectrode space, (d) regions of interest in 4-by-1 montage (red, 15 mm diameter) under electrodes, (e) realistic FEM model for sleep experiments (red: anodes, black: cathodes) and (f) regions of interest in 10/20 EEG for analyzing directionality of normal component (F3, F4: anodes, M1, M2: cathodes).

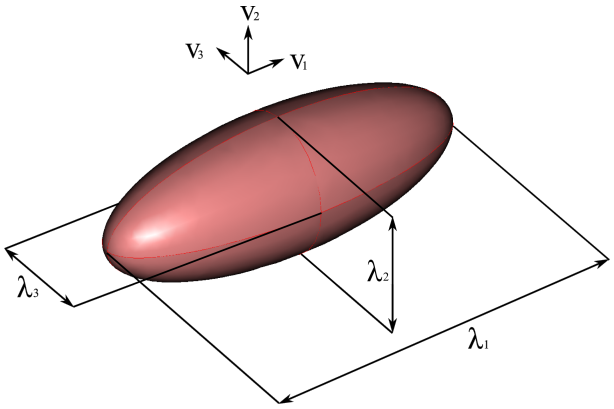

Figure 5.7: Ellipsoid representing a rank-2 tensor. Eigenvectors (v_1, v_2, v_3) determine the orientation of the axes and the eigenvalues $(\lambda_1, \lambda_2, \lambda_3)$ determine the length of the axes.

5.3.4 Anisotropic conductivity

Relation between diffusion and conductivity

So far, we have assumed isotropic conductivity of tissue. In the head however, it is known that there are two tissues showing high anisotropy, i.e. the skull and the white matter. The skull is composed of two layers of cortical bone tissue enclosing the diploe, a spongy and porous layer containing marrow and blood which shows a higher conductivity. For this reason the skull is represented with a conductivity ratio radial to tangential (to the skull surface) of 1:10 [142]. This ratio has been used as the upper-bound when studying anisotropy in EEG studies [143]. An important characteristic of neuronal tissue in white matter is that its fibrillar, consisting of aligned axons forming bundles. The diffusion of water molecules is therefore limited in the orthogonal direction to the axons, whilst favored along the parallel orientation to them. The conductivity ratio of normal to parallel conductivity in white matter fibers has been estimated to be up to 1:9 [144].

The diffusion of water molecules in the brain can be obtained through diffusion tensor imaging (DTI) by applying a series of diffusion gradients, that is, magnetic field variations increasing and decreasing the frequency of the exciting signal in different directions [145], [146], [147]. A minimum of six gradient-sensitizing directions is needed to solve the diffusion coefficients and obtain a rank-2 tensor, i.e. a 3x3 matrix that fully characterizes diffusion in 3D space and has the following form:

$$\mathbf{D} = \begin{pmatrix} D_{xx} & D_{xy} & D_{xz} \\ D_{yx} & D_{yy} & D_{yz} \\ D_{zx} & D_{zy} & D_{zz} \end{pmatrix}. \tag{5.3}$$

This means we can obtain a tensor for each voxel in the volume of our scan. Subsequently, the direction of maximal diffusion can be determined by calculating the eigenvectors and eigenvalues of each tensor. The eigenvectors are orthogonal to each other and describe the directions of diffusion, whereas the eigenvalues describe the strength of the anisotropy in the corresponding eigenvector direction. It is useful to illustrate the eigenvalues and eigenvectors as an ellipsoid (Fig. 5.7). If the eigenvalues are significantly different from each other, diffusion is said to be anisotropic and the ellipsoid shows an elongated shape. If the eigenvalues are similar the diffusion is isotropic and the ellipsoid takes the shape of a sphere [146].

The conductivity tensor of the brain can be estimated *in vivo* from DTI data. Tuch *et al.* [148],[149] showed how the conductivity tensor can be inferred from the water self-diffusion tensor given the strong linear relationship between the two. A statistical analysis of the microstructure was used to derive the cross-property relation in terms of the intra and extra-cellular space transport coefficients, which yields the diffusion tensor and the conductivity tensor to share eigenvectors.

Approaches to obtain the conductivity tensor

- **Direct mapping**

  This is the approach proposed by Tuch *et al.* [148], in which a linear relationship is established between the eigenvalues of the diffusion and conductivity tensors, namely

  $$\sigma_v = s \cdot d_v, \text{ with } s = \frac{\sigma_e}{d_e}, \tag{5.4}$$

  where σ_v is the vth conductivity corresponding to the diffusion eigenvalue d_v, s corresponds to the scaling factor empirically set to $s = 0.736\ \frac{S \cdot sec}{mm^3}$ according to [148]. σ_e and d_e denote the extracellular conductivity and diffusivity respectively.

- **Direct mapping with volume constraint**

When using the direct mapping approach, the factor s from [148] often yields unrealistic high conductivity values. For this reason, the volume constrained approach [150], [151] makes sure that the factor s stays within a reasonable range such that the geometric mean of the conductivity eigenvalues, averaged across all voxels, fits the isotropic conductivity reported in the literature. The factor is then defined as

$$s_{VC} = \frac{d_{wm}\sigma_{wm}^{iso} + d_{gm}\sigma_{gm}^{iso}}{d_{wm}^2 + d_{gm}^2}, \tag{5.5}$$

where σ^{iso} is the isotropic conductivity value from the literature and $d_{wm/gm}$ is the geometric mean of the white mater or gray matter compartment, obtained as follows

$$d_{wm/gm} = \sqrt[3]{\frac{\sum_{i=1}^{N_{voxels}} \prod_{j=1}^{3} d_i^j}{N_{voxels}}}. \tag{5.6}$$

N_{voxels} denotes the number of voxels in the corresponding compartment and d_i^j is the jth eigenvalue of the diffusion tensor in the ith voxel. The factor s_{VC} is then used for both compartments, gray and white matter.

- **Volume normalized**

Another approach proposed by Güllmar *et al.* [152] is to match the geometric mean of each conductivity eigenvalue voxel to an isotropic reference value. In other words, it matches the volume of the ellipsoid defined by the conductivity tensor (Fig. 5.7) to the volume of the isotropic conductivity sphere while leaving the orientation of the eigenvectors unchanged, providing an more conservative approach than the volume constraint. The normalized conductivity eigenvalues σ_i are obtained by

$$\sigma_i = d_i \cdot \frac{\sigma_{wm/gm}^{iso}}{\sqrt[3]{\prod_{j=1}^{3} d_i^j}}. \tag{5.7}$$

From DTI data to anisotropic mesh

In order to solve an anisotropic FEM model, there are a set of processing steps needed to extract the relevant information from the DTI data. We can divide the workflow in three stages explained below. Fig. 5.8 summarizes the workflow for obtaining the diffusion tensors, apply the conductivity mapping and integration to the FEM model.

1. **Pre-processing**

   It is the extraction of eigenvalues and eigenvectors from the DTI volumes. There are a number of software packages to perform the so-called pre-processing which include MedINRIA [153], DTIStudio [154], FSL [155] among others. We chose FSL since it has become an established tool in neuroscience, it allows easy manipulation of the data and also allows to automate the procedures through *shell* scripts.

   In this stage we have to correct for movement artifacts of the subject during the scan. This is achieved performing an eddy current correction. The next step is to obtain the eigenvalues and eigenvectors of the diffusion tensors (FSL DTIfit), followed by an affine registration of the fractional anisotropy [145] volume from the DTI scan to the T1 anatomical data (FSL FLIRT). The resulting transformation matrix was subsequently used to register the eigenvectors making sure their diffusion directions were preserved (FSL VECREG). Finally, an affine registration of the eigenvalue volumes was performed (FSL FLIRT).

2. **Conductivity tensor construction**

   Once we have the eigenvalues and eigenvectors, its necessary to adopt one of the conductivity mapping schemes (mentioned in the past section) and construct the conductivity tensor in such way. Given that we have eigenvalues and eigenvectors matrices, we can obtain the corresponding tensor applying a singular value decomposition:

$$\sigma_{\mathbf{t}} = \mathbf{V}\mathbf{D}\mathbf{V}^{\mathbf{T}}, \tag{5.8}$$

where **V** is the 3x3 eigenvectors matrix and **D** is the 3x3 diagonal eigenvalue matrix. The resulting conductivity tensor matrix, just like the diffusion tensor, is a symmetric matrix, which means that we only need the upper triangular elements to describe the tensor. The conductivity tensor construction is performed using custom code in MATLAB (Mathworks, Natick, MA).

3. **Integration of conductivity tensor to FEM mesh**

In order to integrate the conductivity tensor to the mesh we need to assign a coordinate to each tensor element in the same coordinate system as the T1-data (because that is where the FEM model geometries are constructed from). We do this using the segmentation mask from the brain, only taking the relevant voxels from the data. Subsequently, we write six text files corresponding to each one of the elements of the upper triangular matrix of the conductivity tensor. These text files will be read by the FEM software COMSOL Multiphysics (COMSOL AB, Sweden). In COMSOL, one needs to define a linear interpolation function for each element of the tensor. This function takes the coordinates of the tensor and interpolates it to those of each mesh element in the geometry. In this way, each mesh element has a corresponding conductivity tensor.

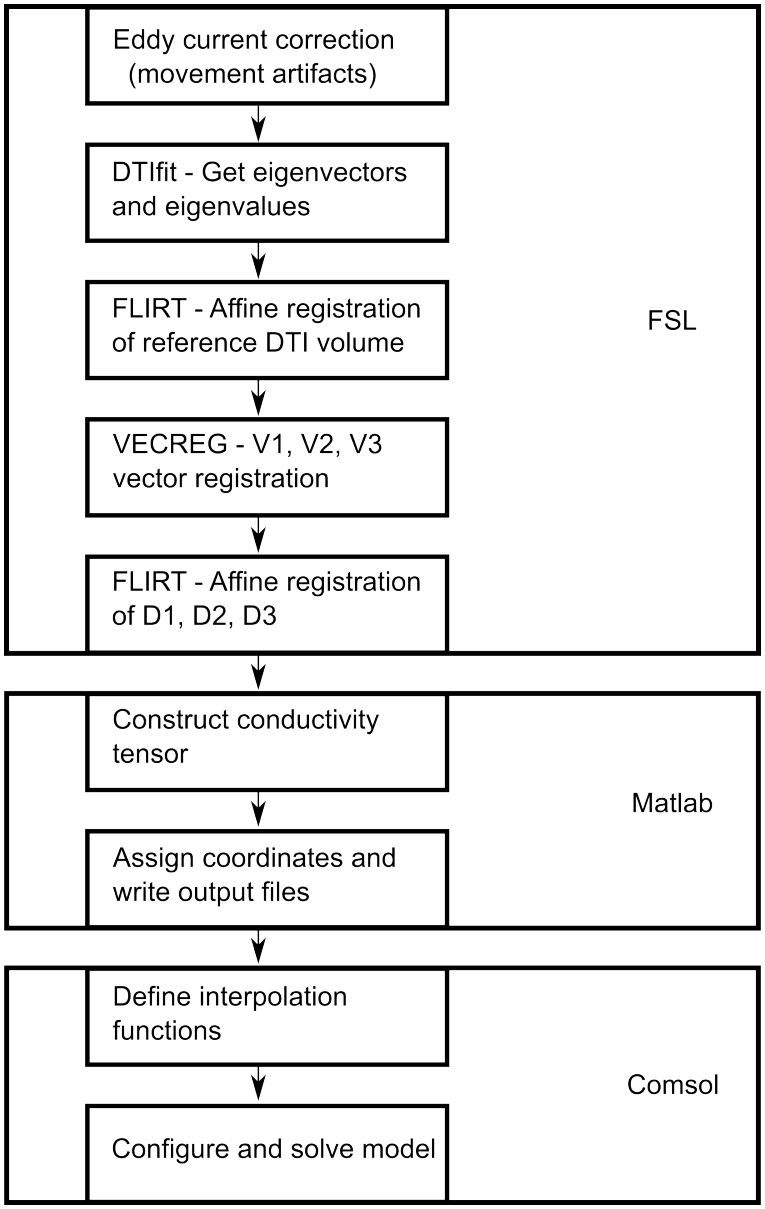

Figure 5.8: Workflow for integrating anisotropic conductivity to FEM model. Three stages are shown depicting the environment in which they take place, i.e. FSL, MATLAB and COMSOL. Eigenvector volumes are referred to as V1,V2,V3, whereas eigenvalue volumes are D1,D2,D3.

5.4 Animal studies

5.4.1 TMS animal study: neurotransmitter outflow in the rat

There is evidence that modulation of neuronal activity in nucleus accumbens shell region may re-establish normal function in various neuropsychiatric conditions such as drug-withdrawal, obsessive-compulsive disorder, depression and chronic pain,[5],[6], [124]. In this study we analyzed the effects of acute repetitive transcranial magnetic stimulation on monoamine outflow in the nucleus accumbens shell in awake and freely moving rats. We applied 20 Hz rTMS in 6 trains of 50 stimuli with 280 ms pulse-width at a magnetic field strength of 130% of the individual motor threshold. In order to quantify neurotransmitter outflow in the nucleus accumbens shell we used intracerebral microdialysis, before, during and after applying rTMS. All procedures with animals were reviewed and approved by the University of Lübeck and the Ministry for Agriculture, the Environment and Rural Areas, Schleswig-Holstein, Germany, and conducted in accordance with the NIH guide for the Care and Use of laboratory animals.

The monoamine transmitters dopamine and serotonin as well as their metabolites were measured using high performance liquid chromatography (HPLC) with electrochemical detection. Also, the amino acid neurotransmitter glutamate and gaminobutyric acid (GABA) and their common precursor glutamine were analyzed.

We performed an analysis of the TMS parameters for the experiment through finite element simulations with an accurate model of the anatomy of the rat scalp and brain presented in Section 5.2.3. We obtained the induced electric field distribution in the brain and the attenuation profile of the electric field magnitude with depth. This profile was calculated in the dorsal-ventral direction going through the nucleus accumbens shell region.

The simulations allowed us to quantify the effect of TMS in the rat brain and to have an estimate of the portion of the induced electric field which affected the nucleus accumbens. The simulations were pivotal for understanding the relation of the neurotransmitter outflow with stimulation in our hypothesis that the changes in monoamine transmitters most likely occur through interaction with cortical structures.

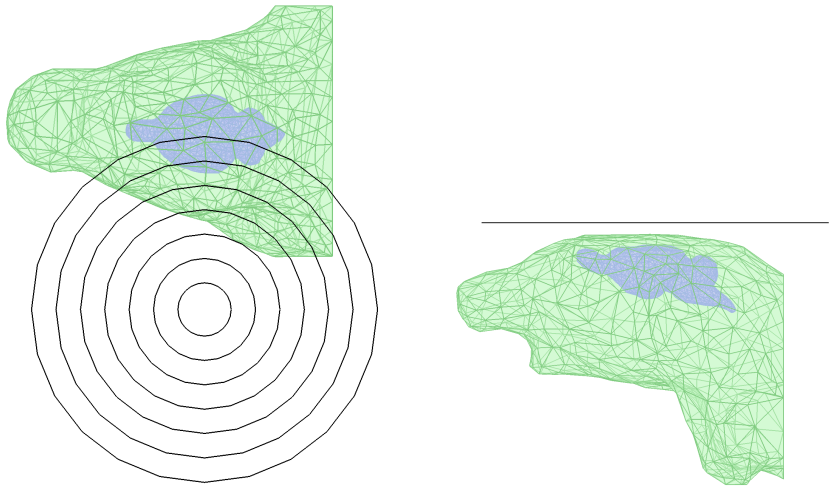

(a) (b)

Figure 5.9: Simulation setup for TMS animal study using circular coil Medtronic MagPro MCF75. (a) Top and (b) lateral view of the coil placed over the left hemisphere of the rat brain.

A realistic model of the Medtronic MagPro MCF75 circular coil was generated, accurate to its geometry and windings but projected into one layer, similarly to [132]. The coil was placed 3 mm above the left hemisphere of the rat's brain (Fig. 7.24). Taking into account that for the experiment, we used the stimulator 4T MagPro X100 with MagOption (MagVenture A/S, DK), the coil was energized with an input current of 2610 A, which corresponds to a maximum of 59 A/μs in the derivative of the biphasic waveform and 30% of the stimulator output, which is the stimulation intensity corresponding to 130% of the rat's motor threshold according to our observations using motor evoked potentials of the rat's leg [124].

5.4.2 tDCS animal study: memory consolidation in the rat

The fact that sleep promotes memory consolidation for several memory systems has been shown in numerous studies in humans and rodents [156],[157]. The application of tDCS, oscillating at the frequency of endogenous slow oscillations during slow wave sleep, enhanced memory consolidation for a hippocampus dependent task and therefore suggested a causal role of slow oscillations for sleep dependent memory consolidation in humans [46],[47].

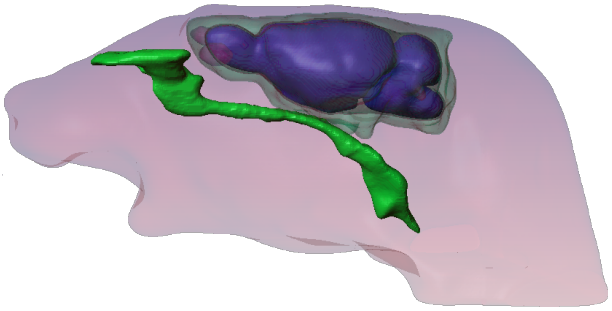

(a)

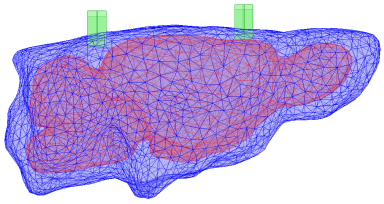

(b)

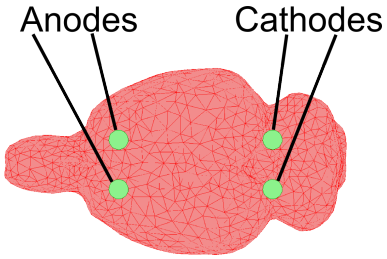

(c)

Figure 5.10: Improved realistic model of the rat used in animal study. (a) Complete model (lateral view) including skin, skull, CSF, brain, eyes and airways. (b) Lateral view depicting the electrodes (green) implanted halfway through the skull (blue). (c) Top view showing electrode positions: two anodes placed +2.5 mm antero-posterior, 2 mm symmetrically lateral, and two cathodes -10 mm anteroposterior, 2 mm symmetrically lateral.

In this study, we aimed at replicating and extend these findings to a rodent model. Slow oscillatory transcranial direct current stimulation was applied over the frontal cortex of rats during NonREM sleep and its effects on memory consolidation in the one-trial object-place recognition task were examined [125]. All the procedures with animals were reviewed and approved by the University of Lübeck and the Ministry for Agriculture, the Environment and Rural Areas, Schleswig-Holstein, Germany, and conducted in accordance with the European animal protection laws and policies (directive 86/609, 1986, European Community).

In order to know the induced electric field distribution in the rat as a result of tDCS, we employed the realistic model defined in Section 5.2.3. However, further improvements were included: segmentation masks of the skull, eyes, airways and CSF were integrated following the same procedure described in Section 5.3.1. The new model is depicted in Fig. 5.10.

Using this model and considering we required focal stimulation over the frontal cortex, we came to the following electrode configuration: two anodes placed +2.5 mm anteroposterior, each 2 mm symmetrically lateral, and two cathodes -10 mm anteroposterior also 2 mm symmetrically lateral. The electrodes were modeled as stainless steel cylinders with 1.57 mm diameter and 2.4 mm shaft length. They were implanted halfway through the skull, which is an achievable level of insertion in the surgery without damaging the brain through mechanical pressure. Other tDCS rat experiments have used much larger electrodes [117], [158]. However, reducing the size of the electrodes, like the ones used in this study, allows to improve focality. Similar small electrode configurations have been successfully used for neuronal entraining [135] at low field strengths.

We assigned the boundary conditions specified in Section 5.2.3, applying a current of 9 μA. Geometries were meshed and solved iteratively using the conjugate gradients linear system solver (relative tolerance of $1\text{x}10^{-6}$) with an algebraic multigrid preconditioner. The models were composed of ca. $5.7\text{x}10^{5}$ tetrahedral elements and $7.9\text{x}10^{5}$ degrees of freedom.

Chapter 6

Inverse problem[1]

This chapter presents the formulations for approaching the inverse problem in transcranial current stimulation, i.e. specifying an arbitrary magnitude and orientation of the induced electric field at a target and using optimization methods for finding the appropriate electrode currents needed to obtain such result. We describe several optimization approaches along with their particular attributes. We present three methods for the sparse representation of the desired electric field using a limited subset of the electrodes at our disposal, which has major practical implications. We introduce the experimental setup used to systematically validate our methods.

6.1 Introduction

In general, *inverse planning* involves defining the outcome one wishes to obtain and then the use of mathematical tools to calculate the optimal parameters which produce such result. Inverse planning is present in a number of medical applications, e.g. computed tomography, EEG and radiotherapy. In the context of radiotherapy treatment planning, for example, one defines the region of interest and their corresponding doses (e.g. high dose for a tumor and low dose for critical organs in the vicinity). After the clinician specifies the requirements, an optimization method calculates the beams, angles, intensities and other settings which can produce this result. Inverse planning is safer and more accurate than forward planning, which normally involves a cycle of trial and error.

[1]Parts of this chapter have been published in [159].

Routinely, in transcranial current stimulation there is no individualized planning, which explains the inter-individual variability that has been observed in a variety of studies [2]. The integration of forward planning alone into the clinicians' workflow would provide valuable information about the extent and magnitude of stimulation in the brain. Inverse planning can go one step further. It can yield the optimal parameters in order to standardize stimulation and maximize the effects while making sure that the applied currents are safe for the patients.

For approaching the inverse problem in transcranial current stimulation we require three components: (1) an anatomically accurate geometry model of the head where to run our calculations, using a method for determining the induced currents in the brain (in our case FEM), (2) a physical model of current conduction in the human head and (3) an optimization method which applies the physical model and sets additional requirements (such as safety) in order to produce the desired result. The first component has been exposed in the former chapter along with its forward solution, the second and third components will be explained in detail in the subsequent sections of this chapter.

6.2 Linear superposition of the electric field

As a physical model of conduction, we employ the linear superposition of applied currents in the human head. A comprehensive formulation has been expressed in [12], which is adopted in this work. Considering the multi-electrode stimulation paradigm and respective FEM model, the brain model is composed of u_n $(n = 1, ..., N)$ finite elements. Also $m = 1, ..., M$ electrodes are considered. In the EEG 10/10 configuration, for example, $M = 63$, in addition to the reference electrode Iz (localized at the inion).

To obtain the contribution of each electrode to the total electric field, we compute the resulting electric field from stimulating only one electrode at the time with a normal current density of $s = 1$ A/cm^2. Repeating this last step for M electrodes, gives us the lead field a_m for each electrode at all finite element nodes; which allows us to express the electric field vector $e_m \in \mathbb{R}^3$ at each finite element, for each electrode m, namely:

$$\mathrm{e_m(u_n) = s_m a_m(u_n).} \tag{6.1}$$

Now stimulating with all electrodes simultaneously, the total electric field at location

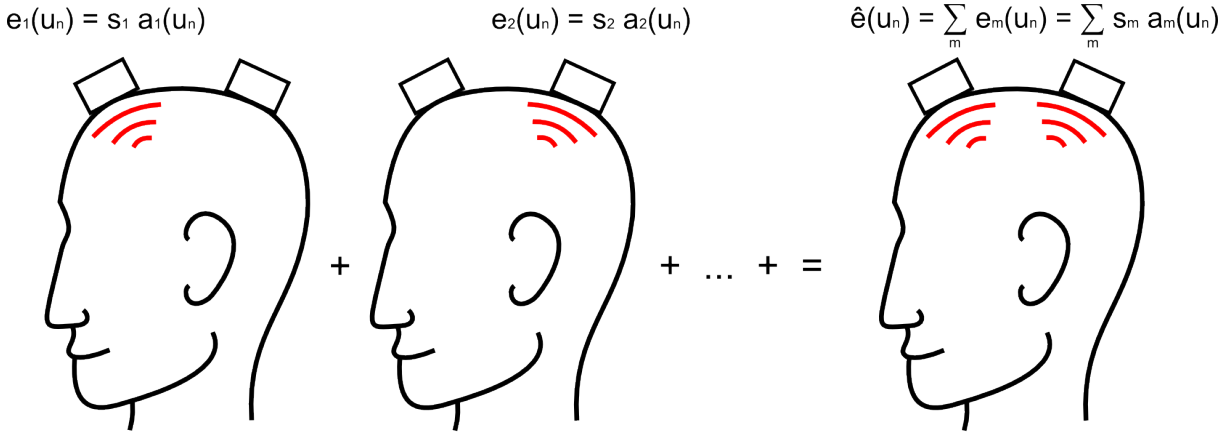

Figure 6.1: Superposition principle applied to transcranial current stimulation. The total induced electric field in the brain $\hat{e}(u_n)$ is equal to the sum of electric field responses e_m for each source s_m applied individually. $a(u_n)$ is the resistivity function which describes the resistance of the brain in each discretized element u_n.

u_n is given by:

$$\hat{e}(u_n) = \sum_{m=1}^{M} s_m a_m(u_n), \tag{6.2}$$

or in matrix notation $\mathbf{e} = \mathbf{sA}$. Where $\mathbf{A}$ is the lead fields matrix with dimensions N-by-M, s is a vector with M elements, and e is a vector with N elements. The corresponding matrices are then as follows:

$$\mathbf{A_{n,m}} = \begin{pmatrix} a_1(u_1) & a_2(u_1) & \cdots & a_M(u_1) \\ a_1(u_2) & a_2(u_2) & \cdots & a_M(u_2) \\ \vdots & \vdots & \ddots & \vdots \\ a_1(u_N) & a_2(u_N) & \cdots & a_M(u_N) \end{pmatrix}, \mathbf{s_m} = \begin{pmatrix} s_1 \\ s_2 \\ \vdots \\ s_M \end{pmatrix}, \mathbf{e_n} = \begin{pmatrix} e(u_1) \\ e(u_2) \\ \vdots \\ e(u_N) \end{pmatrix}. \tag{6.3}$$

Thus, the linear superposition of the fields from each electrode gives the resulting electric field at each finite element node in the brain. We consider the electrode current densities $\mathbf{s_m}$ to be scalar quantities, i.e., assuming their direction is normal to the electrode's surface.

With this formulation, we can apply optimization techniques to calculate the current densities $\mathbf{s_m}$ to generate previously specified intensity and orientation of the electric field. We illustrate these formulations in Fig. 6.1.

Since the electric field in the brain is three-dimensional, the Equation 6.2 has to be obtained for each x, y and z component. If we do so and reorganize the matrices in the expressions 6.3, this yields

$$\tilde{\mathbf{A}}_{\mathbf{n},\mathbf{m}} = \begin{pmatrix} \mathbf{A^x} \\ \mathbf{A^y} \\ \mathbf{A^z} \end{pmatrix}, \mathbf{s_m} = \begin{pmatrix} s_1 \\ s_2 \\ \vdots \\ s_M \end{pmatrix}, \tilde{\mathbf{e}}_\mathbf{n} = \begin{pmatrix} \mathbf{e^x} \\ \mathbf{e^y} \\ \mathbf{e^z} \end{pmatrix}. \tag{6.4}$$

The formulations we just presented are used by the optimization schemes described in the following sections of this chapter. The diagram in Fig. 6.2 summarizes the workflow for multi-electrode optimized tDCS consisting of three steps: (1) selction of multi-electrode paradigm, (2) definition of desired outcome (target location, field magnitude and orientation) and (3) optimization of applied currents.

6.2.1 Using electrode currents instead of voltages

The superposition of electric fields holds equally for applying either transcranial currents or voltages. The optimization of electric potentials for stimulation has also been proposed in the literature [160]. However, having both alternatives, there is one strong reason for formulating our model in terms of currents: in the superposition of current sources, those that are not active, i.e. have zero current, are regarded as open circuits, whereas superposing voltages implies that all sources that are not active have to be grounded. This reason has two important practical implications:

1. When applying voltages as stimulation sources, one has to take into account that the contact resistance between the electrode and the skin will always have an electric potential drop, which requires additional adjustments to ensure that the voltage on the scalp is correct. Conversely, when applying currents, the stimulator device delivers the requested current regardless of the contact resistance.

2. On the one hand, the fact that the inactive electrodes have to be grounded means that all electrodes need to be connected at all times to fulfill their role in the optimization. On the other hand, current control allows to connect just those electrodes which are active, namely $|s_m| > 0$. This simplifies the setup substantially and reduces the sources of human error.

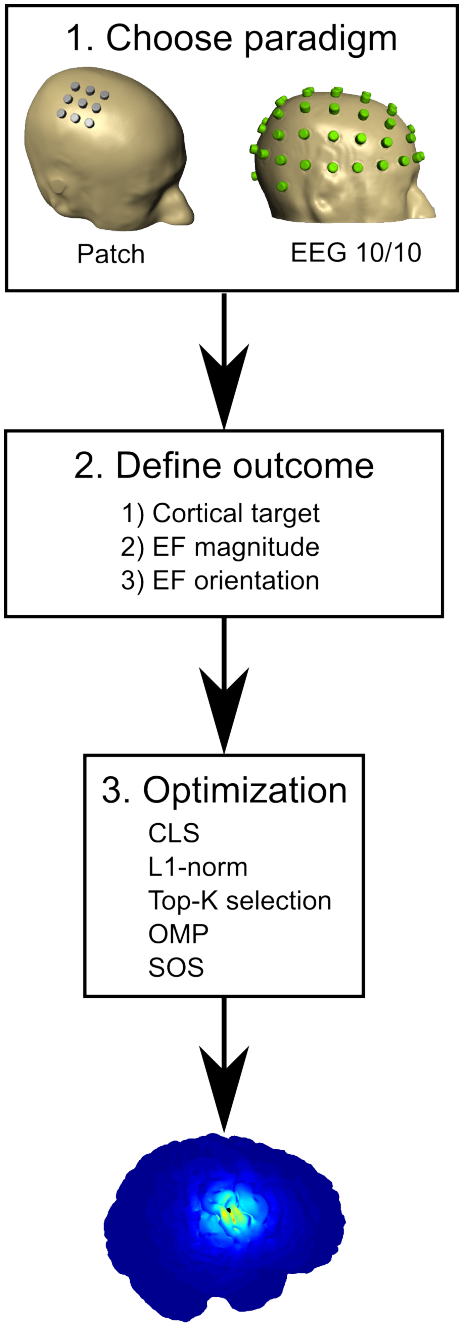

Figure 6.2: Multi-electrode optimized transcranial current stimulation: an approach for solving the inverse problem. The three-step workflow involves (1) selecting multi-electrode paradigm, (2) defining desired outcome of stimulation and (3) applying optimization scheme for obtaining the appropriate electrode currents.

6.2.2 Scalar versus vector fields: deep targets

One relevant point to address in the context of electric field shaping through optimization is whether it is possible to target deep structures in the brain. As we have addressed in the introduction of this work (Section 3.2.3), targeting deeper structures will always lead to maxima at the surface, at the boundaries where the conductivity changes. This problem has been studied by Heller *et al.* [67], where the authors prove that it is not possible to produce a local maximum of electric field strength inside the brain using any superposition of external current sources.

The nature of electrical stimulation of deeper structures is different in contrast to other methods where inverse planning is also put to use. For example, in radiosurgery a number of beams from different directions and doses are able to superpose deep inside different locations of the human body (brain included) and radiate regions of interest where tumors are located, while sparing other neighboring structures [161],[162].

Although both examples make use of the superposition principle to optimize their input parameters, the fundamental difference between radiosurgery and electrical stimulation is that the resulting dose from radiation is a *scalar field*, whereas the resulting electric field is a *vector field*. Formally, we can express it as follows. In a general sense let

$$\{F_n\}_{n=1,\ldots,N} = x_1 + x_2, + \ldots + x_n, \tag{6.5}$$

be a series representing a field distribution composed of the sum of N sources. If

$$F_n \in \mathbb{R}^i \text{ with } i = 1, \text{ then,} \tag{6.6}$$

$$F_n \leq F_{n+1}. \tag{6.7}$$

This means that for a scalar field ($i = 1$) the series F_n will increase monotonically as the number of sources increases. However

$$\forall\ F_n \in \mathbb{R}^i \text{ with } i > 1, \text{ the statement 6.7 does not hold.} \tag{6.8}$$

Which implies that when the field is of higher dimensions ($i > 1$), it does not necessarily increase monotonically as the number of sources increases, i.e. it has a vectorial nature, where different sources can add but as well subtract (cancel) each other.

To illustrate this point let us now imagine a sphere where we have two sources

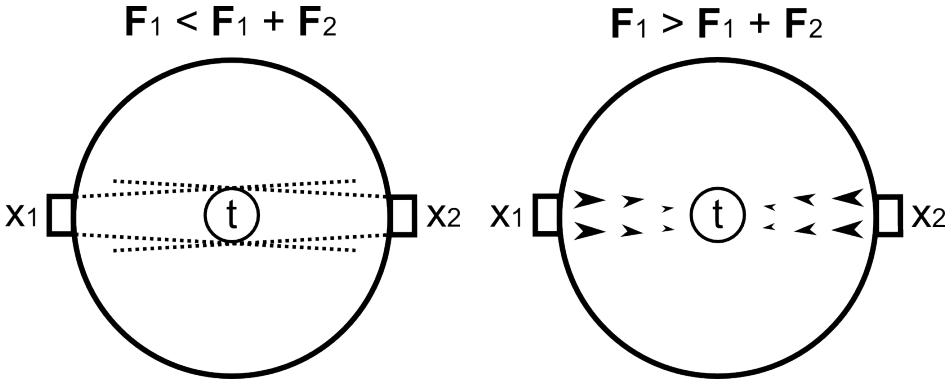

(a) (b)

Figure 6.3: Example of a scalar versus vectorial field with two sources in a sphere. F_n is the contribution of the source x_n (assuming $x_n > 0$) at the region of interest t. (a) Scalar field from two sources: its additive nature is independent from the direction of the sources. The total contribution of the sources x_1 and x_2 is greater than any of them alone. (b) Vector field from two sources. The total contribution of the sources is less than the individual ones given that they have opposite directions.

placed symmetrically on the outer surface as depicted in Fig. 6.3. If we energize both sources simultaneously and observe the field at a region of interest, we note the following: the scalar field on the one hand will show that the resulting magnitude at the region of interest is additive and increases its absolute value (compared to just having one source active). On the other hand, the resulting vector field will also be equivalent to the addition of the contribution of both sources. However, given that the field direction for the sources is opposite, they subtract each other at the region of interest.

Another point to consider when comparing electric current to a radiation beam is that in electric stimulation the Laplace equation dictates that the current going inside the medium has to come out. The profile in depth when stimulating electrically is well-know to decay exponentially whereas in the case of a beam, it goes through with a given attenuation profile (which needs to be taken into account in the optimization).

We have explained why it is physically not possible to reach focality inside a medium when the superposition of sources yields a vectorial field. This is the reason why the optimization schemes exposed in the previous sections of this chapter are aimed at cortical structures of the brain. Other techniques such as deep brain stimulation (DBS) have proven useful for dealing with disorders in the basal ganglia and other deep structures [163]. However, the invasiveness of this technique is a major issue

implying high costs and risk for the patient.

One possible alternative to reach deep structures in the brain with transcranial current stimulation is to exploit the higher conductivity of the cerebrospinal fluid. Particularly, at the inter-hemisphere space in the occipital lobe, the cerebrospinal fluid reaches the thalamus and midbrain. One can achieve a hotspot in such deep regions due to the so-called clustering effect, occurring at the boundary where conductivity changes (between cerebrospinal fluid and other brain tissue). Unfortunately, like we have explained in this section, one cannot avoid having other hotspots at the surface or the brain, directly under the active electrodes.

6.3 Optimization

6.3.1 Constrained least squares (CLS)

Least squares optimization poses the problem of minimizing the convex quadratic function expressed as

$$\|\mathbf{As} - \mathbf{e_d}\|_\mathbf{2}^\mathbf{2} = \mathbf{s^T A^T As} - \mathbf{2e_d^T As} + \mathbf{e_d^T e_d}, \tag{6.9}$$

to which a unique analytic solution is given by $\mathbf{s} = \mathbf{A}^\dagger\mathbf{e_d}$, satisfying the so-called normal equations (with $\mathbf{A}^\dagger$ being the Moore-Penrose pseudoinverse). However, for the application presented in this work, there must be a sensible safety criterion to ensure that the selected current densities are not harmful when stimulating, i.e., they do not exceed a maximum applied current I_{max}= 2 mA; a limit of comfort reported in the literature and used in tDCS studies [2], [119].

The maximum current density is then defined as $s_{max} = I_{max}/D_e$, where D_e is the surface area of the electrode in contact with the scalp. To accomplish this restriction, we constrain the least squares solution so that each electrode $\mathbf{s_m}$ does not take values beyond s_{max}. The problem can take the form of a quadratic program

$$\mathbf{s_{qp}} = \arg\min_{\mathbf{s}} \frac{\mathbf{1}}{\mathbf{2}}\mathbf{sHs^T} + \mathbf{f^T s}, \tag{6.10}$$

subject to $|s_m| \leq s_{max}$, $\forall\ m$, and $|\sum_{m=1}^{M} s_m| \leq s_{max}$,

where $\mathbf{H} = \mathbf{A^T A}$, $\mathbf{f^T} = -\mathbf{e_d A^T}$, and $|\sum_{m=1}^{M} s_m|$ is the current that flows through the reference electrode. The optimization adjusts the electrodes' current densities allowing them to act as anodes or cathodes in order to shape the electric field as close as possible (in the least squares sense) to the desired electric field. The target region is defined as:

$$\mathbf{e_d}(u_n) = \begin{cases} e_t, & n \in \mathcal{C} \\ 0, & n \in \mathcal{C}^c \end{cases}, \text{ with } \mathbf{e_d} \in \mathbb{R}^3 \tag{6.11}$$

where $\mathcal{C}$ is the set of finite element nodes in the brain corresponding to the target, and $\mathcal{C}^c$ is the complement of $\mathcal{C}$. e_t defines the intensity and orientation of the electric field vector. The orientation is assigned projecting e_t onto a unit vector in the desired electric field direction.

6.3.2 l_1-norm optimization

The least squares method with penalization of the l_1-norm produces both an accurate and most importantly, a sparse solution. This is desirable when performing optimization in multi-electrode stimulation because it favors obtaining solutions in which only a reduced subset of electrodes will be active, which has an immediate implication in hardware complexity.

Choosing to constrain the l_1-norm fulfills an even more conservative safety criterion, where less current flows through the brain in contrast to constraining each electrode's current density (as done in Equation 6.10). The l_1-norm constrained problem is expressed as

$$\mathbf{s_{l_1-norm}} = \arg\min_{\mathbf{s}} \|\mathbf{As} - \mathbf{e_d}\|_\mathbf{2}^\mathbf{2} + \lambda\|\mathbf{s}\|_\mathbf{1}, \tag{6.12}$$

where λ is the regularization parameter, which can be adjusted to set a compromise between sparsity and model accuracy (only taking non-negative values). The l_1-norm regularization was proposed as the least absolute shrinkage and selection operator (lasso) algorithm [164], commonly used in linear regression.

If we wish to adapt this regularization to multi-electrode tDCS, we cannot consider Equation 6.12, since that would neglect the remaining current flowing through the reference electrode. Therefore, we formulate the problem taking the current sources,

sinks and reference into account [12]:

$$\mathbf{s_{l_1-norm}} = \arg\min_{\mathbf{s}} \|\mathbf{As} - \mathbf{e_d}\|_\mathbf{2}^\mathbf{2} \tag{6.13}$$

subject to $\sum_{m=1}^{M} |s_m| + |\sum_{m=1}^{M} s_m| \leq 2s_{max}$.

The l_1-norm ($\sum_{m=1}^{M} |s_m|$) is the sum of absolutes and accounts for the positive and negative currents flowing in and out of the brain, whereas $|\sum_{m=1}^{M} s_m|$ is the remaining current flowing through the reference. The constraint is thus set to $2s_{max}$. Electric field intensity and orientation are defined as expressed in Equation 6.11.

6.4 Constraining the number of electrodes: subset selection

The l_1-norm optimization succeeds in reducing the number of active electrodes in the solution. However, the number of active electrodes may change according to the site of stimulation and field orientation. Moreover, the l_1-norm method does not allow to specify a maximum number of active electrodes, which would be necessary when the hardware is limited to a certain number of channels.

This means that with the previously exposed formulations, we cannot assure that multi-electrode tDCS is applicable in a realistic setup. Stimulators in the market have less than eight active channels [165], [166]. For this reason, we require to generate a sparse solution controlling the number of active electrodes. This idea arises having two additional relevant motivations: (1) Reduce hardware. This translates into maintaining a reduced size in multi-channel stimulators, which has a direct implication in costs, and (2) simplify the technique's workflow in practice. Having less electrodes means faster setup times and less sources of error.

One intuitive way to approach this problem would be to truncate the optimized solution taking the most significant electrodes. However, when doing this the induced electric field can change dramatically, given that the contribution of other less-significant electrodes can affect the solution substantially. In order to optimize a set of electrodes we need to solve the optimization problems described in Equations

6.10 and 6.13 including an additional constraint on the number of active electrodes, namely:

$$\|s_m\|_0 \leq k, \tag{6.14}$$

where k is the desired number of active electrodes, and $\|\cdot\|_0$ is a l_0 pseudo-norm which denotes the cardinality of the non-zero elements in vector $\mathbf{s}$. In the following subsections we will present methods for fulfilling this constraint.

6.4.1 Top-k selection

This approach for controlling the number of active electrodes involves two optimization steps. We propose the use the l_1-norm optimization as an *intermediate step* to perform the subset selection given its sparse properties. Subsequently, we find the k electrodes with the highest contribution to the vector $\mathbf{s_{l_1-norm}}$, that is, now having ranking electrode index i we determine the sequence $i_0, i_1, \ldots, i_k$ such that

$$|\mathbf{s_{i_0}}| > |\mathbf{s_{i_1}}| >, \ldots, > |\mathbf{s_{i_k}}|. \tag{6.15}$$

Once we have the subset of k electrodes, only these undergo an additional optimization step. This allows to restrict the solution to any desired number of electrodes. The second optimization step follows the scheme constraining each electrode individually (CLS) in order to provide more freedom to the solution, i.e. allowing s_m to take a wider range of values.

Given that the size of the l_1-norm subset varies according to the stimulation scenario, it is likely that as the desired number of active electrodes k approaches zero, the subset selection will ignore electrodes that may still be relevant, which shall limit the performance of the subsequent optimization. This is the compromise for reducing the allowable active electrode number (i.e. reducing the degrees of freedom) and therefore simplifying the hardware requirements. Nevertheless, by using CLS in the second step we ensure the flexibility in the optimization of the available number of active electrodes. We analyze the trade-off between active electrodes and the capacity to deliver a desired field magnitude and orientation. We evaluate the realistic scenarios having only four, six and eight channels at our disposal.

6.4.2 Electrode patch array

As an alternative to the subset selection, we propose the use of an electrode patch array (Fig. 6.2, top) composed of n electrodes positioned at the site of stimulation. The patch array provides an advantage against the EEG 10/10 configuration when stimulating radially (with electric field oriented normal to the surface of the brain) at any given target in the brain.

The solution from the optimization using the EEG 10/10 configuration will be sub-optimal if the target is not located directly under one of the predefined electrode positions. On the other hand, since the patch array has the freedom to be placed anywhere at the surface of the head, it can provide a solution closer to optimal in terms of field orientation and focality.

Another characteristic of the patch array is its reduced number of electrodes, which eliminates the need of performing subset selection when having hardware limitations. This also translates to shorter computation time for the optimization and FEM simulations.

In this work we evaluate the electrode patch array in four modalities: (a) 4-by-1 patch (four active electrode and reference in center) and (b) 3x3 patch array (eight active electrode and reference in center). Each one is implemented in two sizes: the spatial distribution of EEG 10/10, and a smaller version conserving the anterior/posterior left/right symmetries with increments of 5%, which we call 5/5 throughout this work.

All patch configurations employ CLS optimization in order to grant the solution more freedom by constraining electrodes individually, and to extend the attainable electric field at the target (in contrast to the l_1-norm method, which is more conservative), given the reduced number of channels.

6.4.3 Orthogonal matching pursuit

Considering a signal which can be decomposed of as a set of linear elements, the orthogonal matching pursuit (OMP) is a greedy algorithm which seeks a subset of elements that best represents such signal. It was introduced in the signal processing literature by Mallat *et al.* [167] based on its predecessor: the matching pursuit (MP). MP is a method for computing adaptive signal representations which are

sparse, iteratively choosing the element which can best represent the signal. The criterion is based on the inner product α of the residual $\mathbf{r}$ with the contribution of each of the elements (columns in $\mathbf{A}$, i.e. electrodes):

$$\alpha = | < \mathbf{A}^T, \mathbf{r} > |, \tag{6.16}$$

where $< \cdot >$ denotes the inner product. Subsequently we find the element (with index i_{max}) which reflects the highest correlation with the residual showing the maximum inner product, namely, the element with the minimum distance to the signal we wish to represent

$$i_{max} = \arg \max_{\alpha, i \notin D} (\alpha_i), \tag{6.17}$$

where D is the *winning-elements set*, containing the winning element throughout the iterations in the algorithm until a certain stopping criterion is met, e.g. when the norm of the residual is below a given threshold or when the algorithm has selected a previously defined number of elements. In the context of transcranial stimulation, we employ the latter one in order to select the most representative electrodes to the solution.

The MP selection criterion subtracts the orthogonal projection of the selected element onto the residual, i.e. it removes the selected column vector from the residual at each iteration

$$r_k = r_{k-1} - | < \mathbf{a_{MP}}, \mathbf{r_{k-1}} > | r_{k-1}. \tag{6.18}$$

It has been proven that MP displays asymptotical convergence as the number of chosen elements increases. However, it is known that MP does not provide the best possible representation [167]. The main problematic with MP is that the residual vector in the iterative process does not necessarily remain orthogonal to selected elements, which means that an element can be selected twice throughout the process.

To overcome this limitation, OMP was introduced to improve MP by providing a set of coefficients from which the linear expansion can minimize the distance to the signal. OMP makes sure that the residual remains orthogonal to the selected elements, therefore the algorithm doesn't allow to select an element twice. OMP accomplishes this feature using either: (1) an optimization step in each iteration or (2) a Gram-Schimdt-like orthogonalisation of all non-selected elements. In this way, we can obtain a new signal estimate and update the residual $\mathbf{r_k}$ only taking into account the selected elements.

In the context of multi-electrode tDCS the optimization step corresponds to the ap-

plying the CLS scheme, with individually constrained electrode currents (expression 6.10). The signal corresponds to the induced electric field in the brain resulting from the superposition of different active electrodes (Section 6.2), which are the aforementioned elements. OMP follows the selection criterion with $\mathbf{A}$ being the mixing matrix defined in Section 6.2. The OMP algorithm is written in Appendix A in detail.

6.4.4 Stepwise optimal selection

Whilst OMP allows to select the elements which show the best correlation with the residual vector, this criterion does not ensure that the model selection will be optimal in terms of the approximation's residual. This shortcoming stems from the inherited MP selection criterion only taking into consideration, the projections of the elements onto the residual.

The stepwise optimal selection (SOS) aims at improving this limitation by changing the selection criterion to one based on minimizing the residual. This idea is similar to that proposed by Rebollo *et al.* [168] in their optimized orthogonal matching pursuit (OOMP). However, there is a fundamental difference between the two: OOMP on the one hand makes use of the orthogonalisation of the contribution of the selected element onto the residual in each step of the algorithm (Equation 6.18) while minimizing the norm of the residual $\|\mathbf{r_n}\|$ [168]. SOS on the other hand performs $M - |C|$ optimizations on each step over all elements which have not been selected so far (M is the total number of elements and $|C|$ is the number of already selected ones). The optimization is done using the CLS scheme (Equation 6.10) constraining electrode currents individually. Importantly, SOS does not orthogonalise the projection of the selected elements onto the residual.

The main advantage of not orthogonalising is to avoid discarding the overlap in the contribution of different elements, which can yield to the erroneous selection of elements. This happens when two (or more) elements have a coinciding contribution to the solution. On each iteration, SOS obtains the resulting residual when adding each element to the selection individually. The algorithm does this by calculating:

$$\hat{\mathbf{r}} = \sum_{n=1}^{N} \left(\mathbf{e_d}(\mathrm{u_n}) - \mathbf{As}\right)^2, \tag{6.19}$$

for each remaining element. Where $\hat{\mathbf{r}}$ is the residual sum of squares from the N nodes

conforming the brain geometry. For each iteration $\hat{\mathbf{r}}_j$ we then solve the minimization problem

$$j_{min} = \arg\min_{\hat{r}}(\hat{\mathbf{r}}_j), \tag{6.20}$$

and subsequently add the winning element to the selection. A natural implication of the SOS is that solving $M-|C|$ optimizations yields a heavier computational cost than the previously defined schemes. The procedure is described in Appendix A in detail.

6.5 Performance evaluation

6.5.1 Measures

We evaluated the optimization schemes using the following measures:

- **Focality**. For comparison purpose, we use the focality measure introduced in [12], i.e., the half-max-radius (HMR), arising from:

$$\mathcal{F}(r) = \frac{\sum_{n\in\mathcal{T}(r)} \|e(u_n)\|}{\sum_n \|e(u_n)\|}, \tag{6.21}$$

  where the set $\mathcal{T}$ is a sphere centered at the target in the brain, containing all nodes within radius r. The HMR corresponds to the radius containing half of the total electric field, namely $\mathcal{F}(r) = 0.5$.

- **Misalignment**. The misalignment of the electric field is measured as the angle difference between the desired orientation at the target and that obtained after optimization, namely:

$$\theta_{mis} = |\theta_{desired} - \theta_{opt}|. \tag{6.22}$$

- **Total current flow (TCF)**. This measure allows us to rank the different schemes in their current consumption and therefore the required power the stimulator has to deliver. It also allows us to rank the safety of the schemes under the premise that less current flowing through the head is safer. We define the total current flow as:

$$TCF = D_e(\sum_{m=1}^{M} |s_m| + |\sum_{m=1}^{M} s_m|), \tag{6.23}$$

which accounts for the sum of the current densities going inside and outside the head through the active electrodes s_m (first term), plus the remaining current flowing through the reference electrode (second term). If we multiply both terms by D_e (surface area of the electrode), we obtain the applied current in Ampères.

- **Number of active electrodes**. This measure reflects how parsimonious is the solution provided by the evaluated schemes, which directly influences the complexity of the hardware for stimulation.

6.5.2 Evaluation

In order to asses the benefits of our methods, we present an evaluation on: (1) conventional rectangular pads placed over the primary motor cortex contralaterally; (2) CLS optimization (64 electrodes EEG 10/10); (3) l_1-norm constrained optimization (64 electrodes EEG 10/10); (4) Top-k optimization with k active electrodes from the EEG 10/10; (5) optimized 4-by-1 patch (using CLS); (6) optimized 3x3 electrode patch array (using CLS); (7) OMP with k active electrodes from the EEG 10/10, and (8) SOS with k active electrodes from the EEG 10/10.

To quantitatively evaluate the proposed schemes we show the focality and misalignment curves along the electric field intensity at the target for a radial field orientation. The target for all methods is located in the primary motor cortex, directly under C4 at the surface of the brain. The patch schemes are considered in both arrangements, i.e. 5/5 and 10/10 spacing. The subset selection methods were evaluated for four, six and eight active electrodes.

Focality and misalignment curves allow to characterize our methods. However, one should expect some variation when choosing different targets due to the irregular anatomy of the brain. For analyzing this effect we evaluated the performance of the optimization schemes in different target locations across the cortex with electric field intensity of 0.3 V/m in two field orientations, i.e., radial and tangential. We chose 22 targets in the brain with the following locations in the EEG 10/10 configuration: C1, C2, C3, C4, C5, C6, FC3, FC4, FC5, FC6, CP3, CP4, CP5, CP6, F3, AF3, F4, AF4, P3, PO3, P4, PO4. The patch schemes were evaluated in the 10/10 arrangement.

Topographic plots of the focality across the cortex using the 22 targets listed above were obtained for all schemes. These focality maps illustrate the performance of the

schemes in terms of the HMR and were obtained for radial and tangential targeting.

6.5.3 Computation

All methods were implemented in MATLAB (Mathworks, Natick, MA). For the calculation of the lead fields, MATLAB was interfaced to COMSOL to allow the automation of simulations as well as for the ease of the post-processing. All simulations ran on a PC with processor Intel Core i7 at 3.4 GHz with 16 Gb RAM.

6.6 Experiments: inverse planning *in vitro*

In the Section 4.1 of this work we described the setup for validating the forward problem of having stimulating sources in a conductive medium, comparing our measurements to the simulations. Those experiments set the basis for multi-electrode electric stimulation by proving the superposition of sources and the validity of the simulations. To elaborate on this idea experimentally, we used our optimization methods in order to calculate the appropriate currents for achieving a given magnitude and orientation of the electric field at a predefined target.

We performed experiments for two scenarios which are relevant for transcranial stimulation, namely, tangential and radial field orientation to the outer boundary. These scenarios are particularly important because experimental data in vitro has shown that cortical pyramidal cells (which are oriented normal to the cortical sheet) are preferentially polarized when the electric field is present either parallel or orthogonal to the soma's axis, i.e. radial or tangential to the surface of the brain [104].

The setup consists of the same integrating blocks defined for superposition principle experiments (Section 4.1, Fig. 4.1c). However, for this experiment we use a total of eight electrodes: seven active electrodes (able to operate as sources or sinks) and one reference. All electrodes are immersed orthogonal to the conductive solution surface, in a 10 cm diameter, 2 cm depth petri dish. For measuring we employed a tungsten needle electrode driven by the SASSU robot in a predefined grid of 4 cm $\times$ 4 cm measuring nodes in the conductive medium. The medium was saline solution with conductivity $\sigma = 9$ mS/m, verified with the conductivity meter PCE-PHD (PCE Instruments UK Ltd. UK). The experiment setup is shown in Fig. 6.4 along with the respective simulation geometries.

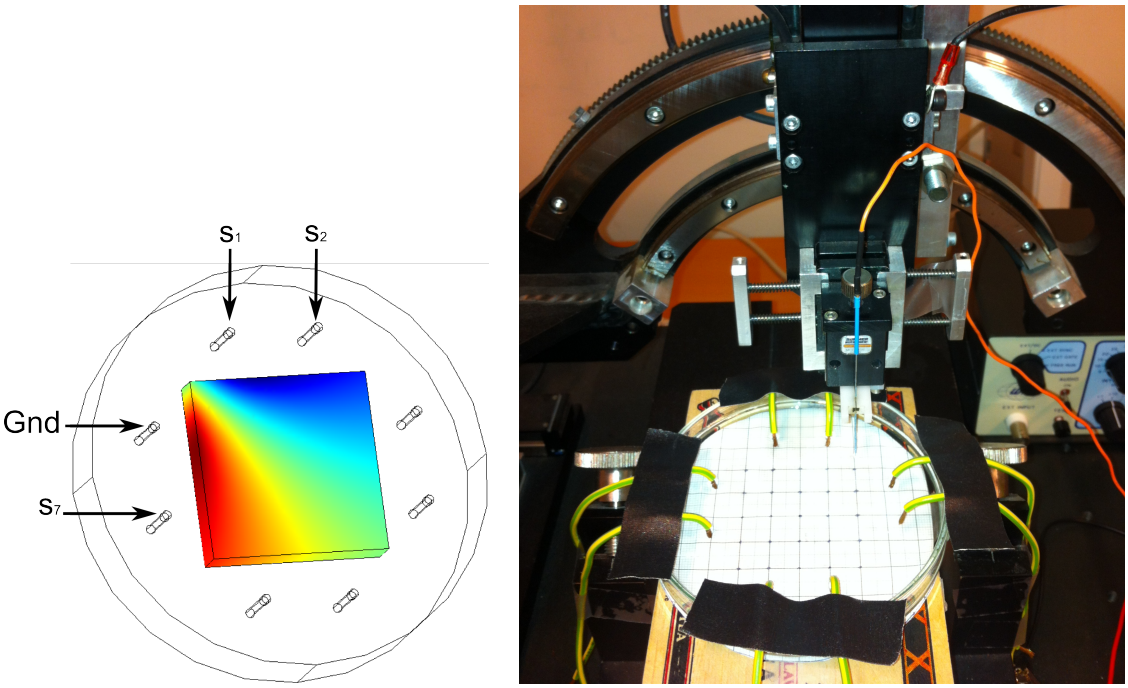

(a) (b)

Figure 6.4: Experiment setup: inverse planning of electrical stimulation in conductive medium. (a) Simulation geometries for experiment with electrodes numbered clockwise, (b) real scenario in laboratory. The SASSU robot drives the needle electrode in the conductive medium in synchrony with the acquisition of the g.USBamp (g.tec medical engineering GmbH, Schiedlberg, Austria). The current controlled stimulator Isostim (World Precision Instruments Inc. Sarasota, FL, USA) generates a periodic stimulating signal for the seven independent channels.

Chapter 7

Results[1]

In this chapter we present the results from the previously introduced developments in three parts: (1) TMS: findings from TMS coil modeling with conductive shield plate in a simplified rat model and experimental measurements of the conductive shield plate for two commercial coils; (2) tDCS: simulations of the realistic tDCS rat model, a comparative evaluation of the different optimization schemes for multi-electrode tDCS in the human, experimental results *in vitro* for the validation of inverse planning, an analysis of the direction of the induced electric field and the anisotropic conductivity analysis; (3) Animal studies: forward planning of TMS and tDCS studies with our realistic rat model.

7.1 TMS coil with conductive shield plate in simplified rat model

The simulation of the distribution of the induced electric field for TMS without shield plate is shown in Fig. 7.1a. The simulation for TMS with shield plate is depicted for the five evaluated circular window diameters, namely, 10 mm, 15 mm, 20 mm, 25 mm and 30 mm (Fig. 7.1b-f respectively).

From the electric field distributions depicted in Fig. 7.1 and observing the values presented in Table 7.1, it is noted that TMS with the conductive shield plate covers substantially smaller regions than stimulation without the shield plate.

[1]Parts of this chapter have been published in [122], [123], [124], [125], [108], [141] and [159].

Table 7.1 shows the focalization in terms of the HPR ratio of each window diameter, relative to the HPR ratio of the stimulation without shield plate, which is 0.1683. Table 7.1 also shows the different attenuation rates for TMS with five different window diameters of the shield plate, relative to the maximum induced electric field without shield plate, which is 419.54 V/m. The smallest window diameter (10 mm) shows an attenuation of 90.89%, whereas the case with the largest window diameter (30 mm) has an attenuation of 9.65%.

In order to address the relation between focalization and maximum induced electric field, Fig. 7.2 shows a plot of the five different window sizes of the shield plate versus HPR ratio and the maximum $||\vec{E}||$. The trend is that as the window diameter of the plate increases, so does the maximum $||\vec{E}||$. The stimulation, conversely, is less focalized (i.e. has a higher HPR ratio), showing a clear compromise.

On the one hand, analyzing the focalization's relation to the maximum induced electric field in Fig. 7.2, and the values given in Table 7.1, it can be seen that for the first three window diameters, the attenuation of the electric field accounts for values above 43.27% in relation to the maximum field induced without the shield plate. On the other hand, the two greater window diameters show lower levels of attenuation, namely, 22.65% and 9.65%.

In terms of focalization improvement, in the case of the 30 mm window diameter, the stimulation still covers 59.95% less volume than the stimulated volume without the shield. Considering the dimensions of the rat brain and depending on the kind of experiment, the optimal compromise between focalization and field attenuation can be found.

Table 7.1: Focalization and attenuation of electric field in stimulation with shield plate relative to stimulation without shield plate. ($max||\vec{E}||$ of TMS without shield plate is 419 V/m. HPR ratio of TMS without shield plate is 0.1683)

Diameter (mm)	Focalization improvement ratio	Attenuation ratio of $max||\vec{E}||$
10	0.8913	0.9089
15	0.8812	0.6828
20	0.8200	0.4327
25	0.7594	0.2265
30	0.5995	0.0965

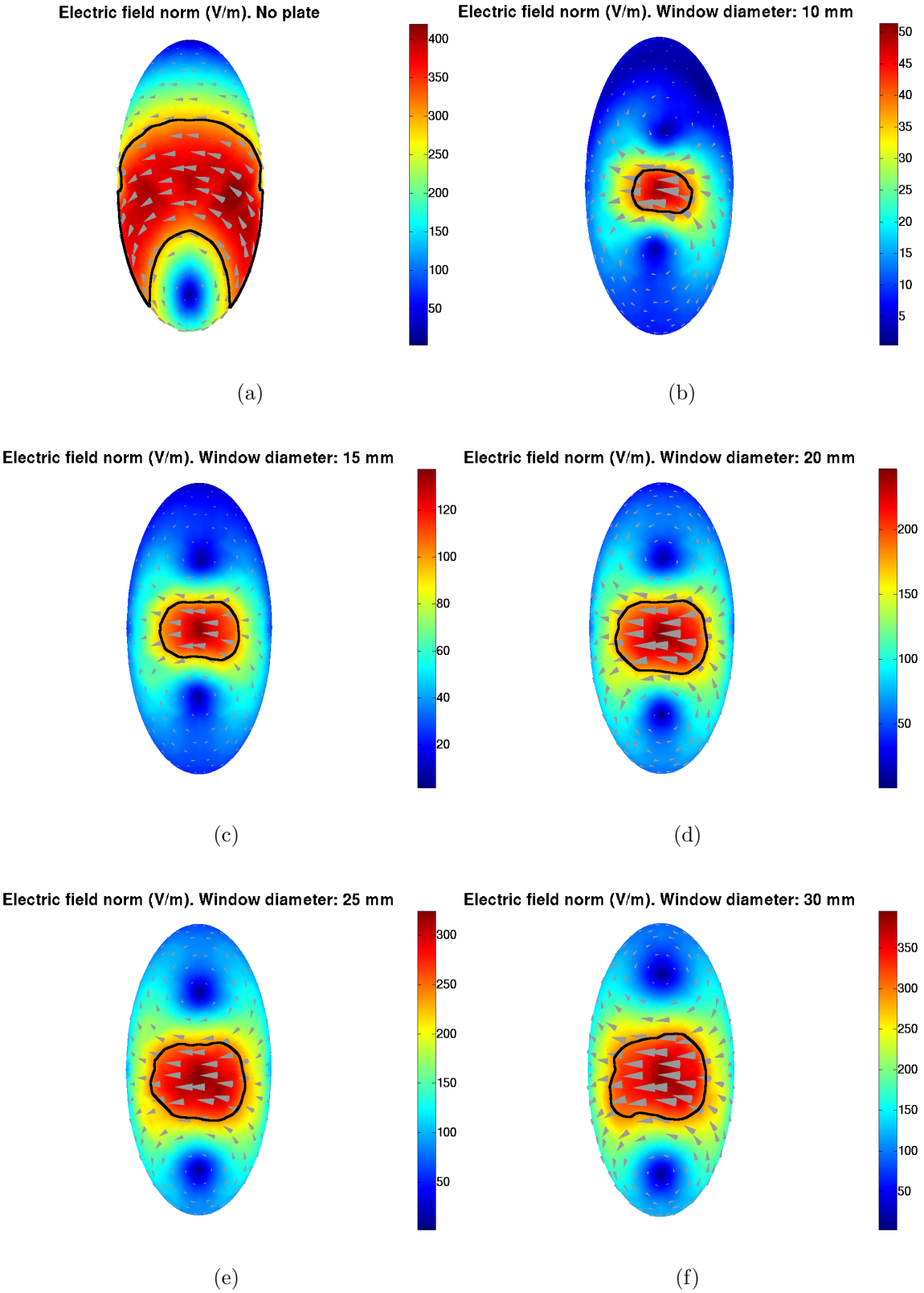

Figure 7.1: Top view of induced electric field in rat's brain model. (a) Stimulation without shield plate, and (b-f) with shield plate with 10 mm to 30 mm diameter window in 5 mm increments, respectively. The black contour indicates the half power region (HPR) and the gray cones the direction of the induced current.

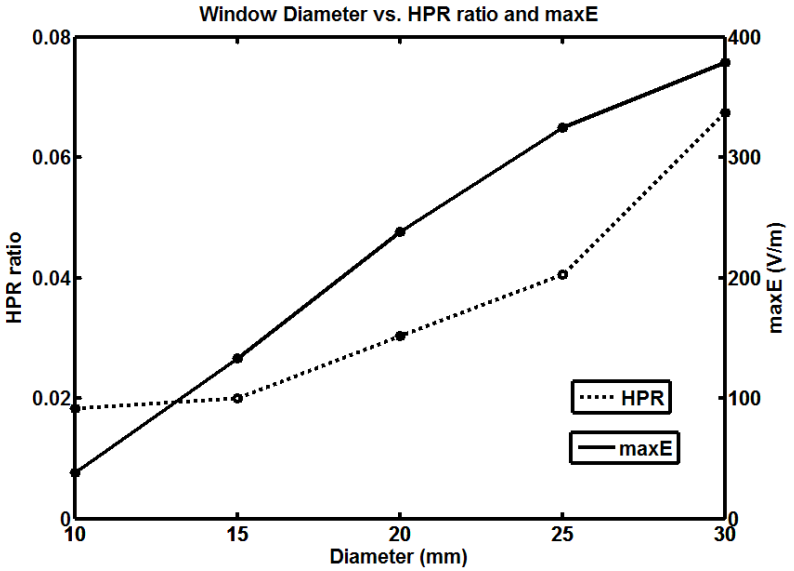

Figure 7.2: Half power region (HPR) ratio and maximum $||\vec{E}||$ values for five different diameters in the circular window of the conductive shield plate.

7.2 TMS experiments: coils with conductive shield plate

In order to investigate how the conductive shield plate can improve the focality of stimulation, we measured the induced electric fields for the two most common coil geometries (round and figure-of-eight coils), which are shown with and without the use of the conductive shield plate. We chose a window diameter of 20 mm for the shield plate, given that according to our previous simulations (Fig. 7.2), we showed this setting delivered a reasonable compromise between focality and field attenuation.

Figs. 7.3 and 7.4 show the measurements in 3D and top views. Fig. 7.3a depicts the round coil MagPro MCF75 and a diagram of the conductive shield plate (Fig. 7.3b), placed directly over the coil with a circular window diameter of 20 mm. We appreciate the well-known round pattern of the induced electric field (Fig. 7.3c,d), highly diffuse with no spatial specificity (HPR = 57.87 cm^2). We can observe a slight asymmetry in the induced electric field, presumably due to the coil's construction (tilting to one side in the casing).

The induced electric field using the conductive shield plate in the MCF75 coil is depicted in (Fig. 7.3e,f), where we observe a clear hotspot directly under the window of the conductive shield plate, improving focality drastically (HPR = 2.43 cm^2).

The hotspot is however substantially attenuated (88%) in relation to the induced electric field the coil can achieve at that point without the conductive shield plate. One can also note that the electric field magnitude beyond the conductive shield plate (surroundings) increases. This is due to the magnetic field lines that are no longer shielded by the plate and can still therefore induce an electric field.

Fig. 7.4b depicts the induced electric fields with and without conductive shield plate for the figure-of-eight coil MagPro MCB35. The spatial focality of this coil (HPR = 8.73 cm^2) is clearly superior than that of the circular coil. When using the conductive shield plate, one can still improve the focality substantially (HPR = 3.06 cm^2, nearly threefold). Nevertheless, the maximum induced electric field is also attenuated (66%) in relation to the coil without the conductive shield plate. Using the conductive shield plate with the figure-of-eight coil shows less attenuation of the induced electric field than the in the case of the round coil. This is because the shield plate's window in the figure-of-eight is directly placed under the magnetic field's hotspot.

We computed the simulations of both coils using the conductive shield plate (Fig. 7.5) to compare them to our measurements. Fig. 7.5a,b show the geometries used in the simulation for reference. Subsequently, Fig. 7.5c,d depicts the induced electric field for the round coil MCF75 without and with conductive shield plate. The same two scenarios are shown for the round coil MCB35 (Fig. 7.5e,f).

We observe that the simulations and measurements agree in their maximum induced fields with a discrepancy of 6% without the shield plate and 9% with shield plate in the case of the round coil, whereas for the figure-of-eight the discrepancy is 6% and 1% for the scenarios without and with the shield plate respectively, in all cases with respect to the theoretical result, i.e. the simulations. The aforementioned issue of the induced field beyond the shield plate in the round coil, which occurred in the measurements, was corrected in the simulations by increasing the diameter of the shield plate from 9 cm (as used in the measurements) to 12 cm.

(a)

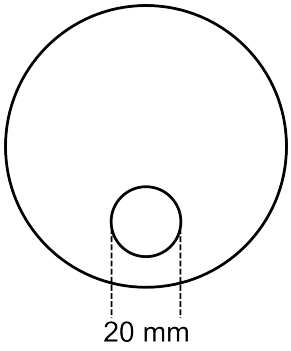

(b)

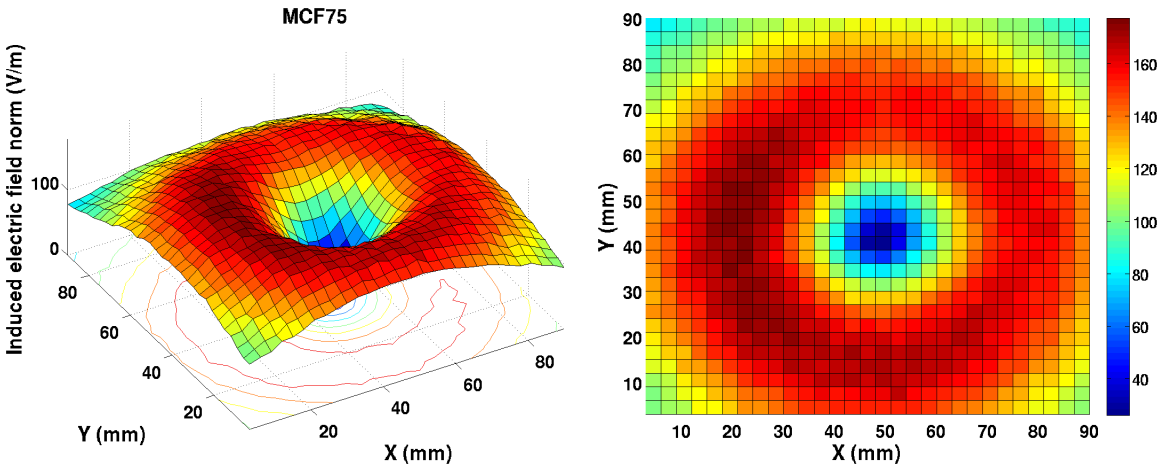

(c)

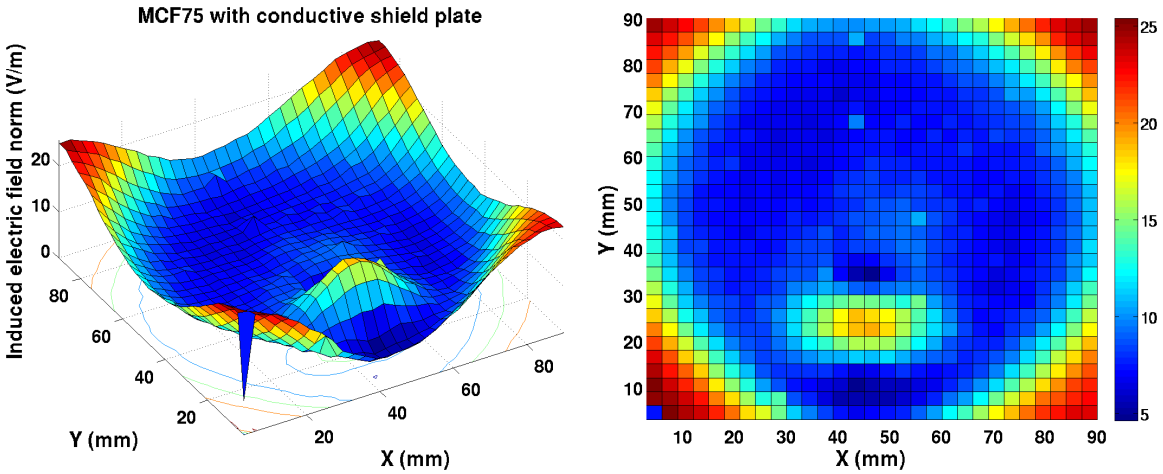

(d)

Figure 7.3: Experiment results: measurement of induced electric field by round TMS coil with conductive shield plate. (a) MCF75 round coil (MagVenture A/S, DK, with friendly permission). (b) Diagram of the conductive shield plate with its circular window (20 mm diameter). (c) Induced electric field without and (d) with the conductive shield plate, all plots in V/m.

(a)

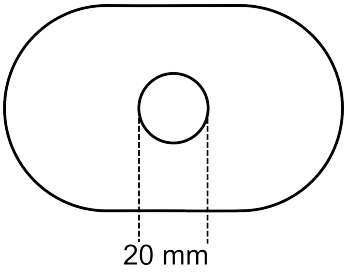

(b)

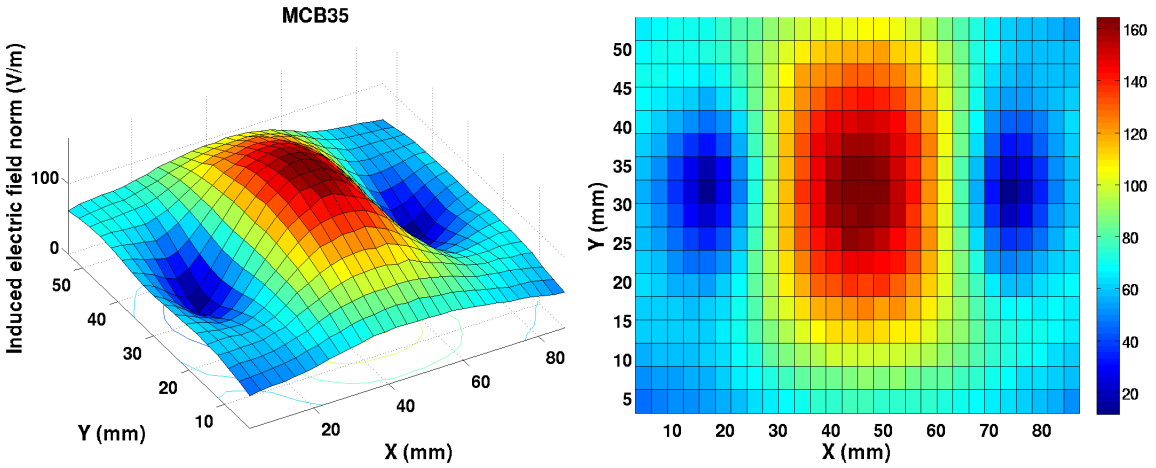

(c)

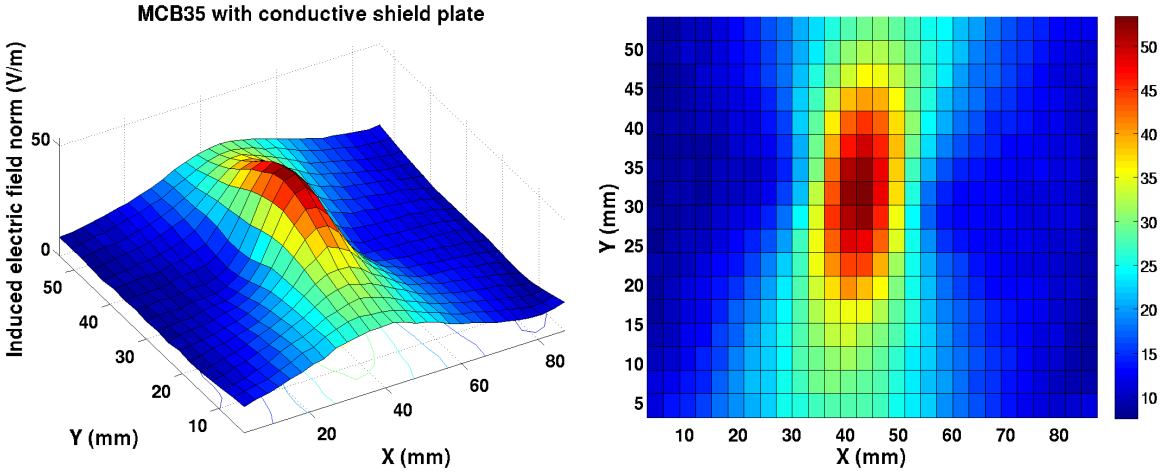

(d)

Figure 7.4: Experiment results: measurement of induced electric field by figure-of-eight TMS coil with conductive shield plate. (a) MCB35 coil (MagVenture A/S, DK, with friendly permission). (b) Diagram of the conductive shield plate with its circular window. (c) Induced electric field without and (d) with conductive shield plate, all plots in V/m.

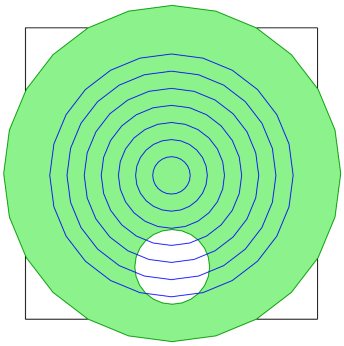

(a)

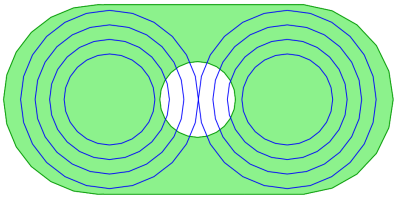

(b)

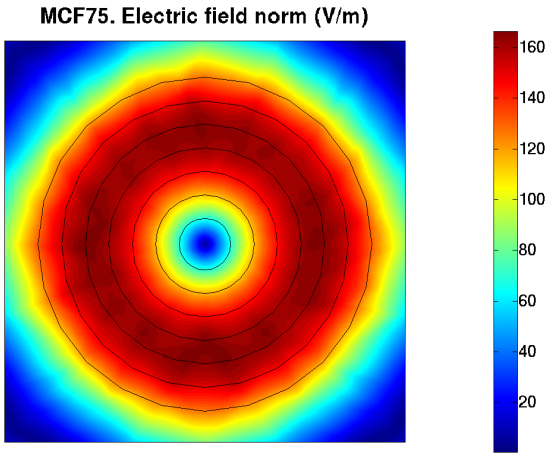

(c)

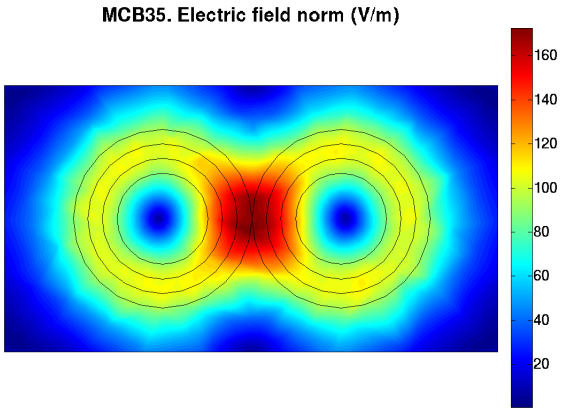

(d)

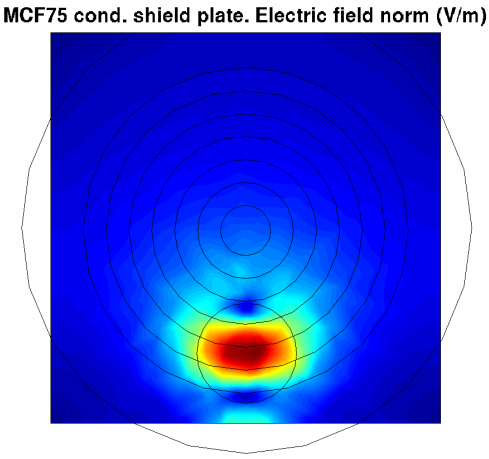

(e)

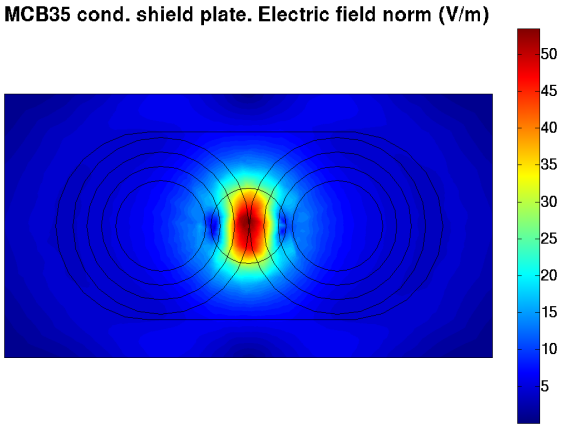

(f)

Figure 7.5: Simulations of the experimental setup: use of conductive shield plate in TMS coil for increased focality. (a) and (b) show the simulation geometries for the round MCF75 and figure-of-eight MCB35 coils respectively, with coil (blue) and shield plate with 20 mm diameter window (green). The induced electric fields are shown without and with the conductive shield plate for the MCF75 (c,e) and MCB35 (d,f) coils respectively (coil and shield plate geometries are overlaid in plots).

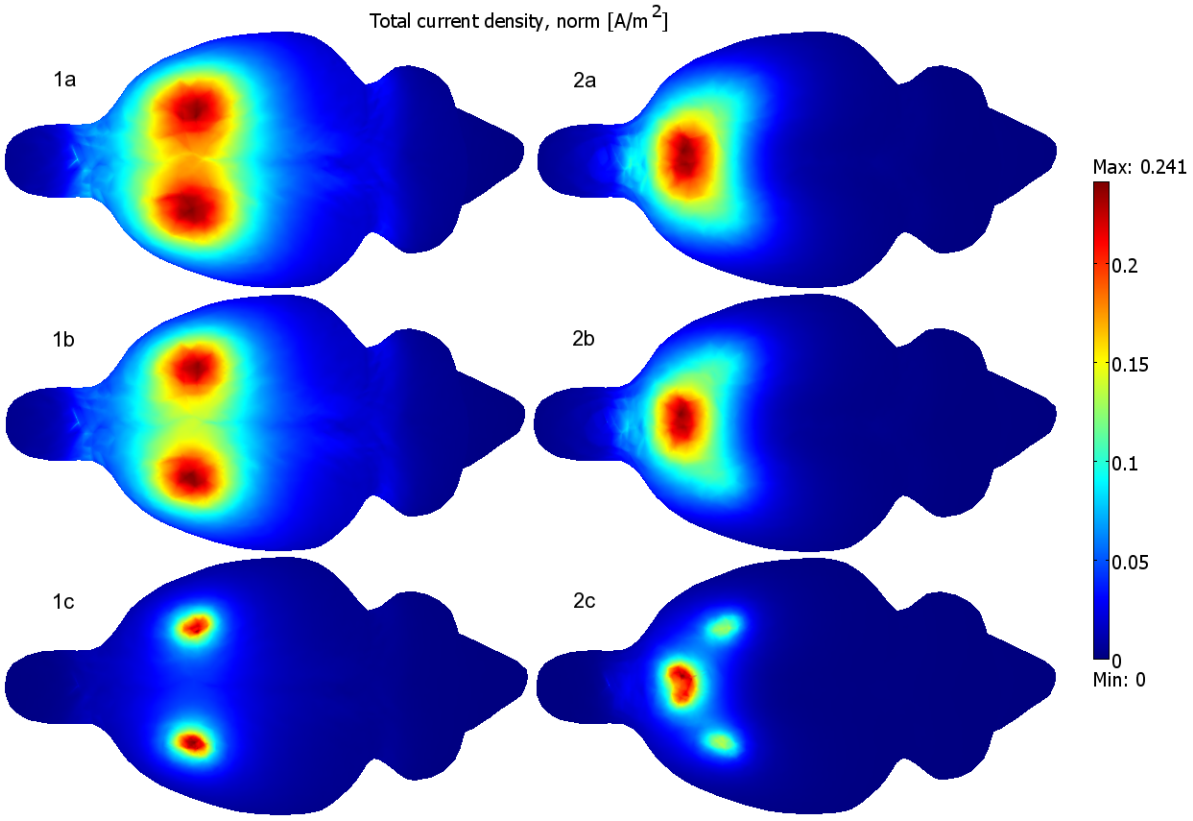

Figure 7.6: Top view of the magnitude of the current density distribution at the surface of the rat brain model for: (1) two-electrode, and (2) three-electrode configurations in three depth scenarios: (a) electrodes fixed at the surface of the skull, (b) electrodes fixed halfway through the skull and (c) electrodes in contact with the CSF. For comparison purpose, the applied current was adjusted to have the maximum current density of 0.241 A/m^2 at the brain surface, which corresponds to the maximum current density applying 15 μA in the two-electrode configuration with electrodes fixed at the surface of the skull (1a).

7.3 tDCS in realistic rat model

We used our realistic rat model to investigate the influence of electrode implantation depth on the induced fields in the brain, considering two electrode configurations similar to those portrayed in a recent study where neuronal entrainment of the rat *in vivo* was observed applying low intensity electrical stimulation [135]. Throughout this work, we assume that the electric field magnitude is correlated to brain activity modulation, in contrast to considering the activating function (electric field derivative). This assumption may be appropriate if the electric fields are uniform at the scale of the neuron and if neuronal modulation is directly related to uniform electric field magnitude [104], [114]. For this analysis we considered current density magnitude plots, which result from multiplying the electric field by the corresponding

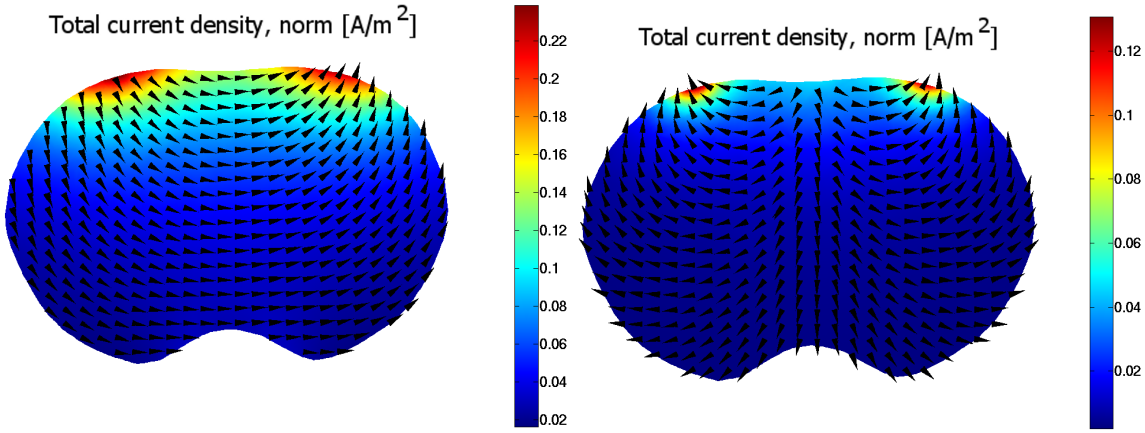

(a) (b)

Figure 7.7: Magnitude of current density in coronal slices of the rat brain model for the two-electrode (above) and three-electrode (below) configurations in bregma for the second implant depth scenario, i.e., electrodes halfway through skull. The gray cones show the direction of the current flow.

conductivity value ($J = \sigma E$).

The magnitude of the current density at the brain's surface for the two electrode configurations in the three depth scenarios is shown in Fig. 7.6. For both configurations, the most diffuse stimulation occurs in the first depth scenario, i.e. the electrodes implanted on the surface of the skull (Fig. 7.6: 1a, 2a). The most focal stimulation is reached in the third depth scenario, i.e. the electrodes implanted in contact with the CSF (Fig. 7.6: 1c, 2c), as expected due to their higher proximity to the brain. To asses the focality of stimulation, we measured the volume of tissue revealing a current density magnitude higher than 70% of the maximum current density revealed at the brain surface.

Table 7.2 shows the focality for all simulations. Focality is higher for all cases in the three-electrode in contrast to the two-electrode configuration. This can be attributed to the fact that in the two-electrode case will always generate two hotspots, whereas in the three-electrode case there is only one hotspot because the current splits flowing from the anode to the two cathodes. In terms of equivalent applied current I_{eq}, both electrode configurations show substantial decrease of I_{eq} with insertion depth, as we could assume (see Table 7.2). The largest I_{eq} difference between electrode configurations occurs in the second depth scenario, where the three-electrode configuration requires 16.5% less I_{eq}, presumably due to the anode's higher proximity to the CSF than the cathodes in the three-electrode configuration.

Coronal slices of the spatial distribution of the current density in the brain model are exemplified at the level of bregma (see Fig. 7.7) for both electrode configurations in the second depth scenario (with cones showing the direction of the current flow). In the two-electrode configuration, the current flows along the coronal plane from anode to cathode and the magnitude of the current density is near its maximum. In the case of the three-electrode configuration, the current splits into both cathodes and its magnitude at each location is nearly half of that seen under the anode.

Table 7.2: Focality and equivalent applied current for a maximum current density of 0.241 A/m^2 for two electrode configurations in three implant depth scenarios

	Two-electrode		Three-electrode	
Depth scenario	Focality (mm^3)	I_{eq} (μA)	Focality (mm^3)	I_{eq} (μA)
Epicranial	7.10	15	2.06	14.92
Halfway in skull	3.44	13.04	1.14	10.89
Contact with CSF	0.21	3.27	0.19	3.43

7.4 tDCS in the human

7.4.1 Electric field distribution

The electric field distribution at the surface of the brain and at the coronal slice where the target is located for the seven optimization schemes (CLS, l_1-norm, 4-by-1, 3x3, Top-k, SOS and OMP) is presented in Fig. 7.8. For all optimization approaches, target intensity of 0.17 V/m and radial orientation of the field were specified, which is the intensity achieved at the target by the conventional pads applying 1 mA. The target is located directly under the C4 location (EEG 10/10 configuration) at the surface of the brain, which corresponds to the motor cortex.

When using contralateral pads (Fig. 7.8a) the electric field distribution is widely diffuse, covering the majority of the cortex and showing maxima at the bottom of several sulci, the so-called "clustering-effect" [8] due to cerebrospinal fluid in the cortical folding.

All optimized approaches show a noticeable improvement in focality in their respective electric field distributions compared to the conventional montage. From the schemes with unconstrained active electrodes, the CLS with EEG 10/10 approach

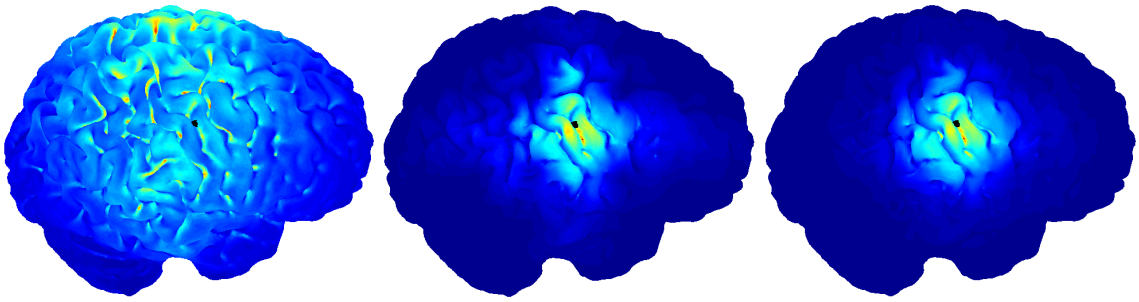

(a) Conventional pads (b) CLS (c) l_1-norm

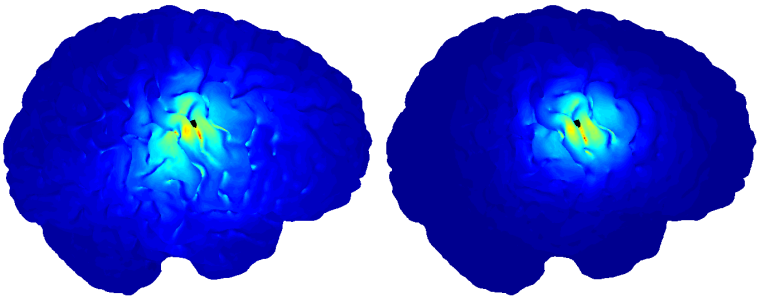

(d) 4-by-1 (e) 3x3

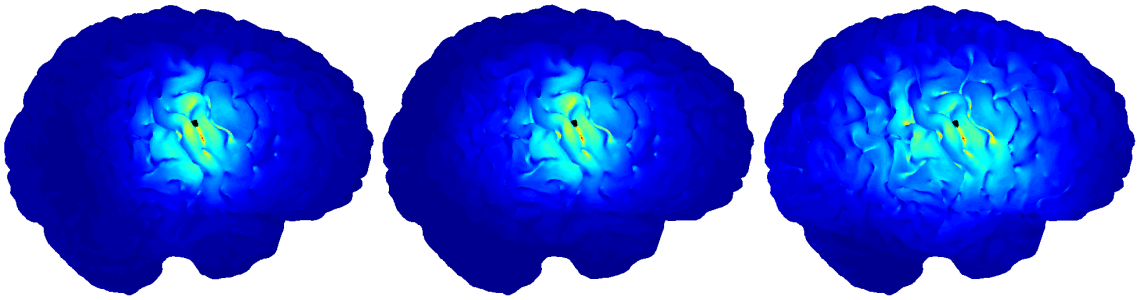

(f) Top-k (g) SOS (h) OMP

Figure 7.8: Induced electric field in cortex (red is maximum and blue minimum) for: (a) conventional 35 cm^2 pads. Schemes with unconstrained active electrodes: (b) CLS and (c) l_1-norm. Patch schemes: (d) 4-by-1 patch and (e) 3x3 patch (both in 5/5 arrangement). Subset selection schemes: (f) Top-k, (g) SOS and (h) OMP. Target is located under C4 (motor cortex) and depicted as a black region in the cortex maps. Orientation of the field was set to radial and target intensity to 0.17 V/m (field intensity at target with conventional pads at 1 mA).

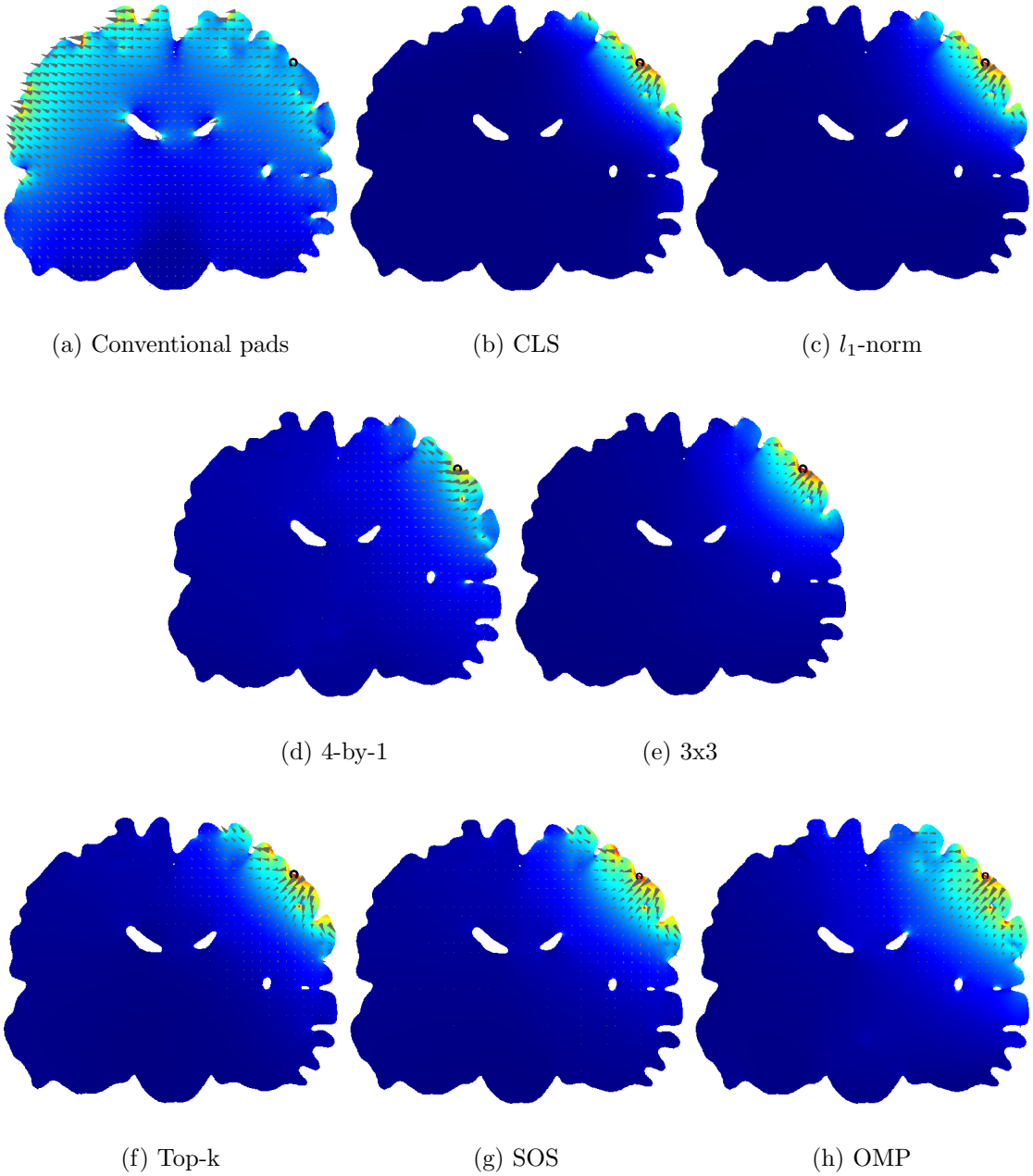

(a) Conventional pads (b) CLS (c) l_1-norm

(d) 4-by-1 (e) 3x3

(f) Top-k (g) SOS (h) OMP

Figure 7.9: Induced electric field in coronal slice (red is maximum and blue minimum) for: (a) conventional 35 cm^2 pads. Schemes with unconstrained active electrodes: (b) CLS and (c) l_1-norm. Patch schemes: (d) 4-by-1 patch and (e) 3x3 patch (both in 5/5 arrangement). Subset selection schemes: (f) Top-k, (g) SOS and (h) OMP. Target is located under C4 (motor cortex) and depicted as a black ring in the slices. The gray cones show the direction of the current flow. Orientation of the field was set to radial and target intensity to 0.17 V/m (field intensity at target with conventional pads at 1 mA).

achieves not only focality on the surface but the most confined distribution, as seen in the coronal slice (Fig. 7.8b), and it does so using 63 active electrodes. The l_1-norm approach achieves a similar electric field distribution by only using 19 active electrodes (for this target location and given intensity). However, the coronal slice shows the field distribution is not as confined as CLS (Fig. 7.8c).

In the patch schemes, the 4-by-1 patch (with 5/5 arrangement) shows a more diffuse field distribution than the previous two schemes. Misalignment in the field orientation is also noticeable in the respective coronal slice (Fig. 7.8d). The 3x3 electrode patch array yields a more focal stimulation (Fig. 7.8e) than the 4-by-1, though not as confined in depth as the first two schemes with unconstrained active electrodes.

The subset selection schemes (Top-k, SOS and OMP) also show a more diffuse electric field distribution than the first two schemes (CLS and l_1-norm). However, they do so by only using four active electrodes (Fig. 7.8f,g,h). Top-k and SOS show similar performance and OMP the most diffuse field distribution.

7.4.2 Focality and misalignment

Focality and misalignment curves are depicted in Figs. 7.10, 7.11 and 7.12. Curves stop at their maximum attainable electric field intensity. The first aspect to point out is that all optimization approaches show improved focality over the conventional configuration at its maximum attainable electric field at the target (HMR of 68 mm at 0.34 V/m, misalignment of 12 degrees). Moreover, all optimization approaches go beyond the conventional approach in their maximum attainable electric field at the target.

The CLS approach shows an HMR of 24 mm until 0.22 V/m, where it starts to gradually increase with its misalignment staying constant at ca. 4 degrees. Note that CLS is the only method that can achieve greater intensities than those in the plot (Fig. 7.10a) at the expense of typically requiring most available channels.

The l_1-norm minimization approach (Fig. 7.10b) performs just as well with a reduced number of active channels, reaching a maximum attainable intensity of 0.43 V/m with HMR of 52 mm and misalignment below 5 degrees for the entire range.

Fig. 7.11 shows the optimized 4-by-1 patch for both arrangements. The 4-by-1 5/5 obtains better focality in lower intensities, however, in a shorter range in contrast to the 4-by-1 10/10, up to 0.12 V/m and 0.23 V/m respectively. We observe that

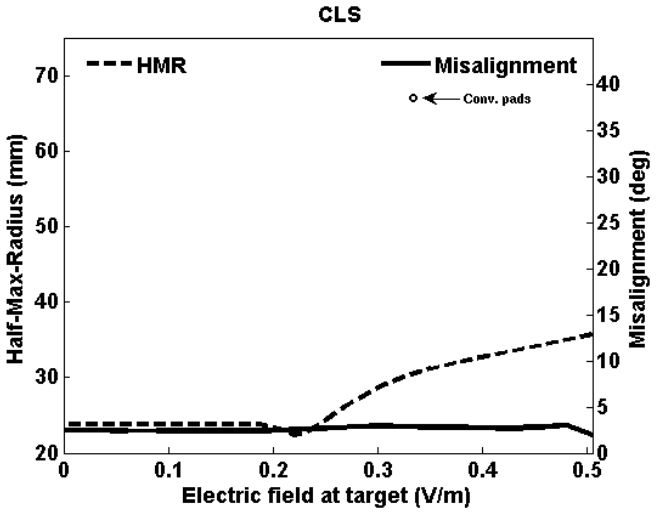

(a)

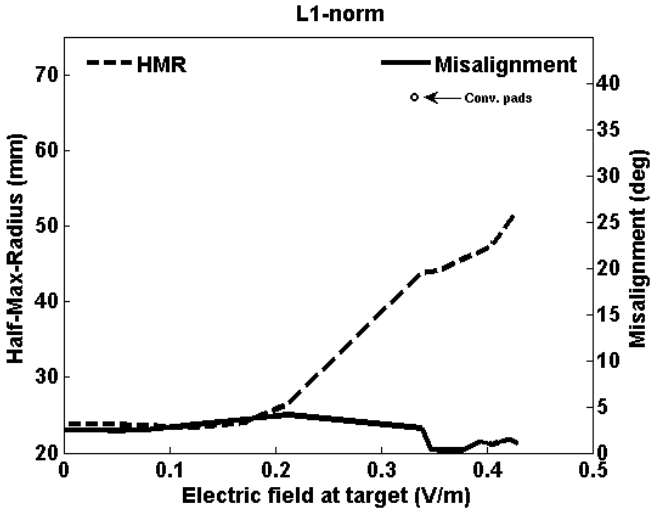

(b)

Figure 7.10: Focality and misalignment for optimization schemes with unconstrained active electrodes. (a) CLS with EEG 10/10 configuration; (b) l_1-norm constrained optimization with EEG 10/10 configuration. The brain target for all methods was located directly under the C4 electrode and the orientation of the field was set as radial. The conventional rectangular pads configuration applying a current of 2 mA achieves a target intensity of 0.34 V/m, showing an HMR of 68 mm with 12 degrees misalignment.

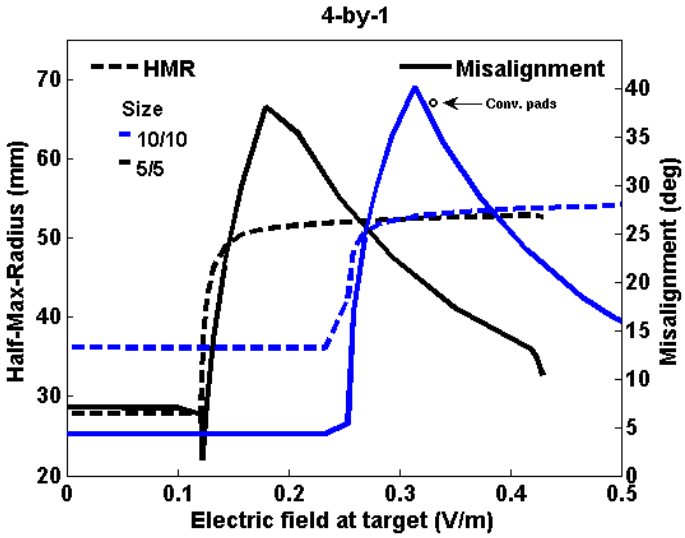

(a)

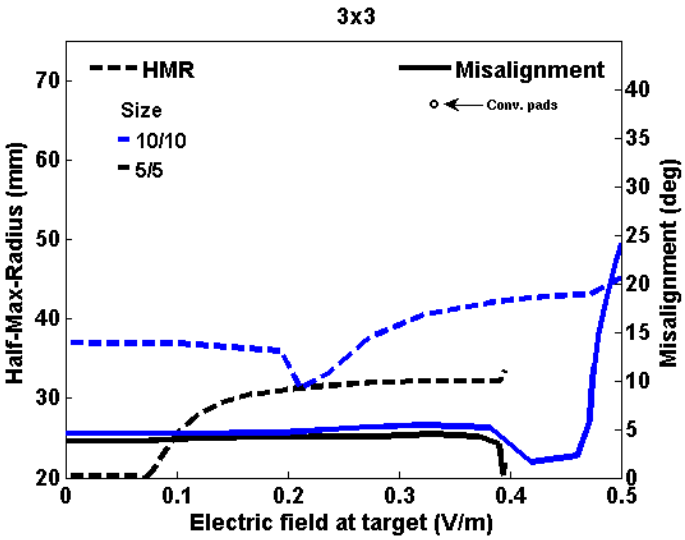

(b)

Figure 7.11: Focality and misalignment curves for patch optimization schemes. (a) optimized 4-by-1 electrode patch using CLS in two sizes: 5/5 and 10/10 spatial distributions; (b) optimized 3x3 electrode array patch using CLS in two sizes: 5/5 and 10/10 spatial distributions. The brain target for all methods was located directly under the C4 electrode and the orientation of the field was set as radial. The conventional rectangular pads configuration applying a current of 2 mA achieves a target intensity of 0.34 V/m, showing an HMR of 68 mm with 12 degrees misalignment.

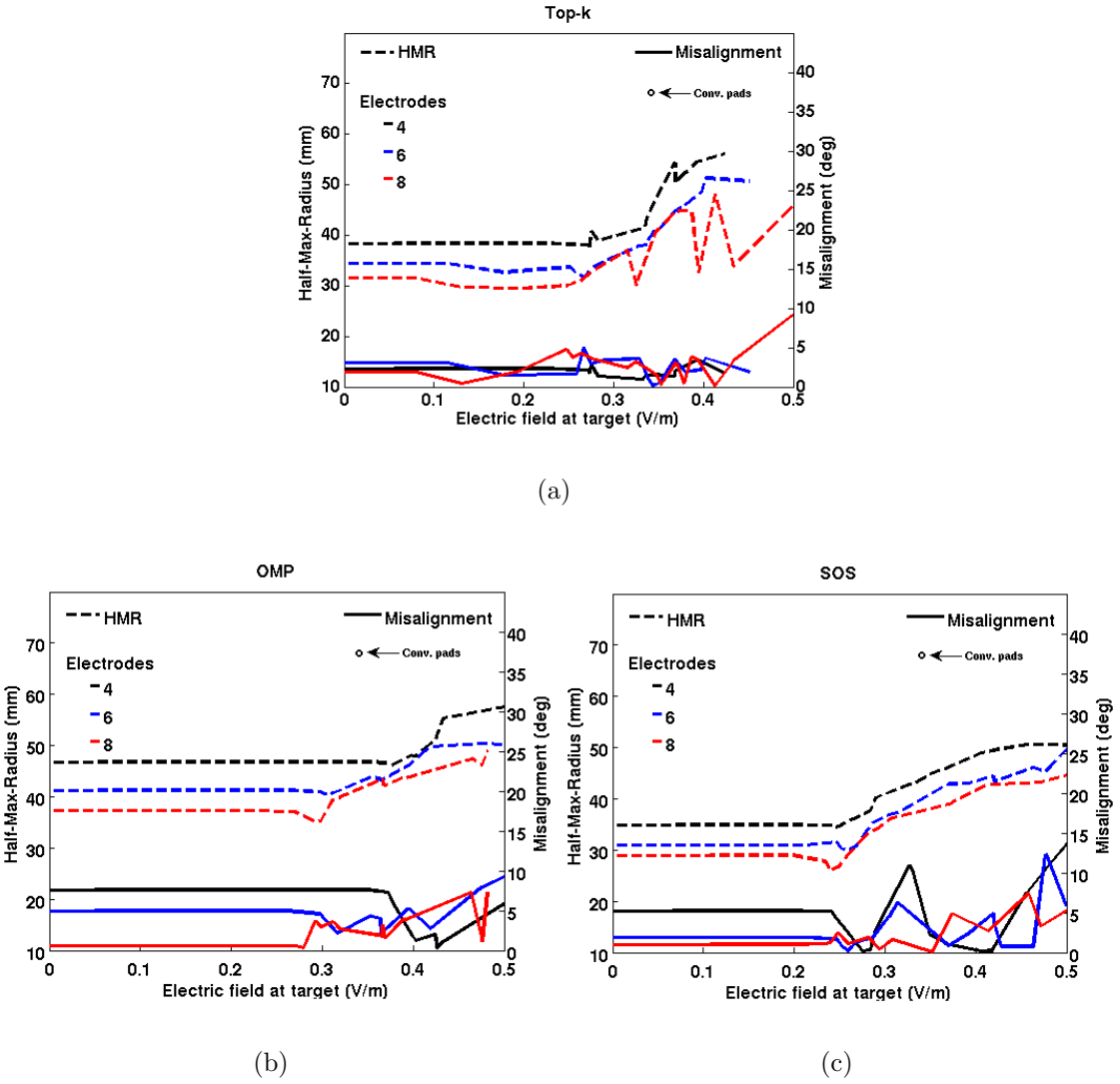

Figure 7.12: Focality and misalignment curves for subset selection optimization schemes. (a) Top-k subset selection with extra optimization step using CLS for four, six and eight active electrodes out of the EEG 10/10 configuration; (b) orthogonal matching pursuit (OMP) and (c) stepwise optimal selection (SOS). The brain target for all methods was located directly under the C4 electrode and the orientation of the field was set as radial. The conventional rectangular pads configuration applying a current of 2 mA achieves a target intensity of 0.34 V/m, showing an HMR of 68 mm with 12 degrees misalignment.

as the HMR increases so does misalignment, up to a peak near 40 degrees when it starts decreasing. The intuitive use of the 4-by-1 applying the same current to the four external electrodes and having the central electrode as return can also be seen in Fig. 7.11a, corresponding to the plateau before the HMR raises, precisely the point at which the optimization adjusts the applied currents in order to allow a wider range of attainable intensities at the cost of a higher misalignment. The 3x3 patch array achieves stable focality throughout the attainable field intensity range with an HMR below 31 mm and 45 mm for the 5/5 and 10/10 cases respectively.

Misalignment of the 3x3 5/5 stays below 5 degrees, whereas in 3x3 10/10 there is an increase at the end of the range leading up to 24 degrees at 0.5 V/m. In both 4-by-1 and 3x3 patches having a broader spatial distribution (10/10) decreases focality but extends the maximum attainable field at the target. We attribute this to the increased shunting effect of the scalp due to the electrode's higher proximity.

The subset selection optimization schemes are shown for four, six and eight active channels (Fig. 7.12). As one would expect, the focality improves as the method has more available channels. However, note that these methods outperform the optimized 4-by-1 patch in higher intensities and have misalignments lower than 10 degrees in the three cases for most of the target intensities.

Interestingly, the subset selection schemes perform similarly to the l_1-norm at higher intensities. Having six active channels yields even better focality than the l_1-norm above ca. 0.27 V/m. In the Top-k scheme, this is due to the increased freedom the subset selection method is granted in the second optimization step, where channels are constrained individually. Among the three schemes, the SOS shows the best performance across all target intensities, showing similar, though more variable misalignments than the other two schemes at higher intensities.

Table 7.3 shows the focality improvement of the five optimized approaches against the conventional pads for the radial target at C4 also portrayed in Figs. 7.10, 7.11 and 7.12. All methods achieve substantial improvements. Those using limited number of channels, i.e., the subset selection schemes show 71%, 76% and 65% improvement, for the Top-k, SOS and OMP schemes respectively. The 4-by-1 patch gives improvements of 55% in both modalities. The 3x3 5/5 patch shows a 89% improvement, and 78% in the 10/10 modality. The improvement is defined as the volume decrease in the sphere with the corresponding HMR. The sphere volume is $(\mathrm{HMR})^3$.

Table 7.3: Focality improvement over conventional pads (HMR of 68 mm at 0.34 V/m) for radial target under C4. Improvement is expressed as the volume decrease of the HMR sphere.

Method	HMR (mm)	Improvement (%)
CLS	31	90
l_1-norm	44	72
4-by-1 (5/5)	52	55
4-by-1 (10/10)	52	55
3x3 (5/5)	32	89
3x3 (10/10)	41	78
Top-k* (c = 4)	45	71
SOS (c = 4)	42	76
OMP (c = 4)	48	65

*c is the number of active channels

7.4.3 Average performance

We have portrayed the performance of the optimization schemes in terms of their electric field distributions and analyzed their behavior as target intensity increases. To fully characterize the presented schemes, we analyzed their average performance in different targets across the cortex. Table 7.4 summarizes the results of the evaluation for 22 different radial targets, displaying the mean focality, misalignment, number of active electrodes, and total current flowing through electrodes and reference. We observe that the trend of Figs. 7.10, 7.11 and 7.12 is maintained in the averaged results with the Top-k method showing the worst average focality. However, in terms of required current the Top-k scheme is the most conservative in radial stimulation and comes second in tangential. Note however that the l_1-norm method will hold the $2s_{max}$ constraint for even higher field intensities.

The same evaluation was done for tangential fields in 22 targets across the cortex, and is shown in Table 7.5. We observe in general lower focality, as reported in [12] and higher misalignments than the radial counterpart. The schemes in general require more current, except in the case of the l_1-norm and 3x3 approaches. The

Table 7.4: Mean performance of optimized multi-electrode tDCS across the cortex (22 targets) for radial field orientation and electric field intensity of 0.3 V/m.

	Orientation: Radial			
Method	HMR (mm)	Misalignment (deg)	Total current† (mA)	Active channels
CLS	34.23	10.49	19.38	63
l_1-norm	49.33	11.01	3.99	13.31
4-by-1 (10/10)	49.08	12.86	4.45	4
3x3 (10/10)	43.25	9.98	8.82	8
Top-k* (c = 4)	59.49	13.46	3.48	4
SOS (c = 4)	49.49	9.74	5.44	4
OMP (c = 4)	54.81	11.93	4.12	4

† current flowing through active electrodes and reference ($D_e(\sum|s_m| + |\sum s_m|)$, where D_e is the electrode surface area.

* c is the number of active channels

Table 7.5: Mean performance of optimized multi-electrode tDCS across the cortex (22 targets) for tangential field orientation and electric field intensity of 0.3 V/m.

	Orientation: Tangential			
Method	HMR (mm)	Misalignment (deg)	Total current† (mA)	Active channels
CLS	40.12	18.64	21.95	63
l_1-norm	57.19	11.39	4	6.27
4-by-1 (10/10)	63.19	27.15	4.64	4
3x3 (10/10)	54.18	21.48	8.43	8
Top-k* (c = 4)	59.36	11.27	4.09	4
SOS (c = 4)	52.93	14.15	5.62	4
OMP (c = 4)	56.96	10.02	4.72	4

† current flowing through active electrodes and reference ($D_e(\sum|s_m| + |\sum s_m|)$, where D_e is the electrode surface area.

* c is the number of active channels

l_1-norm scheme, in contrast, uses less (nearly half) active channels than in the radial case.

CLS holds the best performance for both orientations in terms of focality; however, its implementation is unrealistic given that it always requires 63 active electrodes

and ca. 4 times more current than all other approaches. The l_1-norm scheme allows to reduce the number of active electrodes to 14. Nevertheless, it does not outperform the other schemes with constrained number of active electrodes. The patch approaches show a superior performance than the l_1-norm and similar to the subset selection in the radial case. However, in the tangential case the subset selection schemes outperform the 4-by-1 and come close to the 3x3 using half of electrodes.

Overall, (excluding CLS because of its practicality issues) SOS shows the best performance compromise. Using only 4 electrodes it performs just as good as the other methods in the radial case. In the tangential case it outperforms all other schemes in terms of focality. In terms of misalignment it performs best in the radial case and among in both cases. We shall remember that the choice in field direction can be arbitrary in the optimization. Radial and tangential fields are of particular relevance since it has been shown that these orientations induce maximum polarization in neurons somata [10].

7.4.4 Focality maps

Topographic plots across the cortex for radial targeting with a magnitude of 0.3 V/m are shown in Fig. 7.13 and for tangential targeting in Fig. 7.14. The plots show a focality map measured in terms of the half-max-radius (HMR), reflecting the performance of each optimized multi-electrode scheme in 22 targets spread across the cortex.

In the radial targeting case (Fig. 7.13) we note that the best performance in the schemes with unconstrained number of active electrodes (Fig. 7.13, top row) is achieved by the CLS scheme. The l_1-norm scheme performs at best in targets located close to the auditory cortex. Conversely, it shows its worst performance for targets in the parietal lobe. The patch approaches (Fig. 7.13, middle row) show a similar pattern to the CLS scheme, however, with worse focality values, which makes sense because they use the same optimization procedure but they are constrained to using 4 and 8 active electrodes respectively. The 3x3 patch performs in general better than the 4-by-1, given the increased number of active electrodes.

Among the subset selection schemes, all using 4 active electrodes (Fig. 7.13, bottom row), our SOS scheme performs best, achieving its best focality in the auditory cortex (as the l_1-norm); however, with better focality in the parietal lobe. The OMP

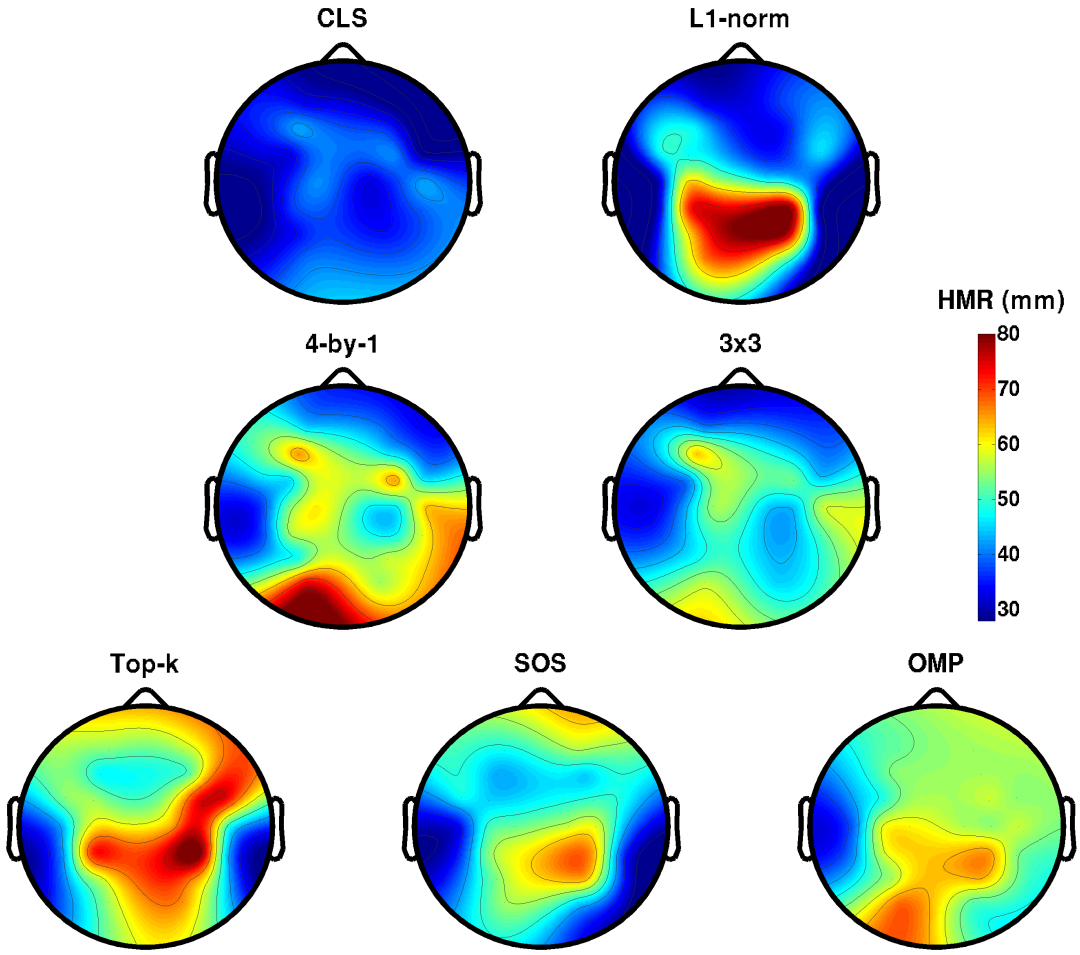

Figure 7.13: Radial focality maps. Topographic plots of the cortex depicting the performance of each optimization scheme in terms of the half-max-radius (HMR). The first row shows the schemes with unconstrained active electrodes, i.e. CLS and l_1-norm. The second row shows the patch schemes, i.e. 4-by-1 and 3x3. The third row shows the subset selection schemes, i.e. Top-k, SOS and OMP.

scheme shows the second best subset selection results, with its worst performance at the occipital and parietal lobes. The Top-k scheme shows a similar pattern to the l_1-norm but with inferior performance in the frontal lobe.

In the tangential case (Fig. 7.14) CLS performs the best. The l_1-norm scheme shows an HMR below 60 mm overall except at the occipital and left frontal/temporal lobes. The patch schemes show again a worse version of the CLS, with the 3x3 again showing much better performance. The subset selection methods show in general worse performance in frontal targets, with SOS being again the best of the three and the second best scheme overall. OMP, just as in the radial case performs better than Top-k showing noticeable better focality in the parietal and occipital lobes.

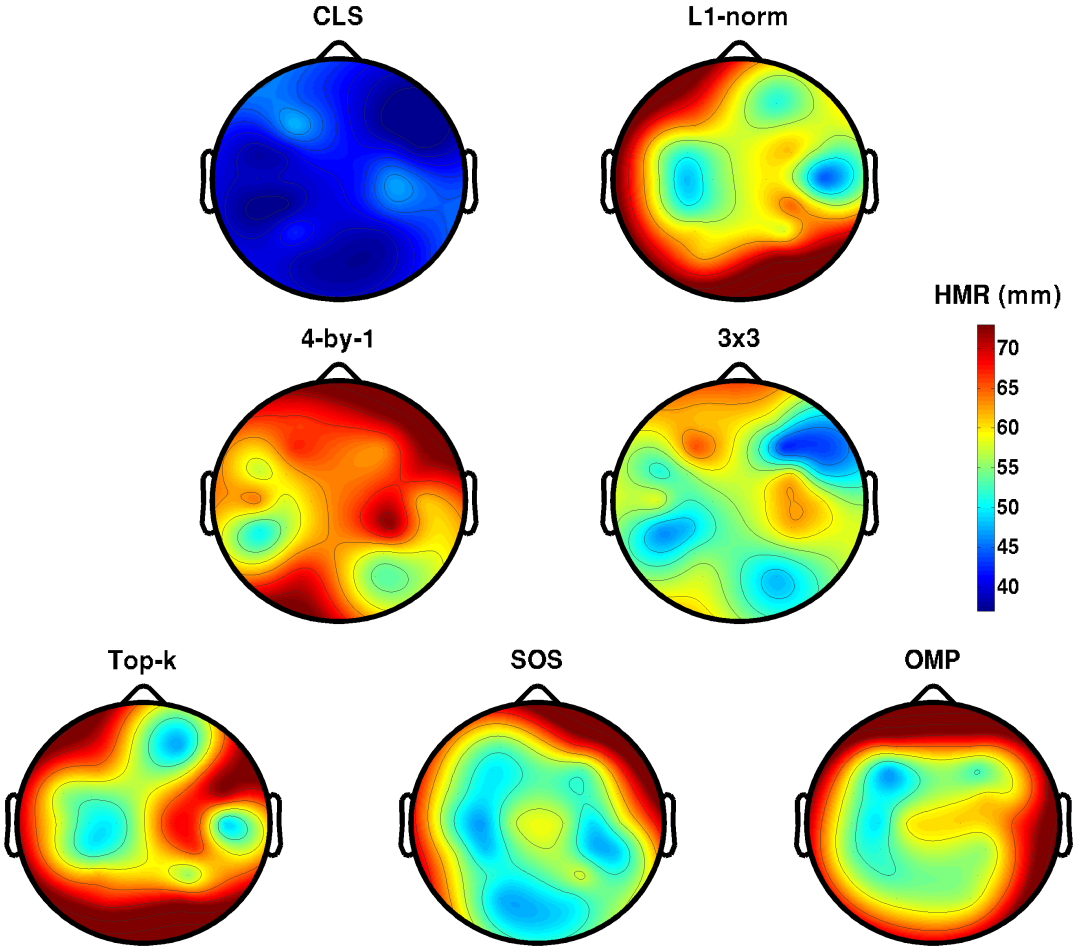

Figure 7.14: Tangential focality maps. Topographic plots of the cortex depicting the performance of each optimization scheme in terms of the half-max-radius (HMR). The first row shows the schemes with unconstrained active electrodes, i.e. CLS and l_1-norm. The second row shows the patch schemes, i.e. 4-by-1 and 3x3. The third row shows the subset selection schemes, i.e. Top-k, SOS and OMP.

7.4.5 Multi-targeting

A particularly useful feature that can be integrated to the optimized electric stimulation schemes is to have multiple-targets simultaneously. In Fig. 7.15 we show the multi-targeting capability of optimized tDCS for two targets in the brain: one in the auditory cortex and a second one in the contralateral motor cortex. We observe that the optimization successfully achieves focal stimulation of both targets, with radial orientation of the field in both cases. This result was obtained using the EEG 10/10 configuration and the CLS optimization scheme. However, multi-targeting could be achieved with any of the schemes analyzed in this work.

Multi-targeting can be used when symmetric/contralateral stimulation is desired

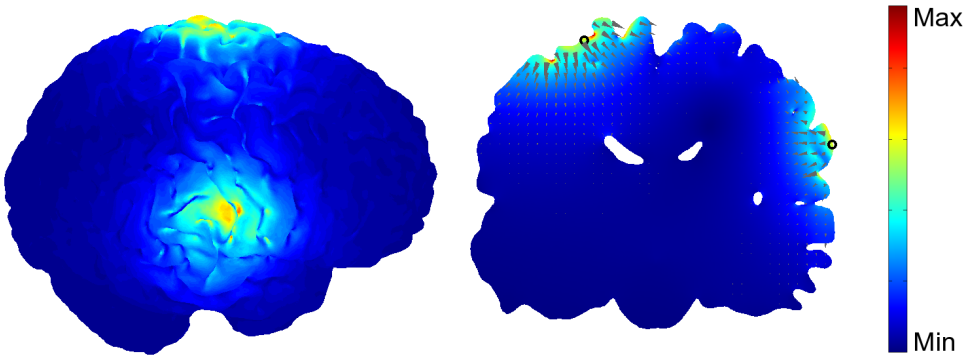

Figure 7.15: Multi-targeting capability of optimized tDCS. Electric field at surface of the brain (left) and coronal slice (right) showing the focal and simultaneous stimulation of two targets (depicted as black rings in the slice). One target is located in the auditory cortex and other in the contralateral motor cortex. The orientation of the electric field was set radial to the surface. The gray triangles show the direction of the current flow.

[106], avoiding the reversed effect of the cathode electrode in the conventional pads montage, under which the direction of the current is opposite to the anode's.

7.5 Experimental results: inverse planning

The measurements of the inverse planning *in vitro* are shown for radial (Fig. 7.16) and tangential (Fig. 7.17) targeting. In both figures, at the top, we show a diagram of the setup depicting the available electrodes ($M = 7$) for the optimization and the ground. Also shown are the target's location and desired orientation of the electric field. The targets are either radial and tangential to the center of the measurement field (also to the center of the petri dish), which is shown as a dotted line from the target to the center. We measured the electric potential distribution with the tungsten needle electrode and subsequently calculated the induced electric field i.e. $\vec{E} = -\vec{\nabla}V$, since the electric field $\vec{E}$ is the spatial gradient of the electric potential V, where $\vec{\nabla}$ is the gradient.

We employed the stepwise optimal selection (SOS) optimization scheme for the measurements in order to reach a magnitude of 1.2 V/m in the radial case and 1.6 V/m in the tangential case. These magnitudes were chosen arbitrarily. We performed the optimization and obtained the electrode currents that were later applied in the experiments.

In the radial case (Fig. 7.16) we observe that the electric potential distribution has small perturbations in the measurements in comparison to the simulation. However, the measurements' distribution as well as the magnitudes are in agreement. The small perturbations in the measured electric potential are also present in the calculated norm of the electric field. We appreciate however, that the desired orientation of the field agrees with the simulation with a misalignment of 6 degrees. The magnitude in the measured electric field at the target is 1.21 V/m.

The measurement for the tangential case (Fig. 7.17) also agrees in the electric potential distribution and magnitudes. The perturbations in this measurement were greater than in the radial case. The measurement has a magnitude of 1.19 V/m at the target with a misalignment of 2 degrees.

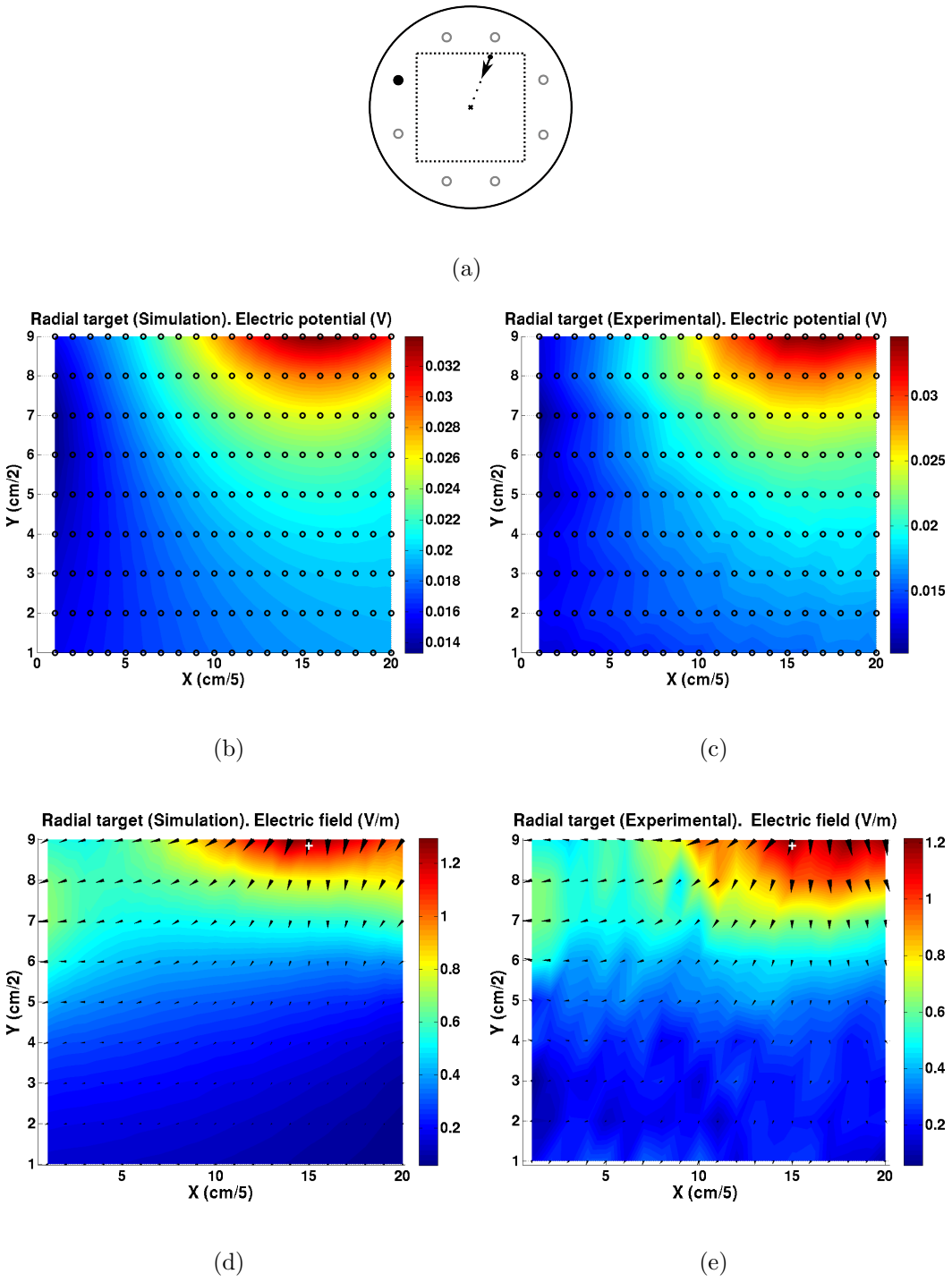

Figure 7.16: Experimental results: measurements of optimized multi-electrode inverse planning of electrical stimulation, radial case. (a) Petri dish diagram of multi-electrode configuration with available electrodes (gray rings) and ground (black circle). The arrow shows the target for optimization with desired orientation. The dotted-line square is the measurements' area. (b) Simulated and (c) experimental electric potential distribution (black rings are measurement points). (d) Simulation and (e) experimental distribution of the electric field. The white cross in (d) and (e) is the target and black triangles depict the electric field orientation.

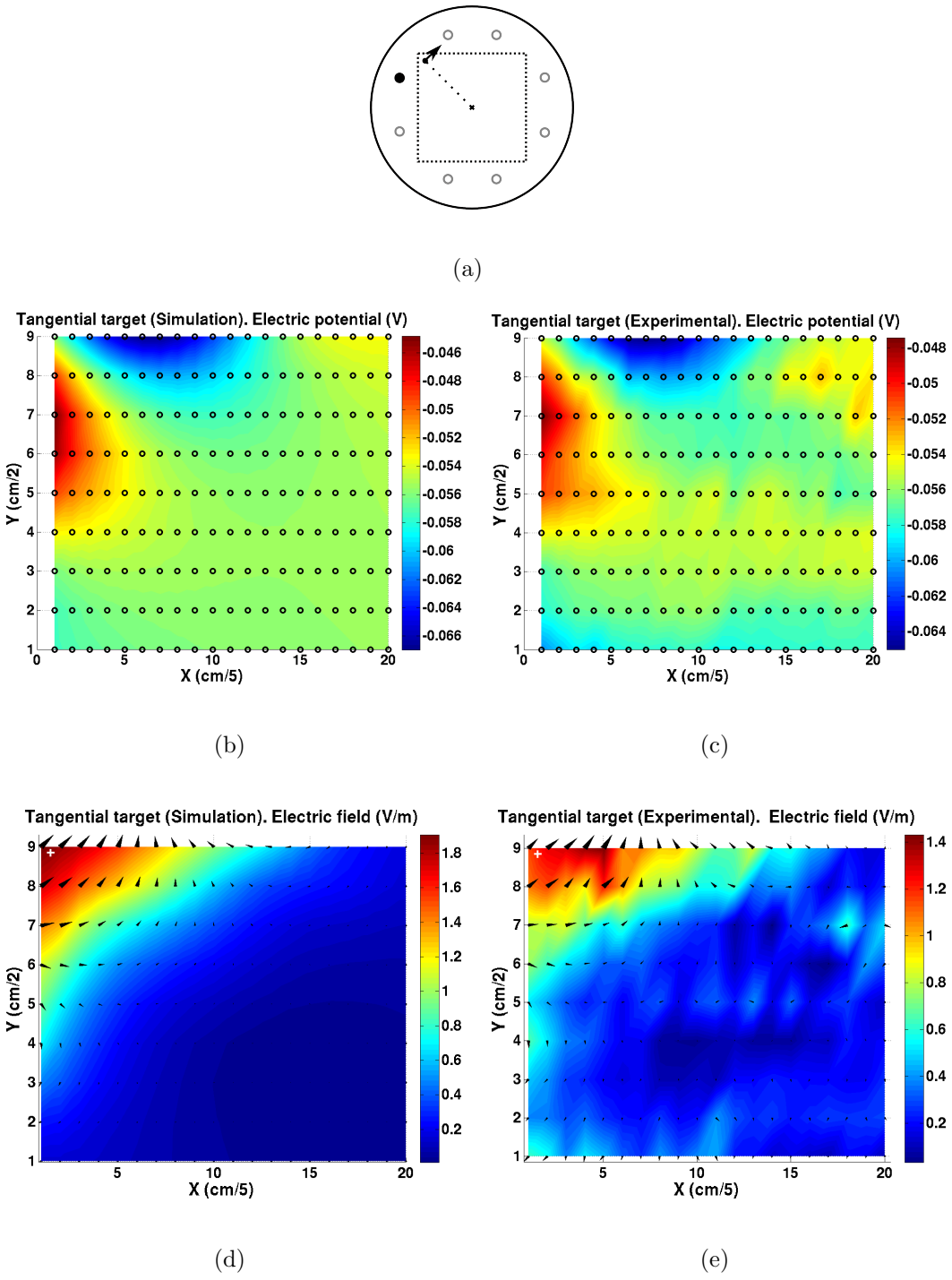

Figure 7.17: Experimental results: measurements of optimized multi-electrode inverse planning of electrical stimulation, tangential case. (a) Petri dish diagram of multi-electrode configuration with available electrodes (gray rings) and ground (black circle). The arrow shows the target for optimization with desired orientation. The dotted-line square is the measurements' area. (b) Simulated and (c) experimental electric potential distribution (black rings are measurement points). (d) Simulation and (e) experimental distribution of the electric field. The white cross in (d) and (e) is the target and black triangles depict the electric field orientation.

7.6 Direction of the electric field

We present the analysis for two electrode configurations in tDCS: the conventional pads and the 4-by-1. Regions of interest (ROIs), depicted in Fig. 7.18a and c (below), were defined at the surface of the cortex. There are two types of ROI: directly under the electrodes *anode* and *cathode* (shown in red) and at the *interelectrode* space (shown in black) covering a radius r_{roi} at the surface of the cortex. For the pads $r_{roi} = 0.025$ m and for the 4-by-1 $r_{roi} = 0.01$ m. These radii were chosen so that the ROIs covered a representative area in relation to the electrode size.

Histograms showing the presence of the radial and tangential components in the ROIs are depicted in Fig. 7.18b and d. The x-axis of the histograms stands for the quotient $E_c/||\vec{E}||$, where E_c is the magnitude of the radial or tangential component and $||\vec{E}||$ is the norm of the electric field. The quotient therefore indicates the strength of each component in relation to the norm. The y-axis shows the percentage of elements at the ROI with a given quotient. On each histogram, we show the T/R relation, i.e. the average tangential to radial component ratio. This ratio is a landmark for component prominence at the ROIs.

Observing the histograms for the conventional pads we note that the tangential component is prominent under the electrodes at similar rates and at the interelectrode region even more noticeably (T/R = 11.74), when the current travels between anode and cathode. The radial component is stronger under the cathode when the current is leaving the brain (Fig. 7.18b). In the case of the 4-by-1 configuration, fields are also predominantly tangential; however, even stronger at the interelectrode regions than in the conventional pads, as shown by the T/R ratio. This can be explained by the proximity between electrodes, which is higher in the 4-by-1 configuration, causing the current flow to be more superficial (on the cerebrospinal fluid), affecting the gyral crowns of the cortical sheet. Under the anode we observe less tangential fields than under the cathodes (Fig. 7.18d).

Surprisingly, and contrasting the common understanding that fields are radial under the electrodes [107], for both electrode configurations, tangential fields are dominant in all ROIs. This is due to the complex folding of the cortical sheet. However, radial fields are present at low and high field intensities in contrast to the tangential, which appear more isolated at high field intensities.

To investigate the directionality of the induced electric field entering or leaving the cortex, i.e. the amount of current flowing inward (depolarizing effect) or flowing

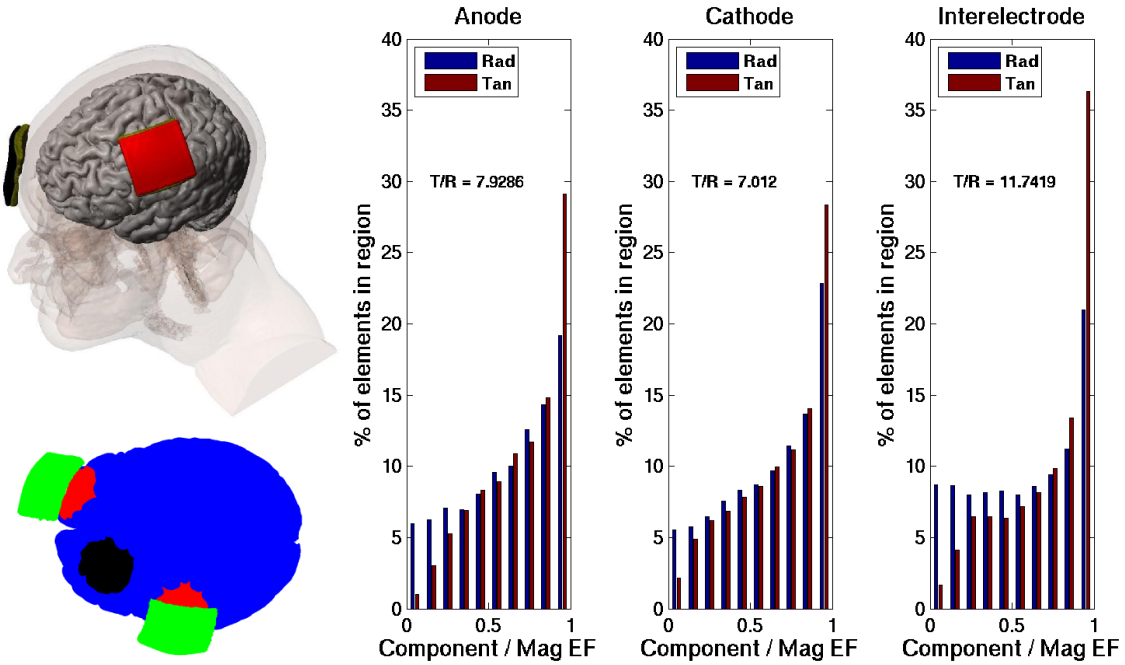

(a) (b)

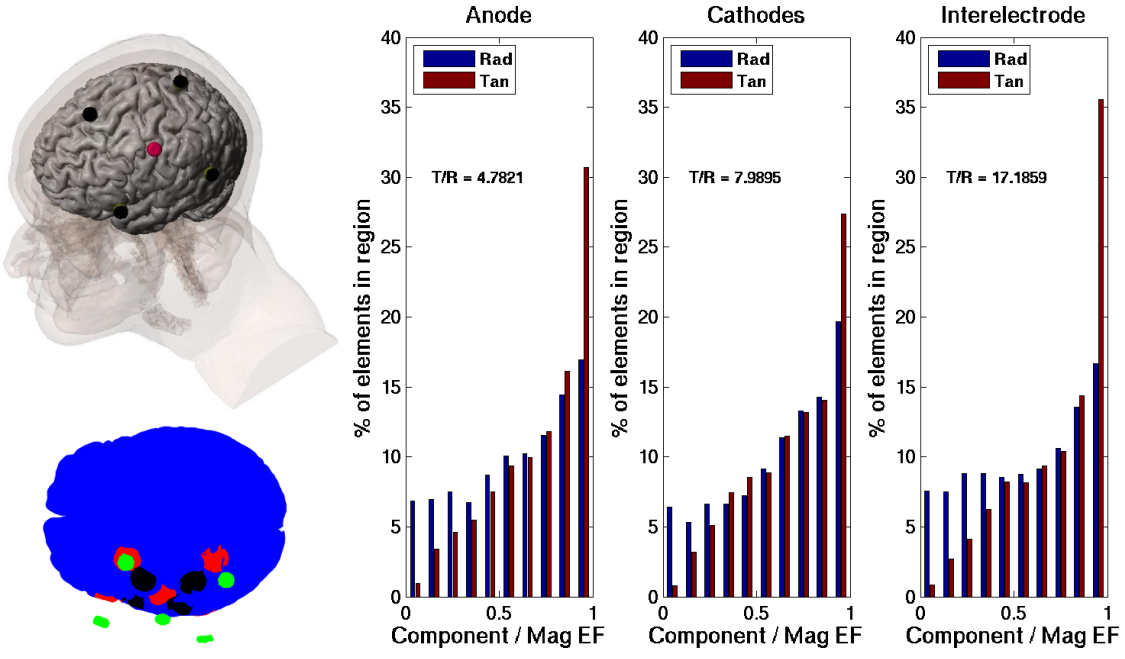

(c) (d)

Figure 7.18: Direction of induced electric field. (a) and (c) show the conventional and 4-by-1 montages, a top view of the brain (blue) with electrodes (green) and ROIs: under electrodes (red), interelectrode (black). (b) and (d) are histograms of radial and tangential components in ROIs in relation to the electric field norm (Mag EF). T/R is the ratio of the average tangential to radial component at the ROI.

outward (hyperpolarizing effect), we show different plots measuring these effects. Fig. 7.19a illustrates the projection of the electric field onto the normals in the cortex. We note the mixed polarization, with current flowing in one side of the walls of the gyri (red in the plot) and flowing out on the walls of the other side of the gyri (blue in the plots).

For analyzing the directionality in different subregions across the cortex, we obtained the net electric field projection onto the normals for 11 regions of interest (ROIs) shown in Fig. 7.19b, namely $\sum_{j=1}^{J} \vec{E} \cdot \vec{n}$, where $j = 1, ..., J$, are the finite elements in the cortex belonging to the ROIs. The ROIs are spheres with 3 cm diameter (depicted in red) centered directly below the corresponding position of the EEG 10/20 configuration.

Topographic plots of the cortex, using the regions of interest from Fig. 7.19b are illustrated. Fig. 7.19c shows the net directionality in the regions of interest. Since the operation is the dot product between the electric field vector with the normals to the surface (pointing inwards), we observe that the net effect of stimulation (two frontal electrodes and two contralateral returns at the mastoids) is that the current direction is predominantly inwards, decreasing gradually as approaching the return electrodes, where the net direction is slightly outwards. Fig. 7.19d illustrates the former point showing the normalized count of elements showing inward current in the regions of interest. We note how prominent this effect is, with most of the cortex showing at least a rate of 60% of elements presenting inward flow, except on the return electrodes at the mastoids, where the rate is nearly 40% and the net directionality is outwards.

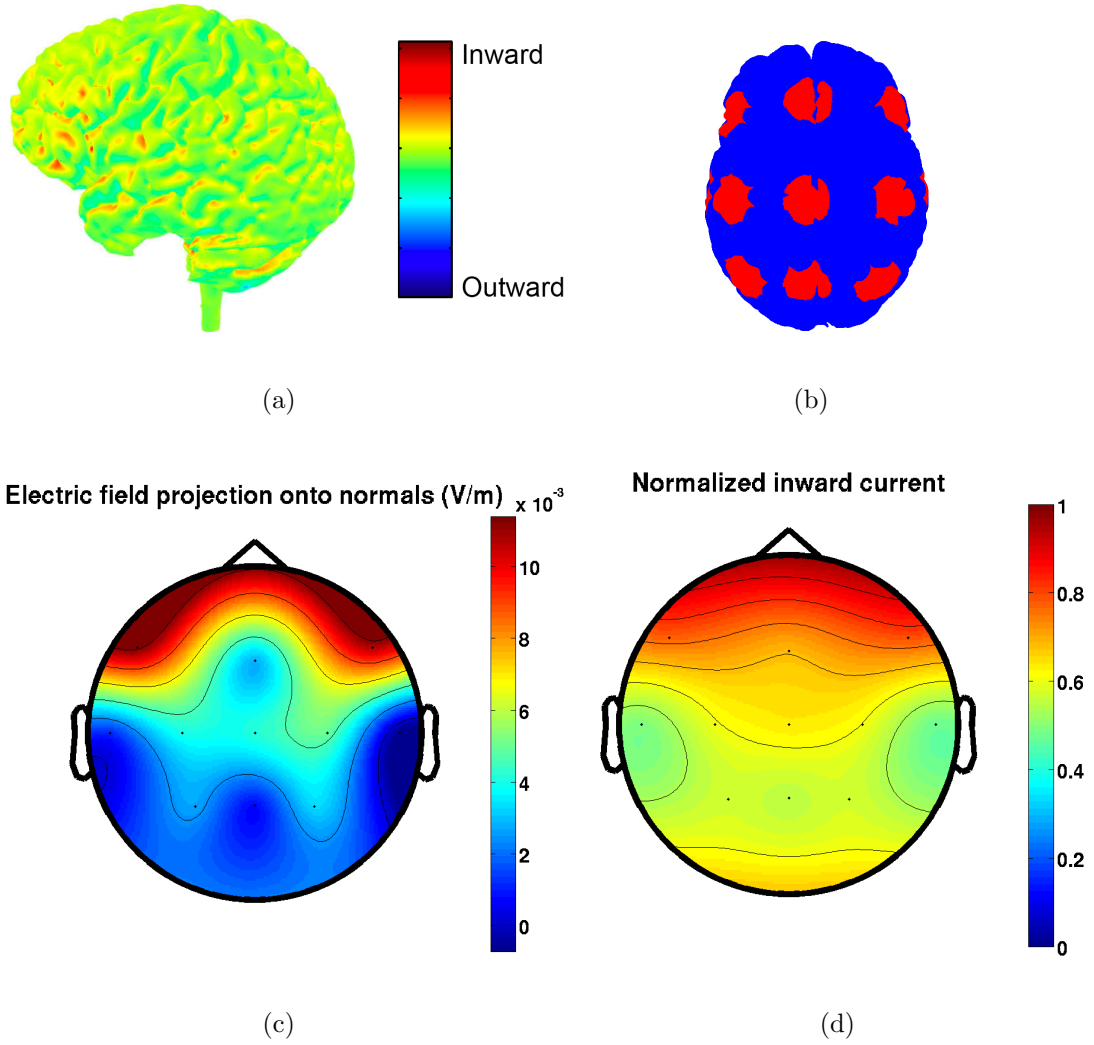

Figure 7.19: Directionality of normal electric field in the cortex. (a) Plot of the cortex showing the magnitude of the electric field with inward or outward direction. (b) Top view of the brain (blue) showing the regions of interest (red) for analyzing the net directionality. Topographic plots of (c) net directionality of electric field in cortex (positive is inwards) and (d) percentage of elements with inward current at regions of interest.

7.7 Anisotropic conductivity

We obtained a diffusion tensor scan from the same subject for which we built the realistic model defined in Section 5.3.2. The DTI sequence had a 2 x 2 x 2 mm resolution, 32 directions and b = 2000 s/m^2 (b-values determine the gradient strength and pulse duration). The measurement was performed with the scanner Philips

Achieva 3 T, at the Neuroradiology UKSH Lübeck. The preprocess of the DTI data for obtaining the diffusion's eigenvectors and eigenvalues and then registering them to the T1 data is shown in Fig. 7.20. As we can see, the registration fits the T1 data satisfactorily. The inset in the axial plane (Fig. 7.20, below) shows the direction of the white matter fibers at the corpus callosum. For the direct mapping we used the scaling factor $s = 0.736\ \frac{S \cdot sec}{mm^3}$ proposed by [149]. For the volume constrained, we calculated the fitted s_{vc} factor so that the geometric mean of the conductivity eigenvalues was in accordance with the literature. We obtained $s_{vc} = 0.253\ \frac{S \cdot sec}{mm^3}$, which is in agreement with [169] and [150].

Observing the induced electric field distribution on the surface of the brain for the different anisotropic mapping approaches in relation to the isotropic case (Fig. 7.21), we note clear differences in magnitude and distribution of the field. The direct mapping approach, due to its higher conductivity values, shows a maximum of nearly half of the maximum in the isotropic case. In the volume normalized and volume constrained mappings, the plots show the maxima are ca. 30% and 40% higher than the isotropic conductivity respectively.

To analyze the effect of anisotropic conductivity modeling, in Fig. 7.22 we illustrate difference histograms between the isotropic and three anisotropic mappings, i.e. direct mapping [148], volume normalized [150] and volume constrained [152]. The histograms show the $Isotropic - Anisotropic_{DM/VN/VC}$ magnitude of the induced electric field norm for white matter and gray matter. A negative difference means that the anisotropic conductivity shows higher electric field magnitudes, whereas a positive one indicates the opposite case. These plots express the extent of the influence of anisotropy (histograms' horizontal axis) in both tissue types. As reference, the maximum induced electric field for the isotropic conductivity was 0.98 V/m, for the direct mapping 0.492 V/m, for the volume normalized 1.4 V/m, and for the volume constrained 1.3 V/m.

The direct mapping approach is known to generate high and unrealistic conductivity values [169], [151]. Our results agree with this finding, observing the histograms in Fig. 7.22a,b we note that the difference in both tissue types for the direct mapping is positive, indicating that the high conductivity values caused by the scaling factor s ($0.736\ \frac{S \cdot sec}{mm^3}$) result in lower electric field magnitudes. Interestingly, we see that this effect is even stronger in the white matter, where at least 30% of the elements have a difference higher than 0.2 V/m.

The volume normalized approach Fig. 7.22c,d indicates the opposite trend than

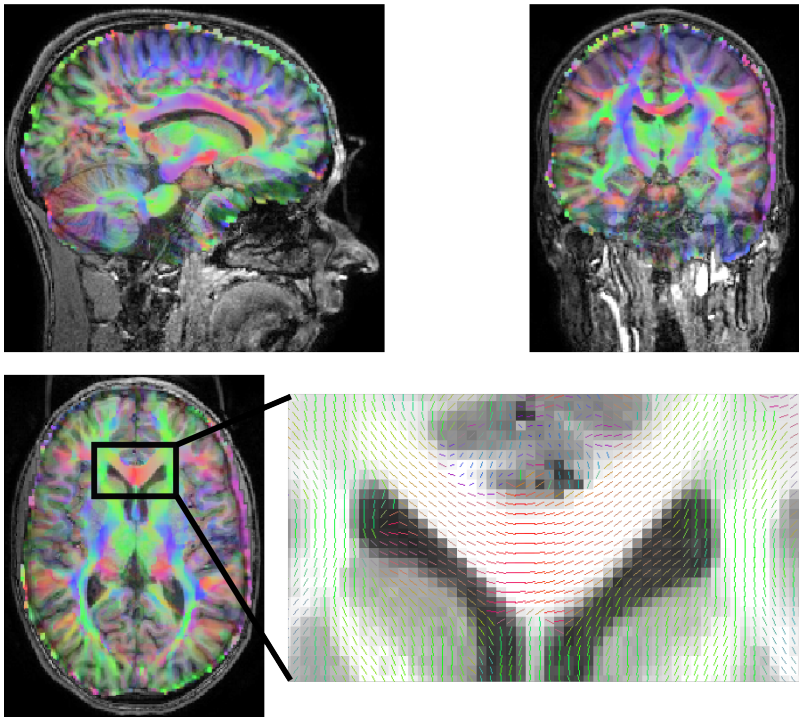

Figure 7.20: First eigenvector from DTI data overlaid onto T1 volume after registration. Saggital, coronal and axial slices depicting the fitted DTI data. The inset in the axial slice depicts the detail in fiber directionality at the corpus callosum region. The color coding indicates the diffusion preference along the following orientations: red (medial-lateral), blue (superior-inferior) and green (anterior-posterior).

the direct mapping. We note that nearly 75% of the elements in gray matter has a difference of less than 0.02 V/m. This means gray matter is not as strongly affected by anisotropy. In contrast, changes in white matter are more apparent, where we observe a normal distribution centered at -0.033 V/m, whereas the center value for the gray matter difference distribution is located at -0.025 V/m.

In the volume constrained approach Fig. 7.22e,f we observe a similar behavior to the volume normalized. However, changes in white matter are more noticeable. The difference distribution has an even higher center value located at -0.04 V/m, confirming that anisotropy increases white matter's electric field magnitudes in our model. In gray matter, we also observe a tendency in field magnitude increase. However, as in volume normalized, these effect is not as strong as in white matter, noting a center value of -0.035 V/m.

In Fig. 7.23 we illustrate axial slices of the conductivity mapping approaches. In general, we note that the electric field distribution is substantially changed mainly in the white matter, where we appreciate patterns of increased electric field magnitude caused by the difference in conductivity along the white matter fibers. The

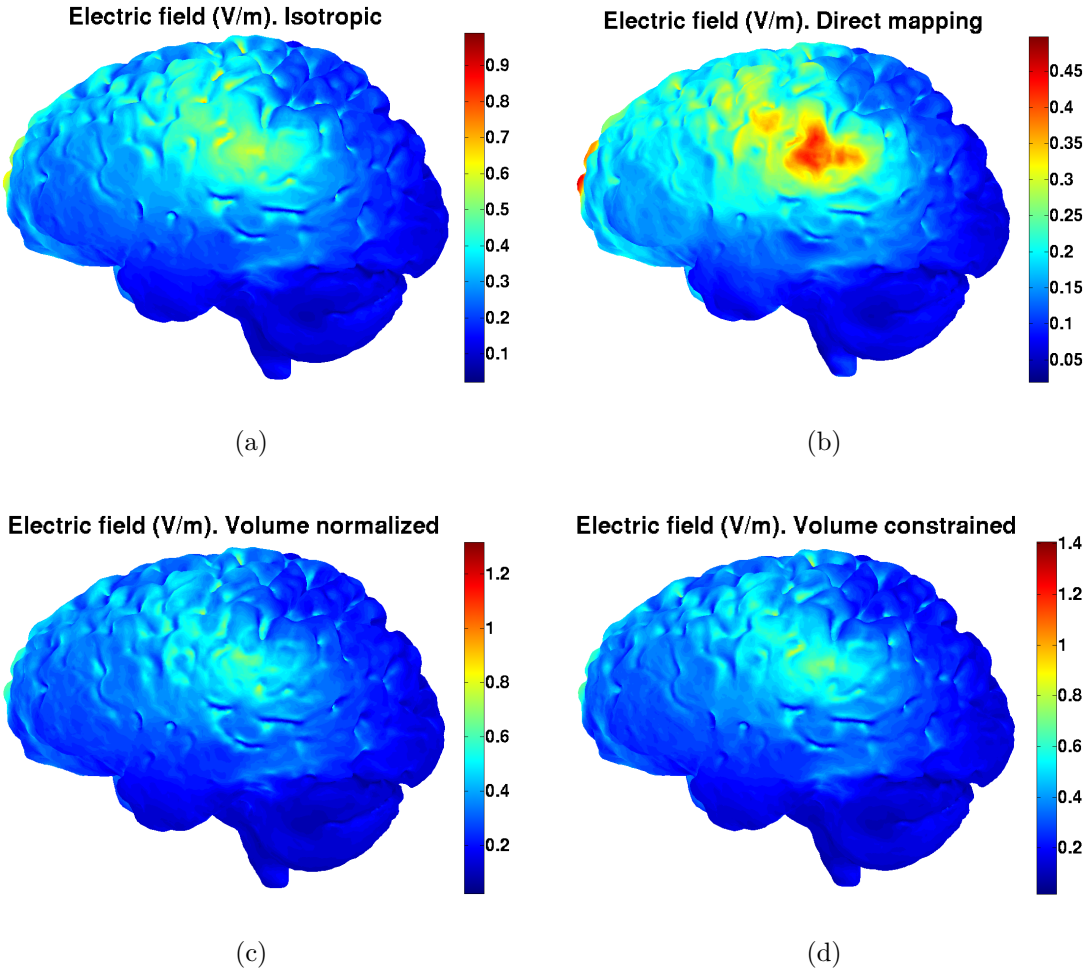

Figure 7.21: Induced electric field in cortex by conventional tDCS in realistic head model with anisotropic conductivity mappings. (a) Isotropic case, (b) direct mapping, (c) volume normalized and (d) volume constrained approaches. Note the difference in scales.

orientation of the electric field is also depicted, which allows to see the anisotropy induced difference in current flow.

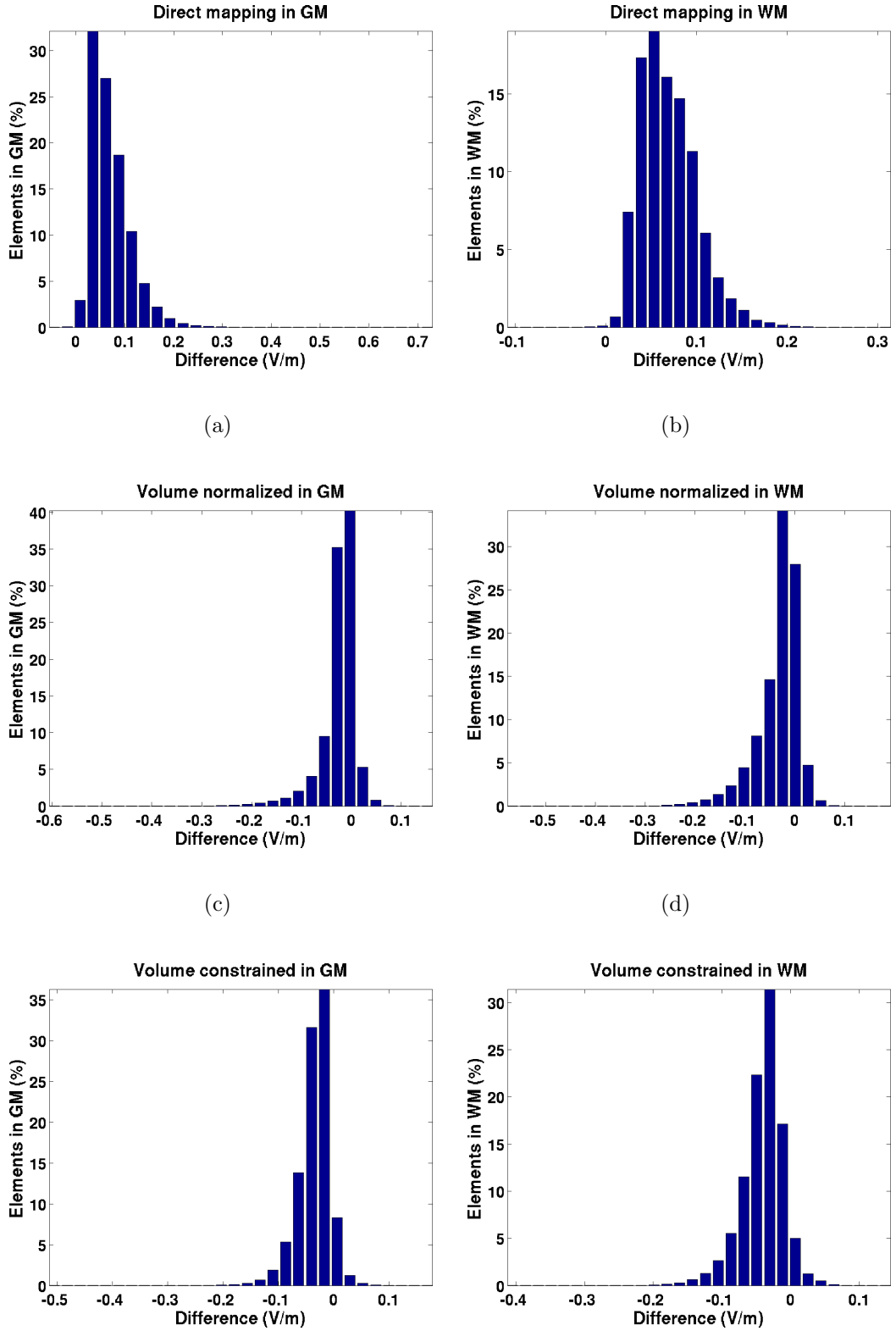

Figure 7.22: Difference histrograms between isotropic and anisotropic conductivity for gray matter (GM) and white matter (WM) in tDCS using: (a),(b) direct mapping, (c),(d) volume normalized and (e),(f) volume constrained mappings.

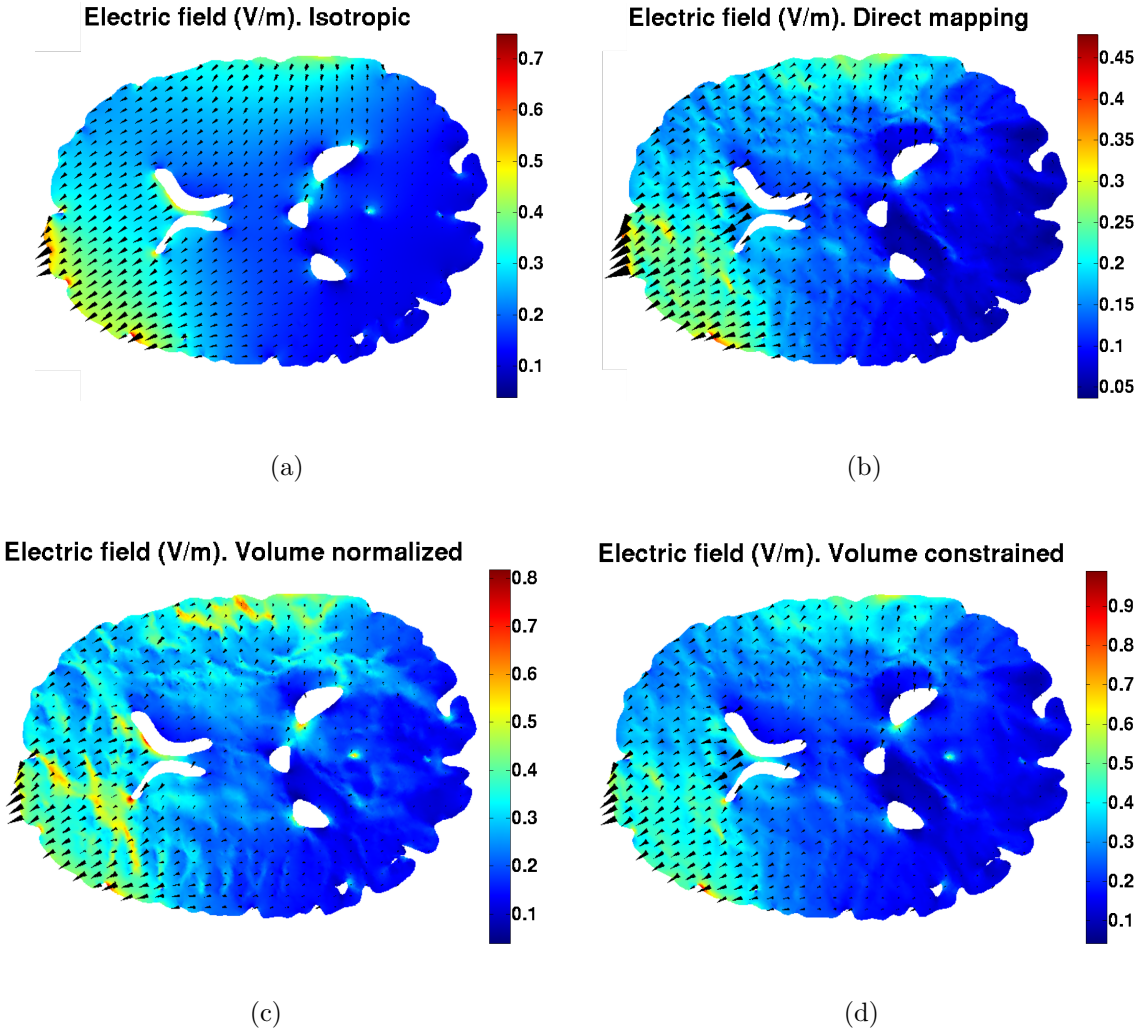

Figure 7.23: Axial slices for anisotropic conductivity mappings. (a) Isotropic, (b) direct mapping, (c) volume normalized and (d) volume constrained approaches. The black triangles depict the direction of the current flow.

7.8 Animal studies

7.8.1 Forward planning for TMS in the rat

The study's objective was to determine the effect of rTMS on neurotransmitter outflow in the nucleus accumbens in the awake rat. For achieving this, our realistic model allowed to predict the outcome of stimulation, showing the structures affected by stimulation and therefore the link with its physiological function.

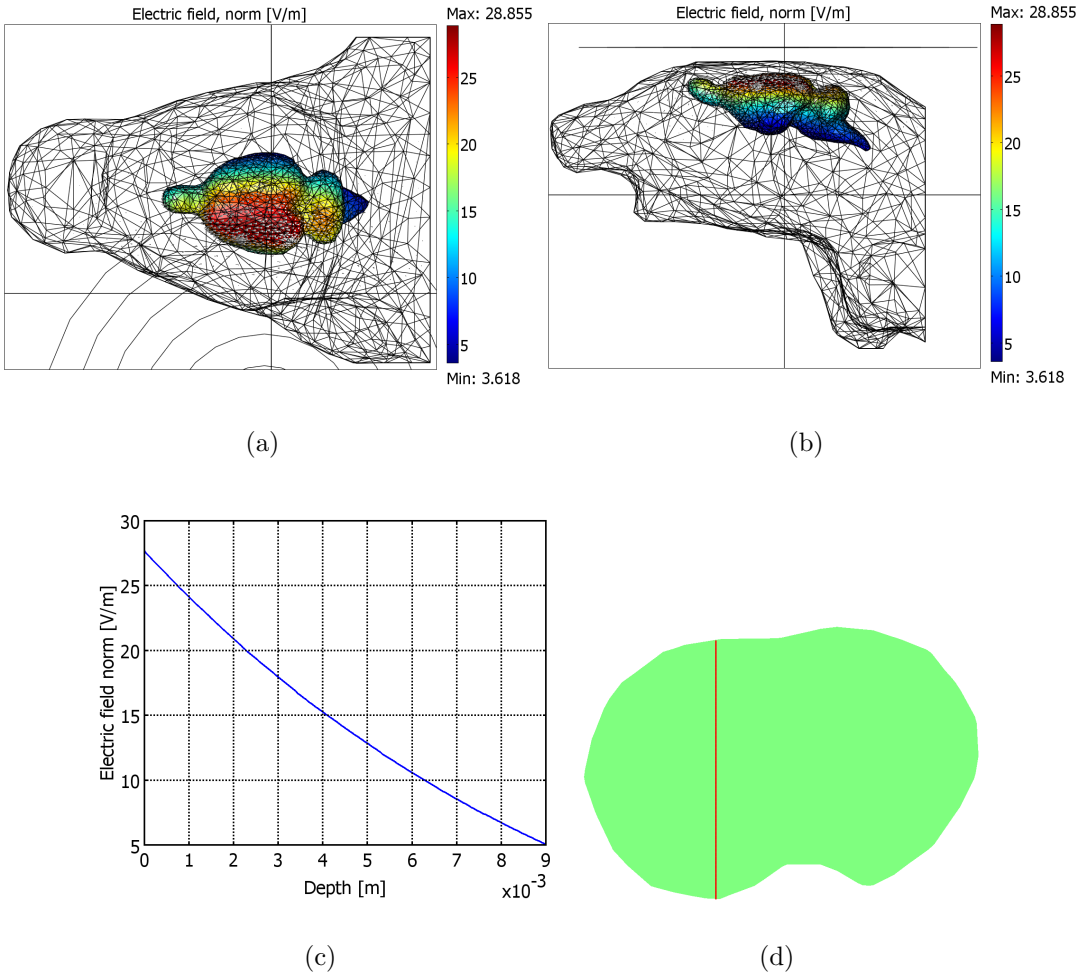

Figure 7.24: Animal study: forward planning of TMS in the rat through FE simulations of the electric field distribution in the rat brain model in a typical rTMS stimulation scenario using a circular MCF75 TMS coil. (a) An electric field with 28.8 V/m at maximum influenced the entire cortex. (b) The induced electric field magnitude decays with depth in the dorsaleventral direction. (c) The profile line for the induced electric field in V/m in the dorsal-ventral direction from the surface of the cortex (0 mm) to the bottom of the brain (8.5 mm) on the anterior-posterior trajectory of the nucleus accumbens shell region at +0.17 mm relative to bregma. (d) Coronal slice at bregma showing the profile line (red) for (c).

The resulting induced electric field distribution in the realistic rat model is shown in Fig. 7.24. Stimulation was not confined to prefrontal cortex, but was observed widely spread in the left hemisphere of the cortex, the side with more proximity to the coil (Fig. 7.24a). The electric field magnitude had at a maximum magnitude of nearly 29 V/m in the cortex.

We show the induced electric field decays rapidly with depth (Fig. 7.24b,c). This decay was obtained in a trajectory from the cortex at 0 mm to 8.5 mm dorsal-ventral, at the anterior-posterior location of the nucleus accumbens shell region and +2 mm lateral (Fig. 7.24d).

The induced electric field profile decays exponentially as the distance from the coil in ventral direction increases. In the depth of nucleus accumbens at 7.5 mm, the electric field strength is 27% of the electric field strength in the cortex [124]. Therefore, it is unlikely that the observed effects in neurotransmitter outflow as a result of rTMS were caused by direct stimulation of the nucleus accumbens. This is in contrast to the findings of [6], [5], which assume direct stimulation.

7.8.2 Forward planning for tDCS in the rat

The study's objective was to investigate memory consolidation after applying slow-oscillating tDCS to rats *in vivo*. The induced electric field distribution for the four electrode configuration defined in Section 5.4.2 is depicted in Fig. 7.25. The aim of the stimulation was to target the frontal lobe contralaterally in a focused way. The forward planning involved the insertion of the electrodes at different depths starting at the surface of the skull and applying different current intensities. We have established from the analysis in Section 7.3, that the electrode implantation has a strong influence in the focality of stimulation, which means that if we require more focality, the electrodes need to be implanted deeper.

When performing the electrode implantation on the rat skull, special care must be taken not to damage the brain. When electrodes are implanted at depths beyond the dura mater, they push the cortex and can create localized lesions; therefore, this is why the insertion depth was chosen to be halfway through the skull, which still produces two focal hotspots of electric field in both hemispheres of the rat's prefrontal lobe (Fig. 7.25a). The electric field magnitudes also stay within the desired range (subthreshold, <1 V/m). The profile in depth can be appreciated in the coronal slice plot at the height of the anodes (Fig. 7.25b), where we can see that

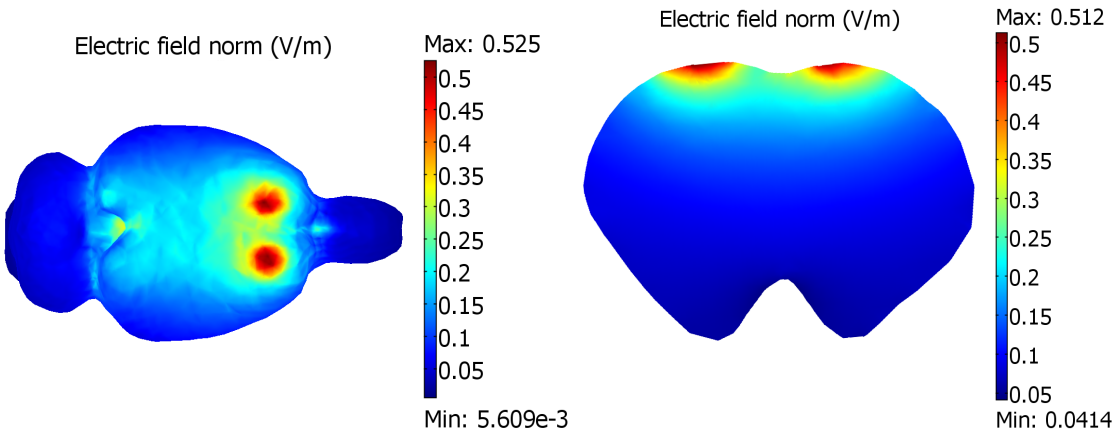

(a) (b)

Figure 7.25: Animal study: forward planning of tDCS in the rat for memory consolidation study. (a) Top view of the induced electric field at surface of the rat brain model by the four-electrode configuration. (b) Coronal slice at the height of the anodes, i.e. +2.5 mm antero-posterior.

the stimulation is confined mostly at the cortex.

This study showed that applying slow-oscillating tDCS to rats *in vivo* enhanced hippocampus dependent memory, replicating the findings shown in humans [46],[47]. With the help of the realistic model of the rat, the results indicate that slow-oscillating tDCS, applied focally to the rat brain cortex, boosted sleep slow oscillations. Although the stimulation affected the motor cortex, it is unlikely that the memory formation was motor-related because of the nature of the task. However, the consolidation is presumably mediated by cortical interactions [125].

Chapter 8

Discussion

8.1 Conductive shield plate on simplified rat model

TMS in the rat has proved to have great potential for studying the brain. Microdialysis is a powerful tool to use in conjunction with TMS in rat experiments, where direct neurochemical measurements can be obtained in specific anatomic structures. In [6] and [5], the authors show that TMS on the nucleus accumbens has a modulatory effect on dopamine release, which in turn can alter the reward circuitry and have major implications for depression or abstinence syndrome. Similar studies could benefit from focalized TMS, as it could provide the means for targeting specific anatomies and their functions.

It is important to consider that rat experiments must undergo significant changes before being transferred to humans, and that targets in the deep human brain are not reachable through conventional TMS. The development of deep brain TMS [94],[170] with the so-called "H-coil" for the treatment of depression has shown positive clinical results [171]. However, like we have stated previously in this work (Section 6.2.2), cortical structures will always be more affected than deep ones (also due to the exponential decay of the electric field in tissue [51]). In order to translate the effects observed in TMS animal experiments it is of vital importance to incorporate accurate modeling of the induced fields. Even if animal experiments cannot be directly translated to the human, they can still reveal crucial mechanisms of brain function [91],[6],[5].

For the shield plate to be integrated in a real TMS environment, one would need to consider the temperature and mechanical changes induced by the shield plate.

Further refinements to the model presented in this section have been included in subsequent work. A next step at this stage was to validate the presented simulations with real measurements of the induced electric field by TMS using the shield plate, which is discussed in the next section of this chapter.

The presented results show that TMS with the conductive shield plate effectively improves the focalization of the induced electric field. A clear dependence between the higher focalization and attenuation of the induced electric field was also observed. The obtained results are encouraging and can therefore lead to the improvement of the state-of-the-art implementation of rat experiments with TMS.

8.2 Experimental results: conductive shield plate

As the results point out, focality is increased more than tenfold in the circular coil and nearly threefold in the figure-of-eight. We observed in our measurements that coil asymmetries do have an influence on the induced electric field (as in the case of the circular coil in Fig. 7.3). The figure-of-eight coil showed less attenuation of the electric field with the plate in comparison to the circular coil. This can be explained by the current flow in the coil geometries: the opening window in the shield plate is exactly placed at the hotspot produced by the figure-of-eight-coil, whereas in the circular coil, due to its slight asymmetry (also noticeable in the measurements, Fig. 7.3), the maximum electric field was not exactly aligned with the window in the shield plate.

The measurements of the two most common coil geometries using the conductive shield plate gave us insight into several aspects of coil construction, if the shield plate were to be integrated inside the coil casing. An aspect we observed during the measurements is that the usual clicking of the TMS coil is enhanced due to the mechanical stress of the conductive shield plate (caused by the coil's magnetic field). We were able to decrease this effect by placing a thin layer of damping material. In production, one would have to consider a casing able to resist such stress in the long term. The conductive plate also influences the temperature of the coil, raising much faster than without it. Just as some of the available coils in the market, a coil with conductive shield plate would have to include an active cooling system to make sure the temperature stays within appropriate values and is operable during treatment. Another relevant issue is the attenuation of the field caused by the shield plate, in accordance with our previous simulations on the simplified rat model (Section

7.1). This can be solved by increasing the intensity output on the TMS stimulator. However, one would need to ensure the aforementioned issues, (i.e. clicking of the coil, mechanical force and temperature) are acceptable for such higher ranges.

8.3 tDCS in the rat

Over the last decade tDCS has shown great clinical and experimental potential to modulate neural function non-invasively. As we have pointed out, the rat model has been highly instrumental to develop potential treatments and evaluate the safety of this technique.

We were able to show that electrode insertion depth changes the induced electric field drastically and that using a realistic model to predict the outcome of a given configuration, one can achieve focal stimulation of the rat cortex. In an effort to improve focality, a number of alternatives have been proposed, such as reducing the size of the electrodes while maintaining the current density, increasing the size of the reference electrode (thus reducing its current density), placing an extra-cephalic reference, and using a ring electrode configuration [2],[8].

An issue to investigate further is the lack of neuronal profile characterization for stimulation, including cytoarchitecture and cortical structure, properties that additionally reveal species specific differences. As a result, studies to determine the biophysics of neurons as well as detailed FE analysis, new electrode designs and configurations [114] should contribute to elucidate the effects of tDCS in the brain. Much of this research requires the animal model, initially to validate, and subsequently to improve the present paradigms. Hence, a systematical approach in experimental protocols and models, is of the utmost importance in predicting the elicited effects of stimulation.

This section of our work presented the FE simulations of tDCS in a realistic three-layer rat head model. We simulated two electrode configurations in three depth scenarios. Realistic modeling of the induced electric field should be taken into account when designing tDCS rat experiments in order to identify the affected brain targets. The analysis with anatomically accurate models is a contribution to the further development of tDCS research in rats, which should facilitate a systematic framework for the pursuit of more ambitious and rational experimental design to study brain function.

8.4 Optimized multi-electrode tDCS

It has been argued that low focality in tDCS for therapeutic cases is irrelevant, where large areas of the cortex are targeted (motor cortex in stroke and dorsolateral prefrontal cortex for depression) [106]. Even though it is not clear whether this idea is true, optimized stimulation does not conflict with it. While the optimization methods portrayed in this work aimed at evaluating the highest attainable focality for the given setups, they also allow targeting wider areas of the brain, as well as more than one target (which can be the case in stroke therapy).

Optimized tDCS gives the clinician the freedom to choose and gain control over stimulation, namely, knowing the area of the brain being stimulated as well as the intensity and orientation of the electric field. This should translate into a better understanding of the functional and anatomical relationships. In humans, it has been shown that as current density increases the effects of tDCS become stronger [101]. This motivates achieving higher intensities within safety limits, something optimized stimulation allows in comparison to the conventional and intuitive 4-by-1 configurations. The intuitive 4-by-1 configuration introduced in [8], provides a substantial focality improvement against the conventional pads (Fig. 7.8) for low intensities.

The subset selection approaches allow customizable optimized stimulation, making it a suitable choice for any multi-electrode stimulation system. Our SOS algorithm for sparse representation proved to have similar or even better performance than the l_1-norm approach using normally half (or less) electrodes in the radial case, and using 2-3 electrodes less in the tangential case. The OMP scheme, while showing worse focality performance than SOS, still does better than the Top-k algorithm and has the advantage of being computationally lighter.

When selecting a target and placing the electrodes, using the EEG 10/10 configuration has the advantage of providing anatomical landmarks; whereas the electrode patch array would require a procedure based on a few measurements of the head, similarly to the way the TMS coil is placed in commercial systems. The EEG 10/10 configuration should ideally be used for radial targets directly under the electrodes or tangential targets in between electrodes. The electrode patch array on the other hand, can be used at any location in the cortex and for any given field orientation. A drawback from the patch schemes is the computational cost associated with having to generate a new lead matrix $\mathbf{A}$ with the FEM simulations for the arbitrary position on the scalp.

The focality maps presented as topographic plots of the cortex showed a general picture of the presented optimization schemes. We note the influence of head topology in the achievable focality. In radial targeting, for the majority of our methods, we observe the influence of skull thickness and cerebrospinal fluid presence. Most of the methods exhibit worse performance in the parietal lobe, where skull is thick and cerebrospinal fluid abundant, than on the temporal lobes, where skull is thin and cerebrospinal fluid more moderately present.

The optimization schemes presented in this work aim at targeting structures at the surface of the brain. Targeting deeper structures under these schemes would lead to a more diffuse electric field distribution with maxima at the surface, at the boundaries where the conductivity changes. This problem has been studied in [67], where the authors prove that it is not possible to produce a local maximum of electric field strength inside the brain using any superposition of external current sources. One could however use the clustering-effect to reach deeper regions in the brain, i.e. targeting deeper structures where the cerebrospinal fluid is present. Unfortunately, this does not hinder the presence of electric field hotspots on cortical regions.

We are aware that other electrode configurations could lead to similar results, if for example, the position of the electrodes were to be integrated into the optimization, allowing them to move freely to any position in the scalp. This idea was explored in [172]; however, the authors concluded the procedure was too time consuming. We consider this worth investigating, however beyond the scope of this work. On the one hand, an advantage of the linearly-constrained-minimum-variance optimization approach presented in [12] is the absence of misalignment. On the other hand, using least-squares based optimization allows us to achieve greater field intensities with a reasonable misalignment: below 12 degrees in radial fields (except 4-by-1 and Top-k) and below 15 degrees in tangential fields for all (except patch and CLS approaches).

In the realm of greedy algorithms, such as our SOS scheme, one could integrate the concept of floating-selection [173], in order to check the possibility of dropping/replacing elements during the selection process. This backtracking capability can increase the computation significantly, which is already the heaviest among the presented schemes.

A useful feature of multi-electrode optimized electrical stimulation is the ability to target multiple anatomical structures simultaneously. This is of particular interest in treatments such as rehabilitation after stroke, where both hemispheres are stimulated at once. Using the conventional pads, one cannot control the orientation of the

electric field, therefore, on one hemisphere there will be current going in, whereas on the other hemisphere current will be mostly going out. Using optimized tDCS one can choose or combine directions of the electric field at the different targets for a given desired clinical outcome.

The finite element model employed in this work aims to realistically simulate human anatomy. However, further refinements remain to be integrated in the future. Particularly, anisotropic properties of tissue, later analyzed in this work, which have shown to influence the direction of current flow primarily in white matter [169].

The elicited electric field distribution in the brain by TMS has been shown in FEM studies [11],[169]. Interestingly, the simulations in those studies show the electric field maxima at the crowns of the gyri, displaying no clustering-effect at the bottom of the sulci. In TMS the direction of the induced current can be modified by changing the orientation of the coil in relation to the gyri. However, the induced current is predominantly tangential to the surface of the brain. The electric field distributions shown in Fig. 7.8 suggest that the focality of optimized tDCS is comparable to TMS. This is of particular importance because it should open a range of possibilities in tDCS experiments.

tDCS clinical and simulation studies have shown inter-individual variability in response and induced electric field intensities [106],[8],[9]. Patient-specific modeling and optimization techniques should prove useful for studying this in order to deliver stimulation in the most systematic way possible.

In this work we introduced new schemes for optimized multi-electrode tDCS which showed substantial improvement against the existing paradigms. Our approaches integrate the concern of hardware complexity and yield promising results using a reduced number of stimulating channels. In the last two decades transcranial stimulation has shown a powerful potential to study the brain and treat neurological conditions. Nevertheless, we consider of paramount importance to develop techniques which allow its rational use and contribute to the better understanding of its effects.

8.5 Experimental results: inverse planning *in vitro*

The two cases showcasing the inverse problem in the petri dish validate the applicability of the optimization of the electrode currents presented in this work. We

were able to successfully assign a target intensity and field orientation *a priori* in an experimental setup. It is important to mention that since we were dealing with more electrodes in comparison to the superposition experiments (Section 4.1), made the measurements more susceptible to error. Each active electrode current is configured by hand and subject to how precise the value in the current source output can be manually set. Although the current output was measured and adjusted observing the signals on the oscilloscope, there is still an error margin. This is the reason we attribute the variations between simulation and measurements, along with present inhomogeneities in the saline solution (specially in the tangential case). Nevertheless, the electric field distributions, magnitude and misalignment showed a reasonable agreement with the simulations (Figs. 7.16 and 7.17).

The applied currents were in the order of μA and are in the lower range of the Isostim stimulator (World Precision Instruments Inc. Sarasota, FL, USA). We chose these low magnitudes in order to maintain an acceptable dynamic range for the g.USBamp amplifier (g.tec medical engineering GmbH, Schiedlberg, Austria).

8.6 Direction of the electric field in tDCS

The somatic doctrine assumes the radial current flow under the stimulating electrodes and that the depolarization and hyperpolarization occur at the soma [107]. The results we present, in addition to a body of evidence suggesting a more complex mechanism of activation occurring at the synaptic afferents rather than the pyramidal somas [104], [140], [108]. Our detailed model of the convoluted cortical sheet has shed insight into the direction in which the electric field affects pyramidal neurons at the cortex. We have quantitatively shown that contrary to the somatic doctrine, the stimulation under the electrodes is predominantly tangential. Even though, radial fields are also present. This means that as the electric current goes through the gyral walls, it does not necessarily polarize neurons with fields either parallel or orthogonal to the walls, but rather a combination of the two, with a heavier tendency to being tangential to the wall. These observations allow us to speculate that the polarization occurs at the synaptic afferents. A finding we have supported with evidence of experiments with rat brain slices *in vitro* [108].

The directionality of the normal electric field in the cortical sheet allows us to quantify whether pyramidal cells are being hyperpolarized or deporalized, given the double polarization that occurs at the gyri [141]. Our results showed that under

the anodes (placed frontally), the electric field's directionality is mostly inwards, having a depolarizing effect. Under the cathodes (placed on mastoids) the effect is opposite, i.e. hyperpolarization. We have used this information to feed a network model replicating the slow-wave oscillations (SWO) 0.5-1 Hz present during human sleep. SWO are a landmark for sleep homeostasis. This is a process that regulates sleep and is thought to be linked to homeostatic plasticity, a mechanism that adjusts average firing rates by altering synaptic strength [174]. With this modeling effort we have been able to show a mechanistic link between transcranial direct current stimulation and accelerated synaptic homeostasis in humans [141].

8.7 Anisotropic conductivity modeling

We presented the results of integrating anisotropic conductivity of the brain into our realistic model. The conductivity tensor, derived from DTI data was successfully fitted to the T1 volume through rigid registration. We performed simulations on three anisotropic conductivity mappings and compared them to the isotropic case.

Our results confirm that anisotropy exerts most of its influence in white matter (see Fig. 7.23). Differences in the conductivity mappings are also apparent. The direct mapping, using the linear scaling factor $s = 0.736\ \frac{S \cdot sec}{mm^3}$ proposed empirically in [148] gives rise to unrealistically high conductivity values. Constraining the factor to the geometric mean of the diffusions' eigenvalues across all voxels forces the conductivity tensors to stay within realistic values. For our model $s_{vc} = 0.253\ \frac{S \cdot sec}{mm^3}$, which agreed with previous studies [169], [152]. The volume normalized mapping is similarly conservative, however constraining the volume of each voxel to that of the isotropic ellipse. The fitting of the conductivity tensors makes the two constrained mappings better suited for anisotropic analysis.

In accordance to the results reported in a similar TMS modeling study [169], we observed that integrating anisotropy increases the average electric field magnitude in white matter. In contrast to the findings of [169], our results show that gray matter also increased its average magnitude, but in a lesser proportion. That is the reason why we observe electric field maxima with greater magnitude at the gray matter in the two constrained conductivity mappings (Fig. 7.21). We can expect an increased effect on gray matter in tDCS taking into account that the induced currents by TMS are mostly tangential to the surface of the brain [51], i.e. they enter orthogonally in the sulcal walls but not so in the gyral crowns. In tDCS, induced

currents have significant contribution of both components: radial and tangential (as analyzed in the previous section of this work). Even though our findings indicate that the tDCS induced currents are dominantly tangential, radial fields are also present, and have a more prevalent effect on the gyral crowns and bottom of the sulci. This is due to the fact that in the conventional tDCS montage (used in this analysis) the current actually travels through the brain, as opposed to TMS, where the induced fields are mostly on the brain surface. This is why tDCS modeling studies report the presence of the "clustering effect" [8], [9], i.e. hotspots at the bottom of the sulci, in contrast to TMS studies, where this effect is not observed [11],[169],[130].

Anisotropic conductivity changes the distribution of the electric field (see Fig. 7.23) mainly along the white matter fibers, in the direction of the current, where a magnitude increase is noticeable. Current direction is in general less homogeneous throughout the brain in the anisotropic case, specifically at prominent white matter fibers close to the electrodes, where abrupt conductivity changes cause charge accumulation.

Our results are based on the hypothesis that the conductivity of brain tissue, i.e. the ionic mobility responsible for it, and the mobility of water molecules share the same eigenvectors [149], [169], [150], [152]. This assumption is reasonable and has been supported by experimental data shown in [175]. We consider that integrating anisotropy into the modeling further refines the predictions mainly in white matter, albeit the computational complexity (ca. triple the run time) added to the model and the extra preprocessing steps required for the DTI data.

8.8 Animal studies

8.8.1 TMS in the rat

Our realistic simulations of the induced electric field showed that direct stimulation of the nucleus accumbens was unlikely since the electric field decayed steeply with depth in an exponential fashion. This finding had not been indicated in previous studies investigating the nucleus accumbens shell with rTMS [5],[6],[176]. The simulation using a homogeneous model of the rat scalp and brain provided a reasonably realistic representation of the stimulation scenario, given that most of the charge

accumulation during TMS occurs at the scalp-air interface, adequately considered in this work.

As it has been shown that the radial component induced by rTMS is not significant, the model should not be notably altered by omitting cerebrospinal fluid layer [60]. We can therefore assume that neurochemical changes found in the nucleus accumbens may arise from indirect effects of cortical stimulation [124], and suggest that the situation in our animal model may be similar to rTMS in humans [177], [178]. Our finding, that extracellular GABA outflow was not modulated by rTMS supports the hypothesis of a remote effect of rTMS on nucleus accumbens neurons, since they are mostly GABAergic [179].

The implication of modulating monoamine outflow in the nucleus accumbens shell region is that it may re-establish normal function in various neuropsychiatric conditions such as drug-withdrawal, obsessive compulsive disorder, depression and chronic pain. This is the first rat TMS study where such detailed simulations are taken into account to provide insight about the effects of stimulation.

8.8.2 tDCS in the rat

The forward planning of the electrode configuration for slow-oscillating tDCS in the rat played a crucial role in the interpretation of the cognitive outcome from the memory consolidation task. Our detailed model allowed to assert that the stimulation foci were located at the prefrontal cortex, the extent in their electric field distribution, their approximate amplitudes, and if these can be comparable to endogenous fields. Before reaching the final electrode configuration, there were previous iterations where the electrodes' location and current magnitude were adjusted in the model to achieve the desired outcome (Fig. 7.25).

We stimulated the prefrontal cortex because it has been shown that the recruitment of neocortical areas such as the medial prefrontal cortex (mPFC) occurs for both remote memory, i.e. events already independent of hippocampus with a delay of more than 10 days; as well as for spatial memory, i.e. hippocampus dependent memories no older than 3 days [180], [181].

The two laterally positioned frontal anodal electrodes did not exert its strongest effects on the mPFC. However, we aimed to enhance and synchronize slow-oscillating activity over a broad area of the prefrontal cortex. Animals were only able to

solve the task if slow-oscillating tDCS was applied, but failed to do so in the sham condition, where no slow-oscillating tDCS was applied [125].

The induced electric field computed with our anatomically accurate FE model (4 electrode configuration with equal surface areas) shows focused effects with highest current densities beneath the anodes. Under the cathodes, the simulations didn't indicate the presence of hotspots (distribution is more spread), which we attribute to two anatomical characteristics of the cerebellum's region: (1) skull thickness is greater and (2) there is higher presence of cerebrospinal fluid. Both of these anatomical characteristics are the opposite in prefrontal regions. The electrode configuration used in our experiments concurs with similar electrode montages used in recent studies [135] which have shown their effectiveness on neuronal entrainment at low field strengths.

Our findings provide further evidence for the usefulness of oscillatory tDCS as a tool to investigate endogenous cortical network activity and its functional relevance for cognitive processes. Furthermore, it could be shown that the findings concerning the effects of slow-oscillating tDCS can be successfully transferred to a rodent model [125], [182].

Chapter 9

Conclusion

9.1 Contributions

Throughout this work, we have presented detailed models and experimental results for achieving a systematic planning and focal transcranial stimulation in its two most applied modalities, i.e TMS and tDCS.

For TMS we used the concept of a conductive shield plate attached to the stimulating coil, as introduced in [92]. The shield plate has a window which allows only a portion of the coil's magnetic field to pass through; therefore constraining the spatial distribution of the induced electric field. As of now, alternatives to improve coil focality have not been tested experimentally [92],[93],[98]. We report the first experimental results showing that the conductive shield plate can substantially improve focality. Furthermore, the attenuation of the induced electric field as the size of the shield's window changes was analyzed in a small animal model. We discussed the practical issues and considerations if the conductive shield is to be integrated in the casing of a TMS coil.

In the case of tDCS, we adopted the multi-electrode optimization approach, where we solved the inverse problem of finding the adequate currents for eliciting a given intensity and orientation of the electric field at a particular target. As originally proposed in [12], their formulations did not constrain the number of active electrodes allowed to be part of the optimization. This means their solution can have a higher number of electrodes than those available in the hardware, making it impractical. We expanded the functionality of this approach by making multi-electrode tDCS realistically applicable. Our methods not only improve focality of stimula-

tion substantially against the conventional electrode montage, but allow the sparse representation of the optimized solutions; meaning we can specify the number of active electrodes we have at our disposal and subsequently obtain the optimal currents for that subset. This has a major implication in the simplicity of applying the technique, using fewer electrodes . Furthermore, a sparse representation reduces the cost of the necessary hardware for multi-electrode stimulation. Since the methods grant the freedom to choose the number of active electrodes, they are compatible with any stimulator system.

We introduced the feature of simultaneous multi-targeting. This functionality can be applied in treatment for stroke (already treated with tDCS [106]), where the two brain hemispheres are stimulated. Multi-electrode tDCS allows not only to stimulate simultaneously in a focal way, but to specify the orientation of the field at the desired targets.

Our analysis of the direction of the induced electric field in the cortex yields a deeper understanding of how neurons are affected as a result of tDCS, contrasting the common belief that fields are radial under the electrodes and that neurons are therefore affected at their somas [107]. We were able to show that due to the complex cortical folding, fields are predominantly tangential under the electrodes and consequently neurons are most likely affected at their afferent terminals [108]. By analyzing the directionality of the radial electric field component, we are the first to quantify the direction of polarization in the human cortex by tDCS (inward: depolarization, outward: hyperpolarization) [141].

We successfully applied our anatomically accurate animal models to plan two animal studies: (1) a study to analyze the effect of rTMS on neurotransmitter outflow in the nucleus accumbens of the awake rat [124], and (2) a study to analyze memory consolidation in rats after slow-oscillating tDCS [125]. Our models were able to predict the outcome of stimulation, provide guidance as to what structures were stimulated, and support functional hypotheses about the role of stimulation on specific anatomical structures.

The models and methods presented in this work contribute to the systematic use of transcranial stimulation by allowing to plan stimulation beforehand and adjust the parameters to reach the desired outcome. By improving focality, we gain control over the way stimulation is delivered, which shall yield more ambitious clinical and research applications in the future.

9.2 Future work

9.2.1 Promising brain modulation techniques

In the search of new techniques to modulate brain function, invasive methods such as deep brain stimulation have been able to achieve better temporal and spatial resolution than its non-invasive counterparts. In recent years, optogenetic-based methods using light-sensitive ion channels or transporters have been able to offer unrivaled resolution (micron scale) to alter or modulate neuronal function [183],[184],[185]. However, optogenetics is also invasive, requiring to reach the target region with light. Besides, it involves genetic modification, which can thereby not only work as an on/off switch in the target cell, but alter its original function altogether by changing intracellular and extracellular ion concentrations [186].

Recent studies have highlighted the viability to stimulate the brain with pulsed ultrasound waves applied transcranially [187], [188], [189]. Ultrasound is a mechanical pressure wave. When applied to neural tissue it is known to generate a temperature gradient as well as mechanical changes. These two effects can also induce tissue damage when ultrasound has high-intensity (>1 W/cm^2) [190]. However, when using intensities <500 mW/cm^2 pulsed ultrasound can generate mechanical effects without producing significant thermal changes, avoiding therefore possible damage [191].

In [187], the authors applied low intensity (<300 mW/cm^2) and low frequency (<0.65 MHz, reliably transmitted through bone [192]) transcranial pulsed ultrasound in the intact mice brain *in vivo*. They were able to evoke motor behaviors and show that it is safe and reliable to stimulate with such parameters, in the absence of temperature rise in the brain (< 0.01° C). Moreover, they were able to stimulate sub-cortical structures, e.g. the hippocampus in mice [187] and various structures in the rabbit, where the authors report a resolution of nearly 2 mm and while using the technique in conjunction with fMRI [193].

Apart from the limitations of transcranial ultrasound at high intensities (mechanical and thermal effects capable of destroying biological tissue), at low intensities, possible inertial cavitational damage in soft tissue can still take place, i.e. the formation of bubbles or empty space occurring at pressures greater than 40 MPa due to the mechanical stress of the sound waves. Therefore, one should apply intensities in the lower limit of the allowed range to avoid such pressures [188].

The multi-electrode tDCS optimization methods portrayed in this work could be applied to transcranial ultrasound. As a matter of fact, one could theoretically target deep structures in the brain, given that the effective radiation pattern from multiple sound sources can be reinforced or suppressed at different locations, using the so-called phased arrays [194],[195].

9.2.2 Model generation pipeline automation

A fundamental part for the simulations portrayed in this work are the anatomically-based models. We generated these models employing semi-automatic methods with several steps in between. In the segmentation stage, we used well-known methods; however, some manual correction and verification of the segmentation masks was necessary to ensure that there were not isolated parts, or overlapping regions, which can cause problems in the subsequent steps. It is because of this tedious pipeline that the automation of the different steps could save considerable time.

There are a number of automatic brain segmentation tools (FSL [155], FreeSurfer [196], SPM [197], etc.) which perform differently according to the quality and type(s) of the imaging data used as input. They normally yield acceptable results for visualization; however, mesh generation is a sensitive process and possible errors may occur if the data hasn't been handled appropriately. Therefore, the automation of the segmentation process should integrate a mask refinement step, an overlap check and an atlas-based topology check of the different layers to avoid leakage.

The idea of a model generation pipeline has been explored in [151]. Although they provide a systematic approach for the process, the user is still required to run different software separately and is therefore error-prone and more time-consuming. Our idea would be to have a master software suite which could still be dependent on other software for various steps, but that could be controlled in one single piece. Adding the custom-built checks mentioned before, one can make sure the model is on the right track progressively. One shall indicate the requirements in the input data (e.g. appropriate MRI data sequences) and be able to control the detail in the mesh, adjusting the desired number of elements.

Such a software suite would be greatly beneficial for the systematic and fast generation of anatomically-based models. It would be of great use to the EEG/tDCS/TMS research communities (among others) and could set a standard for model generation.

List of Figures

Appendix A

Algorithms

Algorithm 1: Orthogonal Matching Pursuit (OMP)

Input : $\mathbf{A}, \mathbf{e_d}, k$

Initialization: $\mathbf{r} = \mathbf{e_d}$, $D = \emptyset$

for *n=1, until n=k* **do**

1 *Calculate inner product*

$\alpha_i = | < \mathbf{A}^T, \mathbf{r} > |$;

2 *Find element best resembling the residual*

$i_{max} = \arg\max_{\alpha, i \notin D}(\alpha_i)$;

3 *Update winning-elemets set*

$D_n = D_{n-1} \cup i_{max}$;

4 *Solve optimization problem*

$\tilde{\mathbf{s}} = \arg\min_s \|\mathbf{e_d} - \mathbf{A}_D\mathbf{s}\|_2^2$;

subject to $\sum_{m=1}^{M} |s_m| \leq s_{max}$, and $|\sum_{m=1}^{M} s_m| \leq s_{max}$;

5 *Calculate new residual*

$\mathbf{r} = \mathbf{e_d} - \mathbf{A}_D\tilde{\mathbf{s}}$;

Output: $\tilde{\mathbf{s}}$

Where:

$\mathbf{A}$ is the mixing matrix

$\mathbf{e_d}$ is the desired output

$\tilde{\mathbf{s}}$ is the OMP coefficients vector

k is the desired number of non-zero elements in $\tilde{\mathbf{s}}$

$\mathbf{r}$ is the residual

α is the inner product of the current residual with matrix A

D is the winning-elements set

Algorithm 2: Stepwise optimal selection (SOS)

Input : $\mathbf{A}, \mathbf{e_d}, k$

Initialization: $W = \emptyset$, $C = \emptyset$, $D \in \mathbb{N}^{m \times 1}$

for *n=1, until n=k* **do**

  forall the *elements of D* **do**

1 *Add new temporary element*

   $C = W \cup j$; (where: $j \in D$)

2 *Solve optimization problem*

   $\tilde{\mathbf{s}} = \arg\min_s \|\mathbf{e_d} - \mathbf{A}_C\mathbf{s}\|_2^2$;

   subject to $\sum_{m=1}^{M} |s_m| \leq s_{max}$, and $|\sum_{m=1}^{M} s_m| \leq s_{max}$;

3 *Obtain residual sum of squares (RSS)*

   $\hat{\mathbf{r}}_j = \sum_{n=1}^{N} (\mathbf{e_d}(\mathrm{u_n}) - \mathbf{A}_C\tilde{\mathbf{s}})^2$;

4 *Clean temporary elements set*

   $C = \emptyset$;

5 *Find element which minimizes the RSS*

   $j_{min} = \arg\min_{\hat{r}}(\hat{\mathbf{r}}_j)$;

6 *Update the winning-elements set*

   $W = W \cup j_{min}$;

7 *Update elements set: eliminate last winning element*

   $D = D \setminus j_{min}$;

8 *Solve optimization problem for optimal subset*

$\hat{\mathbf{s}} = \arg\min_s \|\mathbf{e_d} - \mathbf{A}_W\mathbf{s}\|_2^2$;

subject to $\sum_{m=1}^{M} |s_m| \leq s_{max}$, and $|\sum_{m=1}^{M} s_m| \leq s_{max}$;

Output: $\hat{\mathbf{s}}$

Where:

A is the mixing matrix

b is the desired output vector

$\tilde{\mathbf{s}}$ is the temporary coefficients vector

$\hat{\mathbf{s}}$ is the SOS coefficients vector

k is the desired number of non-zero elements in **s**

$\hat{\mathbf{r}}$ is the residual sum of squares vector

W is the winning-elements set

C is a temporary elements set

D is the elements set

Bibliography

[1] J. Reis, E.M. Robertson, J.W. Krakauer, J. Rothwell, L. Marshall, C. Gerloff, E.M. Wassermann, A. Pascual-Leone, F. Hummel, P.A. Celnik, J. Classen, A. Floel, U. Ziemann, W. Paulus, H.R. Siebner, J. Born, and L.G. Cohen. Consensus: Can transcranial direct current stimulation and transcranial magnetic stimulation enhance motor learning and memory formation? *Brain Stimul*, 1(4):363 – 369, 2008.

[2] M. Nitsche, L. Cohen, E. Wassermann, A. Priori, N. Lang, A. Antal, W. Paulus, F. Hummel, P.S. Boggio, F. Fregni, and A. Pascual-Leone. Transcranial direct current stimulation: state of the art 2008. *Brain Stimul*, 1:206–223, 2008.

[3] V. Walsh and A. Cowey. Transcranial magnetic stimulation and cognitive neuroscience. *Nat Neurosci*, 1:73–79, 2000.

[4] M. Nitsche, S. Doemkes, T. Karakoese, A. Antal, D. Liebetanz, N. Lang, F. Tergau, and W. Paulus. Shaping the effects of transcranial direct current stimulation of the human motor cortex. *J Neurophysiol*, 97:3109–3117, 2007.

[5] M.E. Keck, T. Welt, M.B. Mueller, A. Erhardt, F. Ohl, N. Toschi, F. Holsboer, and I. Sillaber. Repetitive transcranial magnetic stimulation increases the release of dopamine in the mesolimbic and mesostriatal system. *Neuropharmacology*, 43:101–109, 2002.

[6] A. Erhardt, I. Sillaber, T. Welt, M.B. Mueller, N. Singewald, and M.E. Keck. Repetitive transcranial magnetic stimulation increases the release of dopamine in the nucleus accumbens shell of morphine-sensitized rats during abstinence. *Neuropsychopharmacol*, 29:2074–2080, 2004.

[7] A. Fleischmann, S. Hirschmann, O.T. Dolberg, P.N. Dannon, and L. Grunhaus. Chronic treatment with repetitive transcranial magnetic stimulation

inhibits seizure induction by electroconvulsive shock in rats. *Biol Psychiatry*, 45(6):759–763, 1999.

[8] A. Datta, V. Bansal, J. Diaz, J. Patel, D. Reato, and M. Bikson. Gyri-precise head model of transcranial direct current stimulation: Improved spatial focality using a ring electrode versus conventional rectangular pad. *Brain Stimul*, 2(4):201 – 207.e1, 2009.

[9] R. Salvador, A. Mekonnen, G. Ruffini, and P.C. Miranda. Modeling the electric field induced in a high resolution realistic head model during transcranial current stimulation. In *IEEE Eng Med Biol Soc*, pages 2073 –2076, Buenos Aires, Argentina, 2010.

[10] T. Radman, R. L. Ramos, J. C. Brumberg, and M. Bikson. Role of cortical cell type and morphology in sub- and suprathreshold uniform electric field stimulation. *Brain Stimul*, 2:215–228, 2009.

[11] A. Thielscher, A. Opitz, and M. Windhoff. Impact of the gyral geometry on the electric field induced by transcranial magnetic stimulation. *NeuroImage*, 54(1):234 – 243, 2011.

[12] J. Dmochowski, A. Datta, M. Bikson, Y. Su, and L.C. Parra. Optimized multi-electrode stimulation increases focality and intensity at target. *J Neural Eng*, 8, 2011.

[13] National Institute of Mental Health. *Depression*. NIH publication No. 08 3561, USA, 2008.

[14] C.J.L. Murray and A.D. Lopez. Alternative projections of mortality and disability by cause 1990-2020: Global burden of disease study. *Lancet*, 349(9064):1498–1504, 1997.

[15] G. Rait, K. Walters, M. Griffin, M. Buszewicz, I. Petersen, and I. Nazareth. Recent trends in the incidence of recorded depression in primary care. *Brit J Psychiatry*, 195(6):520–524, 2009.

[16] M.S. George, J.J. Taylor, and E.B. Short. The expanding evidence base for rTMS treatment of depression. *Curr Opin Psychiatr*, 26(1):13–18, 2013.

[17] R.M. Berman, M. Narasimhan, G. Sanacora, A.P. Miano, R.E. Hoffman, X.S. Hu, D.S. Charney, and N.N. Boutros. A randomized clinical trial of repetitive transcranial magnetic stimulation in the treatment of major depression. *Biol Psychiatry*, 47(4):332–337, 2000.

[18] W.M. McDonald, V. Durkalski, E.R. Ball, P.E. Holtzheimer, M. Pavlicova, S.H. Lisanby, D. Avery, B.S. Anderson, Z. Nahas, and P. Zarkowski. Improving the antidepressant efficacy of transcranial magnetic stimulation: maximizing the number of stimulations and treatment location in treatment-resistant depression. *Depress Anxiety*, 28(11):973–980, 2011.

[19] M.S. George, S.H. Lisanby, D. Avery, W.M. McDonald, V. Durkalski, M. Pavlicova, B. Anderson, Z. Nahas, P. Bulow, and P. Zarkowski. Daily left prefrontal transcranial magnetic stimulation therapy for major depressive disorder: a sham-controlled randomized trial. *Arch Gen Psychiatry*, 67(5):507–516, 2010.

[20] F. Fregni, P.S. Boggio, M.A. Nitsche, M.A. Marcolin, S.P. Rigonatti, and A. Pascual-Leone. Treatment of major depression with transcranial direct current stimulation. *Bipolar Disord*, 8(2):203–204, 2006.

[21] A.R. Brunoni, M.A. Nitsche, N. Bolognini, M. Bikson, T. Wagner, L. Merabet, D.J. Edwards, A. Valero-Cabre, A. Rotenberg, A. Pascual-Leone, R. Ferrucci, A. Priori, P.S. Boggio, and F. Fregni. Clinical research with transcranial direct current stimulation tDCS: Challenges and future directions. *Brain Stimul*, 5(3):175–195, 2012.

[22] R. Ferrucci, M. Bortolomasi, M. Vergari, L. Tadini, B. Salvoro, M. Giacopuzzi, S. Barbieri, and A. Priori. Transcranial direct current stimulation in severe, drug-resistant major depression. *J Affect Disord*, 118(1-3):215, 2009.

[23] R. Ferrucci, M. Bortolomasi, A. Brunoni, M. Vergari, L. Tadini, M. Giacopuzzi, and A. Priori. Comparative benefits of transcranial direct current stimulation (tdcs) treatment in patients with mild/moderate vs. severe depression. *Clin Neuropsychiatry*, 6(6):246–51, 2009.

[24] P.L. Kolominsky-Rabas, M. Weber, O. Gefeller, B. Neundoerfer, and P.U. Heuschmann. Epidemiology of ischemic stroke subtypes according to toast criteria incidence, recurrence, and long-term survival in ischemic stroke subtypes: a population-based study. *Stroke*, 32(12):2735–2740, 2001.

[25] R. Schulz, C. Gerloff, and F.C. Hummel. Non-invasive brain stimulation in neurological diseases. *Neuropharmacology*, 64:579–587, 2012.

[26] National Center for Biotechnology Information. *Stroke*. U.S. National Library of Medicine, 2011.

[27] S.M. Lai, S. Studenski, P.W. Duncan, and S. Perera. Persisting consequences of stroke measured by the stroke impact scale. *Stroke*, 33(7):1840–1844, 2002.

[28] F.J. Carod-Artal and J.A. Egido. Quality of life after stroke: the importance of a good recovery. *Cerebrovasc Dis*, 27(1):204–214, 2009.

[29] P.M. Pedersen, H.S. Jørgensen, H. Nakayama, H.O. Raaschou, and T.S. Olsen. Hemineglect in acute stroke-incidence and prognostic implications: The copenhagen stroke study1. *Am J Phys Med Rehab*, 76(2):122–127, 1997.

[30] J.M. Baker, C. Rorden, and J. Fridriksson. Using transcranial direct-current stimulation to treat stroke patients with aphasia. *Stroke*, 41(6):1229–1236, 2010.

[31] J. Fridriksson, J.D. Richardson, J.M. Baker, and C. Rorden. Transcranial direct current stimulation improves naming reaction time in fluent aphasia a double-blind, sham-controlled study. *Stroke*, 42(3):819–821, 2011.

[32] P.S. Boggio, A. Nunes, S.P. Rigonatti, M.A. Nitsche, A. Pascual-Leone, and F. Fregni. Repeated sessions of noninvasive brain dc stimulation is associated with motor function improvement in stroke patients. *Restorative Neurol Neurosci*, 25(2):123–129, 2007.

[33] T.H. Emara, R.R. Moustafa, N.M. Elnahas, A.M. Elganzoury, T.A. Abdo, S.A. Mohamed, and M.A. Eletribi. Repetitive transcranial magnetic stimulation at 1hz and 5hz produces sustained improvement in motor function and disability after ischaemic stroke. *Eur J Neurol*, 17(9):1203–1209, 2010.

[34] R. Lindenberg, V. Renga, LL Zhu, D. Nair, and G. Schlaug. Bihemispheric brain stimulation facilitates motor recovery in chronic stroke patients. *Neurology*, 75(24):2176–2184, 2010.

[35] J.P. Lefaucheur, X. Drouot, Y. Keravel, and J.P. Nguyen. Pain relief induced by repetitive transcranial magnetic stimulation of precentral cortex. *Neuroreport*, 12(13):2963–2965, 2001.

[36] R. Cantello, R. Tarletti, and C. Civardi. Transcranial magnetic stimulation and Parkinson's disease. *Brain Research Reviews*, 38:309–327, 2002.

[37] M.A. Nitsche and W. Paulus. Noninvasive brain stimulation protocols in the treatment of epilepsy: current state and perspectives. *Neurotherapeutics*, 6:244–250, 2009.

[38] F. Fregni, P. S. Boggio, M. C. Santos, M. Lima, A. L. Vieira, S.P. Rigonatti, M. Teresa A. Silva, E.R. Barbosa, M.A. Nitsche, and A. Pascual-Leone. Noninvasive cortical stimulation with transcarnial current stimulation in parkinson's disease. *Mov Disord*, 21:1693–1702, 2006.

[39] F. Fregni, P. Boggio, M. Lima, M. Ferreira, T. Wagner, S. Rigonatti, A. Castro, D. Souza, M. Riberto, S. Freedman, M. Nitsche, and A. Pascual-Leone. A sham-controlled phase ii trial of transcranial direct current stimulation for the treatment of central pain in traumatic spinal cord injury. *Pain*, 122:197–209, 2006.

[40] R. Ferrucci, F. Mameli, I. Guidi, S. Mrakic-Sposta, M. Vergari, S. Marceglia, F. Cogiamanian, S. Barbieri, E. Scarpini, and A. Priori. Transcranial direct current stimulation improves recognition memory in alzheimer disease. *Neurology*, 71(7):493–498, 2008.

[41] P.S. Boggio, N. Sultani, S. Fecteau, L. Merabet, T. Mecca, A. Pascual-Leone, A. Basaglia, F. Fregni, et al. Prefrontal cortex modulation using transcranial dc stimulation reduces alcohol craving: a double-blind, sham-controlled study. *Drug Alcohol Depen*, 92(1):55–60, 2008.

[42] A.M. Speer, T.A. Kimbrell, E.M. Wassermann, J.D. Repella, M.W. Willis, P. Herscovitch, and R.M. Post. Opposite effects of high and low frequency rtms on regional brain activity in depressed patients. *Biol Psychiatry*, 48(12):1133–1141, 2000.

[43] S. Fecteau, D. Knoch, F. Fregni, N. Sultani, P. Boggio, and A. Pascual-Leone. Diminishing risk-taking behavior by modulating activity in the prefrontal cortex: A direct current stimulation study. *J Neurosci*, 27(46):12500–12505, 2007.

[44] D.B. Stone and C.D. Tesche. Transcranial direct current stimulation modulates shifts in global/local attention. *Neuroreport*, 20(12):1115–1119, 2009.

[45] A. Fertonani, S. Rosini, M. Cotelli, P.M. Rossini, and C. Miniussi. Naming facilitation induced by transcranial direct current stimulation. *Behav Brain Res*, 208(2):311–318, 2010.

[46] L. Marshall, M. Moelle, and J. Born. Transcranial direct current stimulation during sleep improves declarative memory. *J Neurosci*, 24:9985–9992, 2004.

[47] L. Marshall, H. Helgadottir, M. Moelle, and J. Born. Boosting slow oscillations during sleep potentiates memory. *Nature*, 444:610–613, 2006.

[48] L. Marshall and J. Born. Brain stimulation during sleep. *J Sleep Med Clin*, 6, 2011.

[49] R. Salvador. *Numerical modelling in transcranial magnetic stimulation*. PhD thesis, University of Lisboa, 2009.

[50] P.C. Miranda, F. Wendling, I. Merlet, B. Molaee-Ardekani, G. Ruffinni, S. Dunne, A. Soria-Frisch, and D. Whitmer. *Brain Stimulation: models, experiments and open questions*. HIVE: Hyper Interaction Viability Experiments, 2009.

[51] E.M. Wassermann, C.M Epstein, U. Ziemann, V. Walsh, T. Paus, and S.H. Lisanby. *The Oxford Handbook of Transcranial Stimulation*. Oxford, 2008.

[52] V. Schnabel and J.J. Struijk. Magnetic and electrical stimulation of undulating nerve fibres: a simulation study. *Med Biol Eng Comput*, 37(6):704–709, 1999.

[53] R.P. Feynman, R.B. Leighton, and M. Sands. *The Feynman Lectures on Physics: Mainly Mechanics, Radiation, and Heat: The New Millennium Edition*. Basic Books, 2011.

[54] O. Biro and K. Preis. On the use of the magnetic vector potential in the finite-element analysis of three-dimensional eddy currents. *IEEE Trans Magn*, 25(4):3145–3159, 1989.

[55] D. Fleisch. *A Student's guide to Maxwell's equations*. Cambridge University Press, 2008.

[56] S. Humphries Jr. *Field solutions on computers*. CRC, 1997.

[57] P.C. Miranda, M. Hallet, and P.J. Basser. The electric field induced in the brain by magnetic stimulation: a 3D finite-element analysis of the effect of tissue heterogeneity and anisotropy. *IEEE Trans Biomed Eng*, 50(9):1074–1085, 2003.

[58] COMSOL AB. *COMSOL Multiphysics 3.5a User's Guide*, 2008.

[59] F.S. Salinas, J.L. Lancaster, and P.T. Fox. 3D modeling of the total electric field induced by transcranial magnetic stimulation using the boundary element method. *Phys Med Biol*, 54:3631–3647, 2009.

[60] B.J. Roth, J.M. Hallet, and L.G. Cohen. A theoretical calculation of the electric field in the cortex during magnetic stimulation. *Electroencephalogr Clin Neurophysiol*, 81(1):47–56, 1991.

[61] B.J. Roth, L.G. Cohen, and M. Hallett. The electric field induced during magnetic stimulation. *Electroencephalogr Clin Neurophysiol (Suppl)*, 43:268–278, 1991.

[62] N. Toschi, T. Welt, M. Guerrisi, and M.E. Keck. A reconstruction of the conductive phenomena elicited by transcranial magnetic stimulation in heterogeneous brain tissue. *Phys Med*, 24:80–86, 2008.

[63] N. Toschi, T. Welt, M. Guerrisi, and M.E. Keck. Transcranial magnetic stimulation in heterogeneous brain tissue: clinical impact on focality, reproducibility and true sham stimulation. *J Psychiatr Res*, 43:255–264, 2009.

[64] C. Johnson. *Computational methods and software for biolelectric field problems. The Biomedical Engineering Handbook: Biomedical Engineeing Fundamentals*, volume 1. J.D. Bronzino (Hoboken, NJ:CRC Press), 2006.

[65] M. Nadeem, T. Thorlin, O.P. Gandhi, and M. Persson. Computation of electric and magnetic stimulation in human head using the 3-D impedance method. *IEEE Trans Biomed Eng*, 50(7):900–907, 2003.

[66] N. De Geeter, G. Crevecoeur, and L. Dupre. An efficient 3-D eddy-current solver using an independent impedance method for transcranial magnetic stimulation. *IEEE Trans Biomed Eng*, 58(2):310–320, 2011.

[67] L. Heller and D.B. van Hulsteyn. Brain stimulation using electromagnetic sources: theoretical aspects. *Biophys J*, 63(1):129–138, 1992.

[68] P. Ravazzani, J. Ruohonen, F. Grandori, and G. Tognola. Magnetic stimulation of the nervous system: Induced electric field in unbounded, semi-infinite, spherical, and cylindrical media. *Ann Biomed Eng*, 24:606–616, 1996.

[69] K. Kane and A. Taub. A history of local electrical analgesia. *Pain*, 1:125–138, 1975.

[70] S. Zago, R. Ferrucci, F. Fregni, and A. Priori. Bartholow, sciamanna, alberti: pioneers in the electrical stimulation of the exposed human cerebral cortex. *The Neuroscientist*, 14(5):521–528, 2008.

[71] A.T. Barker, R. Jalinous, and I.L. Freeston. Non-invasive magnetic stimulation of human motor cortex. *Lancet*, 1(8437):1106–1107, 1985.

[72] A. Pascual-Leone, N.J. Davey, J. Rothwell, E.M. Wassermann, and B.K. Puri. *Handbook of Transcranial Magnetic Stimulation*. Arnold, 2002.

[73] V.E. Amassian, P.J. Maccabee, R.Q. Cracco, J.B. Cracco, M. Somasundaram, J.C. Rothwell, L. Eberle, K. Henry, and A.P. Rudell. The polarity of the induced electric field influences magnetic coil inhibition of human visual cortex: Implications for the site of excitation. *Electroencephalogr Clin Neurophysiol*, 93:21–26, 1994.

[74] J. Ruohonen and R. J. Ilmoniemi. Modeling of the stimulating field generation in TMS. *Electroencephalogr Clin Neurophysiol Suppl*, 51:30–40, 1999.

[75] L. Matthäus, P. Trillenberg, T. Fadini, M. Finke, and A. Schweikard. Brain mapping with transcranial magnetic stimulation using a refined correlation ratio and kendall's tau. *Stat Med*, 27(25):5252–5270, 2008.

[76] S. Groppa, A. Oliviero, A. Eisen, A. Quartarone, L.G. Cohen, V. Mall, A. Kaelin-Lang, T. Mima, S. Rossi, G.W. Thickbroom, P.M. Rossini, U. Ziemann, J. Valls-Sol, and H.R. Siebner. A practical guide to diagnostic transcranial magnetic stimulation: Report of an IFCN committee. *Clin Neurophysiol*, in press, 2012.

[77] F. Padberg and M.S. George. Repetitive transcranial magnetic stimulation of the prefrontal cortex in depression. *Exp Neurology*, 219:2–13, 2009.

[78] G.S. Pell, Y. Roth, and A. Zangen. Modulation of cortical excitability induced by repetitive transcranial magnetic stimulation: Influence of timing and geometrical parameters and underlying mechanisms. *Prog Neurobiol*, 93(1):59 – 98, 2011.

[79] M. Sommer, A. Alfaro, M. Rummel, S. Speck, N. Lang, T. Tings, and W. Paulus. Half sine, monophasic and biphasic transcranial magnetic stimulation of the human motor cortex. *Clin Neurophysiol*, 117:838–844, 2006.

[80] A.V. Peterchev, R. Jalinous, and S.H. Lisanby. A transcranial magnetic stimulator inducing near-rectangular pulses with controllable pulse width cTMS. *IEEE Trans Biomed Eng*, 55:257–266, 2008.

[81] Y. Terao and Y. Ugawa. Basic mechanisms of TMS. *J Clin Neurophysiol*, 19(4):322–343, 2002.

[82] M. Gangitano, A. Valero-Cabre, J.M. Tormos, F.M. Mottaghy, J.R. Romero, and A. Pascual-Leone. Modulation of input output curves by low and high frequency repetitive transcranial magnetic stimulation of the motor cortex. *Clin Neurophysiol*, 113:12491257, 2002.

[83] A. Hiscock, S. Miller, J. Rothwell, R.C. Tallis, and V.M. Pomeroy. Informing dosefinding studies of repetitive transcranial magnetic stimulation to enhance motor function: a qualitative systematic review. *Neurorehabil Neural Repair*, 22:228249, 2008.

[84] H.R. Siebner, N. Lang, V. Rizzo, M.A. Nitsche, W. Paulus, R.N. Lemon, and J.C. Rothwell. Preconditioning of low-frequency repetitive transcranial magnetic stimulation with transcranial direct current stimulation: Evidence for homeostatic plasticity in the human motor cortex. *J Neurosci*, 24:3379–3385, 2004.

[85] J. Ruohonen. *Transcranial Magnetic Stimulation: Modelling and New Techniques*. PhD thesis, Helsinki University of Technology, 1995.

[86] A. Thielscher and T. Kammer. Electric field properties of two commercial figure-8 coils in TMS: calculation of focality and eficciency. *Clin Neurophysiol*, 115(7):1697–1708, 2004.

[87] L. Richter, P. Trillenberg, A. Schweikard, and A. Schlaefer. Stimulus intensity for hand held and robotic transcranial magnetic stimulation. *Brain Stimul*, [Epub ahead of print], 2012.

[88] L. Richter, R. Bruder, and A. Schweikard. Hand-assisted positioning and contact pressure control for motion compensated robotized transcranial magnetic stimulation. *IJCARS*, [Epub ahead of print]:1–8, 2012.

[89] L. Richter, F. Ernst, A. Schlaefer, and A. Schweikard. Robust robot-camera calibration for robotized transcranial magnetic stimulation. *Int J Med Rob Comp*, 7(4):414–422, 2011.

[90] A. Luft, A. Kaelin-Lang, T.-K. Hauser, L.G. Cohen, N.V. Thakor, and D.F. Hanley. Transcranial magnetic stimulation in the rat. *Exp Brain Res*, 140:112–121, 2001.

[91] A. Rotenberg, P. A. Muller, A. M. Vahahzadeh-Hagh, X. Navarro, R. Lopez-Vales, A. Pascual-Leone, and F. Jensen. Lateralization of forelimb motor evoked potentials by transcranial magnetic stimulation in rats. *Clin Neurophysiol*, 121:104–108, 2010.

[92] D.-H. Kim, G. E. Georghiou, and C. Won. Improved field localization in transcranial magnetic stimulation of the brain with the utilization of a conductive shield plate in the stimulator. *IEEE Trans Biomed Eng*, 53(4):720–725, 2006.

[93] K. Hsiung and D.M. Durand. A 3D differential coil design for localized magnetic stimulation. *IEEE Trans Biomed Eng*, 48(10):1162–1168, 2001.

[94] A. Zangen, Y. Roth, and M. Hallett. Transcranial magnetic stimulation of deep brain regions: Evidence for efficacy of the h-coil. *Clin Neurophysiol*, 119:775–779, 2005.

[95] T. Fadini, L. Matthaeus, H. Rothkegel, M. Sommer, F. Tergau, A. Schweikard, W. Paulus, and M.A. Nitsche. H-coil: Induced electric field properties and input/output curves on healthy volunteers, comparison with a standard figure-of-eight coil. *Clin Neurophysiol*, 120:1174–1182, 2009.

[96] K. Wendicke. *Optimierung von Stimulationsspulen für die induktive Nervenreizung*. PhD thesis, Technical University of Munich, 2007.

[97] K. R. Davey and M. Riehl. Suppressing the surface field during transcranial magnetic stimulation. *IEEE Trans Biomed Eng*, 53(2):190–194, 2006.

[98] L. Hernandez-Garcia, T. Hall, L. Gomez, and E. Michielssen. A numerically optimized active shield for improved transcranial magnetic stimulation targeting. *Brain Stimul*, 3:218–225, 2010.

[99] J. Ruohonen, P. Ravazzani, F. Grandori, and R.J. Ilmoniemi. Theory of multichannel magnetic stimulation: Toward functional neuromuscular rehabilitation. *IEEE Trans Biomed Eng*, 46(6):646–651, 1999.

[100] L. Bindman, O. Lippold, and J. Redfearn. The action of brief polarizing currents on the cerebral cortex of the rat (1) during current flow and (2) in the production of long lasting after-effects. *J Physiol*, 172:369–382, 1964.

[101] M. Nitsche and W. Paulus. Excitability changes induced in the human motor cortex by weak transcranial direct current stimulation. *J Physiol*, 529:633–639, 2000.

[102] L. Marshall, M. Moelle, H.R. Siebner, and J. Born. Bifrontal transcranial direct current stimulation slows reaction time in a working memory task. *BMC Neurosci*, 24:6–23, 2005.

[103] F. Froehlich and D. McCormick. Endogenous electric fields may guide neocortical network activity. *Neuron*, 67(1):129 – 143, 2010.

[104] M. Bikson, M. Inoue, H. Akimaya, J. Deans, J. Fox, H. Miyakawa, and J.G.R. Jeffereys. Effects of uniform extracellular dc electric fields on excitability in rat hippocampal slices in vitro. *J Physiol*, 157:175–190, 2004.

[105] T. A. Wagner, M. Zahn, A. Grodzinsky, and A. Pascual-Leone. Three-dimensional head model simulation of transcranial magnetic stimulation. *IEEE Trans Biomed Eng*, 51(9):1586–1598, 2004.

[106] A. Priori, M. Hallett, and J. C. Rothwell. Repetitive transcranial magnetic stimulation or transcranial direct current stimulation? *Brain Stimul*, 2(4):241–245, 2009.

[107] M.A. Nitsche, D. Liebetanz, A. Antal, N. Lang, F. Tergau, and W. Paulus. Modulation of cortical escitability by weak direct current stimulation–technical, safety and functional aspects. *Suppl Clin Neurophysiol*, 56:255–276, 2003.

[108] A. Rahman, D. Reato, M. Arlotti, F. Gasca, A. Datta, L.C. Parra, and M. Bikson. Cellular effects of transcranial direct current stimulation: Somatic and synaptic terminal effects. *J Physiol*, submitted:–, 2012.

[109] J.K. Deans, A.D. Powell, and J.G. Jefferys. Sensitivity of coherent oscillations in rat hippocampus to ac electric fields. *J Physiol*, 583:555–565, 2007.

[110] D. Reato, A. Rahman, M. Bikson, and L.C. Parra. Low-intensity electrical stimulation affects network dynamics by modulating population rate and spike timing. *J Neurosci*, 30(45):15067–15079, 2010.

[111] D. Liebetanz, M.A. Nitsche, F. Tergau, and W. Paulus. Pharmacological approach to the mechanisms of transcranial dc-stimulation-induced after-effects of human motor cortex excitability. *Brain*, 125:2238–2247, 2002.

[112] MA Nitsche, K. Fricke, U. Henschke, A. Schlitterlau, D. Liebetanz, N. Lang, S. Henning, F. Tergau, and W. Paulus. Pharmacological modulation of cortical excitability shifts induced by transcranial direct current stimulation in humans. *J Physiol*, 553(1):293–301, 2004.

[113] P.C. Miranda, M. Lomarev, and M. Hallett. Modeling the current distribution during transcranial direct current stimulation. *Clin Neurophysiol*, 117(7):1623 – 1629, 2006.

[114] A. Datta, M. Elwassif, F. Battaglia, and M. Bikson. Transcranial current stimulation focality using disc and ring electrode configurations: FEM analysis. *J Neural Eng*, 5(2):163–174, 2008.

[115] P. Minhas, A. Datta, and M. Bikson. Cutaneous perception during tDCS: Role of electrode shape and sponge salinity. *Clin Neurophysiol*, 122:637–638, 2011.

[116] M. Bikson, A. Datta, and M. Elwassif. Establishing safety limits for transcranial direct current stimulation. *Clin Neurophysiol*, 120(6):1033, 2009.

[117] D. Liebetanz, R. Koch, S. Mayenfels, F. Koenig, W. Paulus, and M.A. Nitsche. Safety limits of cathodal transcranial direct current stimulation in rats. *Clin Neurophysiol*, 120(6):1161 – 1167, 2009.

[118] P.C. Miranda, P. Faria, and M. Hallett. What does the ratio of injected current to electrode area tell us about current density in the brain during tDCS? *Clin Neurophysiol*, 120(6):1183 – 1187, 2009.

[119] P. Minhas, J. Patel, V. Bansal, J. Ho, A. Datta, and M. Bikson. Electrodes for high-definition transcutaneous dc stimulation for applications in drug-delivery and electrotherapy, including tdcs. *J Neurosci Methods*, 190(2):18897, 2010.

[120] L. Ramrath, A. Schweikard, and U.G. Hofmann. Spherical assistant for stereotactic surgery. In *IEEE Int Conf on Intelligent Robots and Systems*, San Diego, CA, USA, 2007.

[121] L. Ramrath, U.G. Hofmann, and A. Schweikard. A Robotic Assistant for Stereotactic Neurosurgery on Small Animals. *IJCARS*, 4(4):295–303, 2008.

[122] F. Gasca, L. Richter, and A. Schweikard. Simulation of a conductive shield plate for transcranial magnetic stimulation in the rat. In *IEEE Eng Med Biol Soc*, pages 1593–1596, Buenos Aires, Argentina, September 2010.

[123] F. Gasca, L. Marshall, S. Binder, A. Schlaefer, U.G. Hofmann, and A. Schweikard. Finite element simulation of transcranial current stimulation in realistic rat head model. In *Int IEEE EMBS Conf Neural Eng*, volume 5, pages 36–39, Cancun, Mexico, 2011.

[124] S. Loeffler, F. Gasca, L. Richter, U. Leipscher, P. Trillenberg, and A. Moser. The effect of repetitive transcranial magnetic stimulation on monoamine outflow in the nucleus accumbens shell in freely moving rats. *Neuropharmacology*, 63(5):898–904, 2012.

[125] S. Binder, K. Berg, F. Gasca, J. Born, and L. Marshall. Boosting slow oscillations during sleep by oscillatory transcranial current stimulation so-tDCS enhances hippocampus-dependent memory consolidation in rats. *J Neurosci*, -(-):submitted, 2012.

[126] A. Thielscher and T. Kammer. Linking physics with physiology in TMS: a sphere field model to determine the cortical stimulation site in TMS. *Neuroimage*, 17(3):1117–1130, 2002.

[127] Z.D. Deng, S.H. Lisanby, and A.V. Peterchev. Electric field depth-focality tradeoff in transcranial magnetic stimulation: Simulation comparison of 50 coil designs. *Brain Stimul*, in press, 2012.

[128] P. Faria, M. Hallett, and P.C. Miranda. A finite element analysis of the effect of electrode area and inter-electrode distance on the spatial distribution of the current density in tDCS. *J Neural Eng*, 8(066017):11, 2011.

[129] R.N. Holdefer, R. Sadleir, and M.J. Russell. Predicted current densities in the brain during transcranial electrical stimulation. *Clin Neurophysiol*, 117:1388–1397, 2006.

[130] M. Chen and D.J. Mogul. Using increased structural detail of the cortex to improve the accuracy of modeling the effects of transcranial magnetic stimulation on neocortical activation. *IEEE Trans Biomed Eng*, 57(5):1216–1226, 2010.

[131] J. Zheng, L. Li, and X. Huo. Analysis of electric field in real rat head model during transcranial magnetic stimulation. In *IEEE Eng Med Biol Soc*, pages 1529–1532, Shanghai, China, September 2005.

[132] R. Salvador and P. Miranda. Transcranial magnetic stimulation of small animals: a modeling study of the influence of coil geometry, size and orientation. In *IEEE Eng Med Biol Soc*, pages 674–677, Minneapolis, USA, September 2009.

[133] G. Paxinos and C. Watson. *The rat brain in stereotaxic coordinates*. Academic Press, 5th edition, 2004.

[134] S. Silva, P.J. Basser, and P.C Miranda. Elucidating the mechanisms and loci of neuronal excitation by transcranial magnetic stimulation using a finite element model of a cortical sulcus. *Clin Neurophysiol*, 119:2405–2413, 2008.

[135] S. Ozen, A. Sirota, M. Belluscio, C. Anastassiou, E.Stark, C. Koch, and G. Buzsaki. Transcranial Electric Stimulation Entrains Cortical Neuronal Populations in Rats. *J Neurosci*, 30(34):11476–11485, 2010.

[136] V. Jurcak, D. Tsuzuki, and I. Dan. 10/20, 10/10, and 10/5 systems revisited: Their validity as relative head-surface-based positioning systems. *NeuroImage*, 34(4):1600 – 1611, 2007.

[137] A. Priori. Brain polarization in humans: a reappraisal of an old tool for prolonged non-invasive modulation of brain excitability. *Clin Neurophysiol*, 114:589–595, 2003.

[138] O. Creutzfeld, G. Fromm, and H. Kapp. Influence of transcortical DC currents on cortical neuronal activity. *Exp Neurol*, 5:436–452, 1962.

[139] L. Bindman, O. Lippold, and J. Redfearn. Long-lasting changes in the level of the electrical activity of the cerebral cortex activity produced by polarized currents. *Nature*, 196:584–585, 1962.

[140] M. Bikson, T. Radman, and A. Datta. Rational modularion of neuronal processing with applied electric fields. In *IEEE Eng Med Biol Soc*, pages 1616–1619, New York, USA, August 2006.

[141] D. Reato, F. Gasca, A. Datta, M. Bikson, L. Marshall, and L.C. Parra. Transcranial electrical stimulation accelerates human sleep homeostasis. *PLoS Comput Biol*, in press:–, 2012.

[142] S. Rush and D. Driscoll. Current distribution in the brain from surface electrodes. *Anasthesia and Analgetica*, 47(6):717–723, 1968.

[143] C.H. Wolters, A. Anwander, X. Tricoche, D. Weinstein, M.A. Koch, and R.S. MacLeod. Influence of tissue conductivity anisotropy on EEG/MEG field and return current computation in a realistic head model: a simulation and visualization study using high-resolution finite element modeling. *NeuroImage*, 30(3):813–826, 2006.

[144] P.W. Nicholson. Specific impedance of cerebral white matter. *Exp Neurol*, 13:386–401, 1965.

[145] S. Mori and J. Zhang. Principles of diffusion tensor imaging and its applications to basic neuroscience research. *Neuron*, 51:527 – 539, 2006.

[146] P. Hagmann, L. Jonasson, P. Maeder, J.-P. Thiran, V. J. Wedeen, and R. Meuli. Understanding diffusion mr imaging techniques: From scalar diffusion-weighted imaging to diffusion tensor imaging and beyond. *Radiographics*, 26(suppl 1):S205–S223, 2006.

[147] P.C. Sundgren, Q. Dong, D. Gomez-Hassan, S.K. Mukherji, P. Maly, and R. Welsh. Diffusion tensor imaging of the brain: review of clinical applications. *Neuroradiology*, 46:339–350, 2004.

[148] D.S. Tuch, V.J. Weeden, A.M Dale, J.S. George, and J.W. Belliveau. Conductivity tensor mapping of the human brain using diffusion tensor mri. *Proc Natl Acad Sci*, 98(20):11697–11701, 2001.

[149] D.S. Tuch, V.J. Weeden, A.M Dale, J.S. George, and J.W. Belliveau. Conductivity mapping of biological tissue using diffusion MRI. *Ann N Y Acad Sci*, 888(1):314–316, 1999.

[150] M. Rullmann, A. Anwander, M. Dannhauer, S.K. Warfield, F.H. Duffy, and C.H. Wolters. EEG source analysis of epileptiform activity using a 1 mm anisotropic hexahedra finite element head model. *NeuroImage*, 44(2):399 – 410, 2009.

[151] M. Windhoff, A. Opitz, and A. Thielscher. Electric field calculations in brain stimulation based on finite elements: An optimized processing pipeline for the generation and usage of accurate individual head models. *Hum Brain Mapp*, [Epub ahead of print], 2011.

[152] D. Guellmar, J. Haueisen, and J.R. Reichenbach. Influence of anisotropic electrical conductivity in white matter tissue on the EEG/MEG forward and inverse solution. a high-resolution whole head simulation study. *NeuroImage*, 51(1):145 – 163, 2010.

[153] N. Toussaint, J.C. Souplet, and P. Fillard. Medinria: Medical image navigation and research tool by INRIA. In *MICCAI Workshop on Interaction in medical image analysis and visualization*, Brisbane, Australia, 2007.

[154] H. Jiang, P.C.M. van Zijl, J. Kim, G.D. Pearlson, and S. Mori. Dtistudio: Resource program for diffusion tensor computation and fiber bundle tracking. *Comput Meth Prog Bio*, 81(2):106–116, 2006.

[155] M.W. Woolrich, S. Jbabdi, B. Patenaude, M. Chappell, S. Makni, T. Behrens, C. Beckmann, M. Jenkinson, and S.M. Smith. Bayesian analysis of neuroimaging data in FSL. *NeuroImage*, 45:S173 – 186, 2009.

[156] W. Plihal and J. Born. Effects of early and late nocturnal sleep on declarative and procedural memory. *J Cognitive Neurosci*, 9:534–547, 1997.

[157] S. Diekelmann and J. Born. The memory function of sleep. *Nat Rev Neurosci*, 11:114–126, 2010.

[158] C.A. Dockery, D. Liebetanz, N. Birbaumer, M. Malinowska, and M.J. Wesierska. Cumulative benefits of frontal transcranial direct current stimulation on visuospatial working memory training and skill learning in rats. *Neurobiol Learn Mem*, 96:452–460, 2011.

[159] F. Gasca, T. Wissel, H. Hadjar, A. Schlaefer, and A. Schweikard. Sparsely optimized multi-electrode transcranial direct current stimulation. In *Front Comp Neursci, Berstein Conf*, Munich, Germany, 2012.

[160] J.-H. Park, S.B. Hong, D.-W. Kim, M. Suh, and C.-H. Im. A novel array-type transcranial direct current stimulation (tdcs) system for accurate focusing on targeted brain areas. *IEEE Trans Magn*, 47:882–885, 2011.

[161] A. Schweikard, R. Tombropoulus, L. Kavraki, J.R. Adler, and J.-C. Latombe. Treatment planning for a radiosurgical system with general kinematics. In *IEEE Int Conf Robot Autom*, pages 1720–1727, San Diego, USA, 1994.

[162] A. Schweikard, A. Schlaefer, and J. Adler. Resampling: an optimization method for inverse planning in robotic radiosurgery. *Med Phys*, 33(11):2738–2741, 2006.

[163] M.L. Kringelbach, N. Jenkinson, S.L.F. Owen, and T.Z. Aziz. Translational principles of deep brain stimulation. *Nat Rev Neurosci*, 8(8):623–635, 2007.

[164] R. Tibshirani. Regression shrinkage and selection via the lasso. *J R Statist Soc*, 58(1):267–288, 1996.

[165] Neuroelectrics. http://www.neuroelectrics.com. Barcelona, Spain.

[166] Soterix Medical Inc. http://www.soterixmedical.com. New York, USA.

[167] S.G. Mallat and Z. Zhang. Matching pursuits with time-frequency dictionaries. *IEEE Trans Signal Process*, 41(12):3397–3415, 1993.

[168] L. Rebollo-Neira and D. Lowe. Optimized orthogonal matching pursuit approach. *IEEE Signal Process Lett*, 9(4):137–140, 2002.

[169] A. Opitz, M. Windhoff, R. M. Heidemann, R. Turner, and A. Thielscher. How the brain tissue shapes the electric field induced by transcranial magnetic stimulation. *NeuroImage*, 58(3):849 – 859, 2011.

[170] R. Salvador, P.C. Miranda, Y. Roth, and A. Zangen. High-permeability core coils for transcranial magnetic stimulation of deep brain regions. In *IEEE Eng Med Biol Soc*, pages 6652–6655, Lyon, France, August 2007.

[171] F.S. Bersani, A. Minichino, P.G. Enticott, L. Mazzarini, N. Khan, G. Antonacci, R.N. Raccah, M. Salviati, R. Delle Chiaie, G. Bersani, P.B. Fitzgerald, and M. Biondi. Deep transcranial magnetic stimulation as a treatment for psychiatric disorders: A comprehensive review. *European Psychiatry*, page in press, 2012.

[172] C.-H. Im, H.-H. Jung, J.-Do. Choi, S.Y. Lee, and K.-Y. Jung. Determination of optimal electrode positions for transcranial direct current stimulation (tDCS). *Phys Med Biol*, 53(11):N219, 2008.

[173] P. Pudil, J. Novovicova, and J. Kittler. Floating search methods in feature selection. *Pattern Recogn Lett*, 15:1119–1125, 1994.

[174] G.G. Turrigiano, K.R. Leslie, N.S. Desai, L.C. Rutherford, and S.B. Nelson. Activity dependent scaling of quantal amplitude in neocortical neurons. *Nature*, 391:892–896, 1998.

[175] S.H. Oh, S.Y. Lee, M.H. Cho, T.-S Kim, and I.H. Kim. Electrical conductivity estimation from diffusion tensor and T2: a silk yarn phantom study. *ISMRM*, page 3034, 2006.

[176] A. Zangen and K. Hyodo. Transcranial magnetic stimulation induces increases in extracellular levels of dopamine and glutamate in the nucleus accumbens. *Neuroreport*, 13:2401–2405, 2002.

[177] A. Pascual-Leone, B. Rubio, F. Pallardo, and M.D. Catala. Early report rapid-rate transcranial magnetic stimulation of left dorsolateral prefrontal cortex in drug-resistant depression. *The Lancet*, 347:233–237, 1996.

[178] M.S. George, S.H. Lisanby, and H.A. Sackeim. Transcranial magnetic stimulation. *Arch Gen Psychiatry*, 56:300–311, 1999.

[179] Y. Shirayama and S. Chaki. Neurochemistry of the nucleus accumbens and its relevance to depression and antidepressant action in rodents. *Curr Neuropharmacol*, 4:277–291, 2006.

[180] P.W. Frankland and B. Bontempi. The organization of recent and remote memories. *Nat Rev Neurosci*, 6:119–130, 2005.

[181] W.C. Leon, M.A. Bruno, S. Allard, K. Nader, and A.C. Cuello. Engagement of the PFC in consolidation and recall of recent spatial memory. *Learn Mem*, 17:297–305, 2010.

[182] S. Binder, P.C Baier, M. Moelle, M. Inostroza, J. Born, and L. Marshall. Sleep enhances memory consolidation in the hippocampus-dependent object-place recognition task in rats. *Neurobiol Learn Mem*, 97:213–219, 2012.

[183] E.S. Boyden, F. Zhang, E. Bamberg, G. Nagel, and K. Deisseroth. Millisecond-timescale, genetically targeted optical control of neural activity. *Nat Neurosci*, 8:1263–1268, 2005.

[184] S. Szobota, P. Gorostiza, F. Del Bene, C. Wyart, D.L. Fortin, K.D. Kolstad, O. Tulyathan, M. Volgraf, R. Numano, and H.L. Aaron et al. Remote control of neuronal activity with a light-gated glutamate receptor. *Neuron*, 54:535–545, 2007.

[185] F. Zhang, A.M. Aravanis, A. Adamantidis, L. de Lecea, and K. Deisseroth. Circuit-breakers: optical technologies for probing neural signals and systems. *Nat Rev Neurosci*, 8:577–581, 2007.

[186] X. Han. In vivo application of optogenetics for neural circuit analysis. *ACS Chem Neurosci*, [Epub ahead of print], 2012.

[187] Y. Tufail, A. Matyushov, N. Baldwin, M.L. Tauchmann, J. Georges, A. Yoshihiro, S.I. Helms Tillery, and W.J. Tyler. Transcranial pulsed ultrasound stimulates intact brain circuits. *Neuron*, 66:681–694, 2010.

[188] Y. Tufail, A. Yoshihiro, S. Pati, M.M. Li, and W.J. Tyler. Ultrasonic neuromodulation by brain stimulation with transcranial ultrasound. *Nature*, 6(9):1453–1470, 2011.

[189] S.J. Norton. Can ultrasound be used to stimulate nerve tissue? *Biomed Eng Online*, 2(6), 2003.

[190] P.H. Tsui, S.H Wang, and C.C. Huang. In vitro effects of ultrasound with different energies on the conduction properties of neural tissue. *Ultrasonics*, 43:560–565, 2005.

[191] D. Dalecki. Mechanical bioeffects of ultrasound. *Annu Rev Biomed Eng*, 6:229–248, 2004.

[192] K. Hynynen and G. Clement. Clinical applications of focused ultrasound-the brain. *Int J Hyperthermia*, 23:193–202, 2007.

[193] S.-S. Yoo, A. Bystritsky, J.-H. Lee, Y. Zhang, K. Fischer, B.-K. Min, N.J. McDannold, A. Pascual-Leone, and F.A. Jolesz. Focused ultrasound modulates region-specific brain activity. *NeuroImage*, 56(3):1267–1275, 2011.

[194] E. Martin, D. Jeanmonod, A. Morel, E. Zadicario, and B. Werner. High-intensity focused ultrasound for noninvasive functional neurosurgery. *Ann Neurol*, 66:858–861, 2009.

[195] K. Hynynen, G.T. Clement, N. McDannold, N. Vykhodtseva, R. King, P.J. White, S. Vitek, and F.A. Jolesz. 500-element ultrasound phased array system for noninvasive focal surgery of the brain: a preliminary rabbit study with ex vivo human skulls. *Magn Reson Med*, 52:100–107, 2004.

[196] B. Fischl. Freesurfer. *NeuroImage*, 62(2):774–781, 2012.

[197] J. Ashburner and K.J. Friston. Unified segmentation. *NeuroImage*, 26(3):839–851, 2005.